Doctoral theses at NTNU, 2018:339

Krzysztof Adamczyk

Defect-impurity interactions in high performance multicrystalline silicon

NTNU
Norwegian University of
Science and Technology

Doctoral thesis

Krzysztof Adamczyk

Doctoral theses at NTNU, 2018:339

NTNU

NTNU
Norwegian University of Science and Technology
Thesis for the Degree of
Philosophiae Doctor
Faculty of Natural Sciences
Department of Materials Science and
Engineering

ISBN 978-82-326-3467-5 (printed ver.)
ISBN 978-82-326-3466-8 (electronic ver.)
ISSN 1503-8181

NTNU
Norwegian University of
Science and Technology

Krzysztof Adamczyk

Defect-impurity interactions in high performance multicrystalline silicon

Thesis for the Degree of Philosophiae Doctor

Trondheim, October 2018

Norwegian University of Science and Technology
Faculty of Natural Sciences
Department of Materials Science and Engineering

NTNU
Norwegian University of
Science and Technology

NTNU
Norwegian University of Science and Technology

Thesis for the Degree of Philosophiae Doctor

Faculty of Natural Sciences
Department of Materials Science and Engineering

© Krzysztof Adamczyk

ISBN 978-82-326-3467-5 (printed ver.)
ISBN 978-82-326-3466-8 (electronic ver.)
ISSN 1503-8181

Doctoral theses at NTNU, 2018:339

Printed by NTNU Grafisk senter

Preface

This thesis is submitted in fulfillment of the requirements for the degree of Doctor of Philosophy at the Norwegian University of Science and Technology (NTNU). The main part of the work has been carried out from August 2014 to August 2017, where most of the experiments were performed at the Department of Materials Science and Engineering at NTNU.

The author received part of the studied material from the team responsible for ingot growth at NTNU, part from the REC team, which used their facility in Singapore. The thermal processing and photoluminescence analysis of the wafers was done by the team at Institute for Energy Technology, IFE, in Kjeller, Norway. The wafers were sent for processing into Heterojunction with Intrinsic Thin Layer cells (HIT) to the Shanghai Institute of Microsystem and Information Technology, SIMIT, in Shanghai, China. The Light Beam Induced Current (LBIC) measurements was performed by the author at Karlstad University in Karlstad, Sweden. Secondary Ion Mass Spectroscopy (SIMS) was performed by Thomas Neset Sky at the MiNaLab in Oslo, Norway. Neutron Activation Analysis (NAA) was performed by the staff of the Missouri University Research Reactor in USA. Micro X-Ray Fluorescence analysis was performed by the collaborating teams from the Massachusets Institute of Technology and the Advanced Photon Source of the Argonne National Laboratory in USA. The remaining techniques used in this work were performed by the author in the facilities and with assistance of Sintef and NTNU teams in Trondheim, Norway.

The research work was financed by the Research Council of Norway and the industrial partners within the project “Impurity Control”. Professor Marisa Di Sabatino at the Department of Materials Science and Engineering at NTNU was the principal supervisor, while Gaute Stokkan from Sintef and Rune Søndenå from IFE were the co-supervisors.

The thesis consists of two main sections. The first section gives an introduction to the necessary theoretical concepts and an overview of the current state of knowledge concerning the defect-impurity interactions in High Performance Multicrystalline silicon (HPMC Si). Additionally, a description of the experimental techniques used in this work are presented. The second section contains the published articles and submitted manuscripts. The following works are included in the second section:

Article I:

Grain boundary effect on lifetime in high performance multicrystalline silicon during solar cell processing

K. Adamczyk, R. Søndenå, M. Mhamdi, A. Autruffe, G. Stokkan, M. Di Sabatino, 2016, Physica Status Solidi C, vol. 13, issue 10-12, p. 812-815

Article II:

The effect of phosphorus diffusion gettering on recombination at grain boundaries in HPMC-Silicon wafers

M. S. Wiig, K. Adamczyk, H. Haug, K. E. Ekstrøm, R. Søndenå, 2016, Energy Procedia, vol. 92, p. 886-895

Article III:

Recombination strength of dislocations in high-performance multicrystalline/quasi-mono hybrid wafers during solar cell processing

K. Adamczyk, R. Søndenå, C. C. You, G. Stokkan, J. Lindroos, M. Rinio, M. Di Sabatino, 2018, Physica Status Solidi A, vol. 215, issue 2, p. 1700493

Article IV:

Recombination activity of grain boundaries in high-performance multicrystalline Si during solar cell processing

K. Adamczyk, R. Søndenå, G. Stokkan, E. Looney, M. Jensen, B. Lai, M. Rinio, M. Di Sabatino, 2018, Journal of Applied Physics, vol. 123, issue 5, p. 055705

Article V:

Guidelines for establishing an etching procedure for dislocation density measurements on multicrystalline silicon samples

K. Adamczyk, G. Stokkan, M. Di Sabatino, 2018, MethodsX, vol. 5, p 1178–1186

Other contributions, not included in the thesis:

Defects in multicrystalline Si wafers studied by spectral photoluminescence imaging, combined with EBSD and dislocation mapping

T. Mehl, M. Di Sabatino, K. Adamczyk, I. Burud, E. Olsen, 2016, Energy Procedia, vol. 92, p. 130

Impurity control in high performance multicrystalline silicon

G. Stokkan, M. Di Sabatino, R. Søndenå, M. Juel, A. Autruffe, K. Adamczyk, H. V. Skarstad, K. E. Ekstrøm, M. S. Wiig, C. C. You, H. Haug, M. M'Hamdi

Acknowledgements

The work described here is important to me, and I view it as a large project. The very nature of such projects requires teamwork, it's an effort of many different people and even more influence it. I'm not naming many who helped, but I need to name at least the selected few:

Great thanks to my supervisors: Marisa Di Sabatino, Gaute Stokkan and Rune Søndenå. You gave me an opportunity to take up this challenge, you guided me during the way and with your help I got to a point where it is actually finished. I learned a great deal from you. Thank you for this.

In the same vein I'm grateful to Markus Rinio, who greeted me to his lab and shared his knowledge. He and Jeanette Lindroos helped me a lot during my stay at Karlstad University, where I made the LBIC measurements forming a large part of this thesis.

I'm of course also very thankful for the warm support I received from the team at NTNU. A special thanks goes to my colleagues: Antoine Autruffe, Adeline Lanterne, Xuemei Cheng, Daniele Casari, Guilherme Gaspar, Kai Erik Ekstrøm and Espen Undheim.

I'm very grateful to Jarosław Jabłoński and the team at Topsil, from whom I learned a great deal about silicon before coming to Norway, and from whom I'm still learning after coming back to Poland. I think I would not be chosen for this work without your help, and finishing it would be much more difficult without your trust.

Na koniec podziękowania trochę bardziej osobiste. Bardzo dziękuję moim rodzicom i mojej siostrze. Pomogliście mi wejść na tę drogę i się na niej utrzymać. Bez Was nie dałbym rady.

Osobne i specjalne podziękowania dla Agaty. Wielokrotnie pokazywałaś mi, że jest świat poza tym wąskim kawałkiem, do którego go samemu ograniczałem. Często prowokowałaś mnie do robienia rzeczy wymagających ode mnie wiele wysiłku. Najczęściej okazywało się, że było warto. Przetrwaliśmy razem tę przygodę. Teraz czas na następne.

Trondheim, October 10th 2018,

Krzysztof Adamczyk

Table of contents

Preface i

Acknowledgements v

Table of contents vii

1. Introduction 1

1.1 Motivation 2

1.2 Outline 4

2. Theoretical background and literature review 5

2.1 Basics of solar cell operation 5

2.2 Recombination mechanisms 8

2.3 Crystalline silicon 11

2.4 Impurities 21

2.5 Defect-impurity interactions 30

3. Experimental techniques 45

3.1 Solidification and wafer processing 45

3.2 Characterization techniques 45

3.2.1 Microwave detection of photoconductive decay - µPCD 45

3.2.2 Photoluminescence - PL 47

3.2.3 Light Beam Induced Current - LBIC 47

3.2.4 Electron Backscatter Diffraction - EBSD 49

3.2.5 Selective etching 50

3.2.6 PVScan and microscope analysis 52

3.2.7 Secondary Ion Mass Spectrometry – SIMS 53

3.2.8 Neutron Activation Analysis - NAA 54

3.2.9 Micro X-ray fluorescence - µXRF 55

3.3 Modelling 55

4. Summary of the publications within the four main topics investigated in this PhD thesis 57

4.1 Effect of grain boundaries on lifetime 57

4.2 Recombination strength of dislocations 58

4.3 Recombination activity of grain boundaries 58

4.4 Selective etching and dislocation density measurements 59

References 61

1. Introduction

In 2015, on the 12th of December, 194 countries and the European Union signed the Paris Agreement aimed, among others, at "holding the increase in the global average temperature to well below 2°C above pre-industrial levels and pursuing efforts to limit the temperature increase to 1.5°C above pre-industrial levels, recognizing that this would significantly reduce the risks and impacts of climate change" [1]. Roadmaps for a 100% renewable global energy mix which would help in meeting these targets were drafted [2]. Photovoltaic devices provide about 48% of energy in this projected mix, and according to the roadmap authors this is economically and technically feasible. It is estimated that in 2017 the share of renewable energy technologies in global electricity production was about 26.5%, with only 1.9% of this global share produced with photovoltaics [3]. Year 2017 was, however, the second one when PV accounted for more added power capacity than any other generating technology [3, 4].

It is crystal clear to the majority of the scientific community that global warming is happening and that it is related to human activity [5]. It can be expected that well informed governments aided by this community will try to react, just like they did with the Paris Agreement, when global warming is starting to be seen as a threat to global commerce [6]. The changes induced by global warming are also seen by multinational corporations. Shell estimates that current "mature" solar PV technologies can become the largest single primary energy source in 2060, accounting for about 40% of primary energy [7]. Statoil/Equinor also draws scenarios in which even in the most conservative case renewable energy share in the energy mix is considerably increasing [8]. Yet social and political barriers for a wider PV adoption still remain. In order to overcome them, the scientific and industrial community can make an important contribution to explain the required energy transition better, pursue smarter energy policies, and make solar power technology cheaper and more efficient.

Currently the main focus of the photovoltaics industry is on silicon-based devices, with 95% of the market share for this material [9]. Multicrystalline silicon takes about 62% of the total solar cell production. The current efficiency of solar cells made from monocrystalline silicon is reported to be 26.7% ± 0.5%, while the current record for multicrystalline silicon cells is at 22.3 ± 0.4% [10]. Record terrestrial module efficiencies are about 2% point smaller for each case, and the efficiencies of commercial modules are again lower, close to 19% for monocrystalline and 16-17% for multicrystalline modules. The reason why multicrystalline cells are dominating the market even with their lower efficiency is related to their production cost. While monocrystalline cells have higher efficiencies, the process of monocrystalline growth, the Czochralski process (CZ), requires more energy and has a lower throughput than the process of directional solidification used for multicrystalline material growth. In October 2018 the average price of a full 156 mm x 156 mm mono wafer is about 0,39 $ to 0,28 $ for a multi wafer [11]. This difference in price in many cases offsets the difference in final module efficiency and is the main driving force behind the current multicrystalline material dominance. With the current industrial mindset of cost reduction, the production processes need to be constantly improved. The International Renewable Energy Agency estimates that even with the outstanding price reductions of PV systems in the last few years, and with the current focus on reducing the costs of "Balance Of System", including the inverter, electrical and structural elements supporting the module, there still is a potential to reduce the price of PV modules and cells [12]. Achieving this requires a better understanding of the structure of multicrystalline silicon and the changes it undergoes in the production process.

1.1 Motivation

Multicrystalline silicon is usually grown by directional solidification. The nature of this process is that the nucleation in the melt starts near the bottom of a crucible and occurs in a controlled, but random manner. The growth proceeds towards the top of crucible, and a great deal of effort is put into controlling the growth front [13, 14]. This results in a structure containing multiple grains divided by grain boundaries, and with dislocations emitted in the structure in areas where the thermal stresses were sufficiently high to plastically deform the crystal grains in the high temperatures shortly after crystallization [15]. Both grain boundaries and dislocations are known to be detrimental to the final solar cell performance, and they are one of the main reasons why using monocrystalline silicon without grain boundaries and with much smaller dislocation densities leads to higher cell efficiencies. Dislocations are viewed as more detrimental, but recent developments in growth control showed that their density in the final material can be reduced by changing the grain boundary structure [16].

Structural defects mostly affect the cell efficiency when they are decorated with impurities [17]. Impurities are mainly introduced during the crystal growth process and thus during the ingot making. The feedstock used for photovoltaic silicon growth already contains some impurities, but the crucible is their main source in multicrystalline ingot growth. In directional solidification used for multicrystalline silicon metal impurities from the crucible can diffuse both into the silicon melt and ingot [18]. Special coatings are used to limit this diffusion process, however they can also act as impurity sources. Impurities such as carbon and oxygen can come from the furnace atmosphere, where they are introduced from quartz crucible and graphite furnace elements heated close to the melting temperature of silicon [19, 20].

The distribution of impurities introduced into the ingot during the solidification process is established during its cooldown phase. When the temperature decreases, the diffusivity and solubility of impurities also decreases, leading to precipitation on preferred nucleation sites such as dislocations and grain boundaries. The next step in the standard solar cell production chain having a considerable effect on the impurity concentration and distribution is the phosphorus diffusion gettering, where the emitter layer is created by in-diffusing phosphorus into the wafer from a gaseous source [21]. During this step the fast diffusing metal impurities are partially gettered in the emitter layer, where they are not as harmful as in the bulk. Finally, during the contact firing step occurring in the presence of hydrogen rich antireflection layers, such as a SiN_x layer, bulk defects are passivated with hydrogen [22]. These high temperature processes influence the concentration of impurities, how they are distributed in the material and how they are affecting the final device performance.

In this context, the main motivation of this work was to obtain a better understanding of the processes and interactions between structural defects, such as dislocations and grain boundaries, and the impurities present in multicrystalline silicon for photovoltaic applications. To keep this relevant for industrial applications, these interactions were studied in the context of state-of-the-art processes used in commercial solar cell production. We have investigated wafers from the two currently most relevant multicrystalline solidification techniques, e.g. mainly from the high performance multicrystalline (HPMC) material, but also from quasi-mono (QM) silicon. We have looked at the defect-impurity relations in the as-grown state as well as during the solar cell processing steps with a high thermal budget, that is gettering and hydrogenation.

1.2 Outline

This thesis is divided in two parts. The first part has four chapters which allow for a better understanding of the theoretical background and experimental methods used in this work and, thus, give a better understanding of the five scientific manuscripts forming the second part of this thesis.

Chapter 1 briefly describes the global perspective on photovoltaics and sets the context of the thesis.

Chapter 2 presents a theoretical background necessary to understand the aims and scope of the thesis. It discusses basics of solar cell operation along with mechanisms of recombination limiting conversion efficiency. Crystalline structure of silicon, the techniques used to solidify it and the defects present in the solidified material are described, along with impurities. Finally this chapter contains the state of the current knowledge on defect-impurity interactions in silicon solar cell processing.

Chapter 3 lists the experimental techniques used for the presented study. The equipment and processing parameters used for ingot growth and sample preparation are described. Large part of this chapter is focused on the different techniques used to characterize the electrical properties of the material as well as its structure and composition. The chapter includes also a presentation of the Donolato model of recombination on dislocations on which part of the analysis is based [23].

With this introduction, Chapter 4 summarizes the publications included in this thesis and general conclusions from the different analysis steps are listed.

2. Theoretical background and literature review

2.1 Basics of solar cell operation

Solar cells operate on the basis of the photovoltaic effect, in which an electromotive force is produced between two layers of different materials as a result of irradiation [24]. For the photovoltaic effect to take place the two materials need to be semiconductors. Usually a semiconductor is defined as a crystalline solid with an electrical conductivity intermediate between that of a conductor (up to 10^9 S m^{-1}) and an insulator (as low as 10^{-15} S m^{-1}) [25], but a better understanding of the photovoltaic effect can be achieved by explaining semiconductors in terms of band theory. When atoms are joined together to form any material, their electron orbitals start to overlap and their allowed energy levels spread out to create energy bands. In conductors the conduction band in which electrons are free to change energy states with very small excitation is usually joined with the valence band full of occupied energy levels, where electrons stay in their bonds due to neighboring states also being occupied. In insulators and semiconductors these two bands are separated by a band gap. In insulators this band gap is in the range of several eV, and electrons can move to the conduction band only with high energy excitation, which occurs only in cases of the insulator breaking down. This description for semiconductors and insulators is valid in 0 K, at which all the states above a certain Fermi energy characteristic for a given material are free, and all the states below are occupied. At higher temperatures, the thermal energy is enough for a small part of electrons to be excited to the conduction band. In semiconductors the band gap is typically in the range of 0.5-3 eV [26].

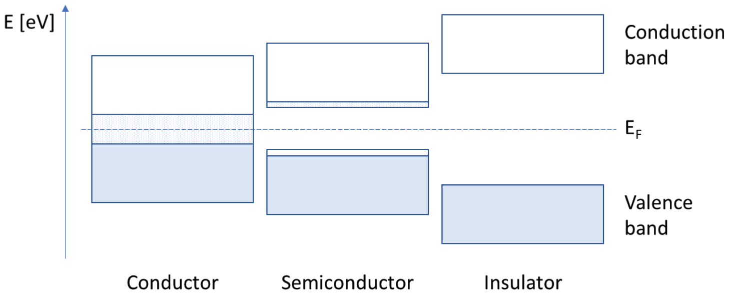

Figure 1. Band structure of conductors, semiconductors and insulators in temperatures above 0 K. The shaded area represents the excited electrons.

The band gap of silicon is about 1.1 eV. Heating a semiconductor leads to an excitation of more charge carriers and a higher conductivity, even though the lattice vibrations scattering the charge carriers are also stronger. Photons with energies above 1.1 eV, that is with wavelength below 1127 nm can also excite electrons from the valence band to the conduction band in silicon. Semiconductor materials are then distinguished by the ease with which their electrical properties can be controlled, in a sense that thanks to their band gap structure their conductivity can be controlled by temperature or irradiation.

When an electron is excited to a higher energy level across the band gap, it leaves behind a positively charged vacancy, which can be filled again by other electrons. When an electron from a neighboring atom fills the vacancy, the vacancy then moves to this neighboring atom, and it can now be viewed as a free, positive charge carrier, called an electron hole. Many useful analogies have been made to portray how hole movement occurs, comparing it for example to the movement of an empty seat in crowded auditorium.

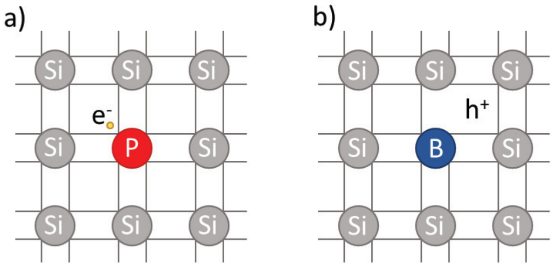

Figure 2. Two diagrams showing a 2D silicon lattice doped with a phosphorus atom in a) and with a boron atom in b).

Another way to control the conductivity in a semiconductor is doping, which is the process of adding a finite amount of impurities to introduce energy levels in the band gap, close to the band gap edges. Ideally clean, intrinsic silicon creates a configuration in which each atom bonds with four other atoms, resulting in a complete electron octet. Elements with three or five valence electrons are used for doping. Phosphorus is an atom with five valence electrons. When it replaces a silicon atom it adds the fifth electron as a free charge carrier, not bound by neighboring atoms. Phosphorus in this case is a donor. Doping with phosphorus will then increase the conductivity of the material by increasing the negatively charged carrier density, hence silicon doped with phosphorus is called n-type, and the electrons are the majority charge carriers in such material. Boron, a dopant most commonly used in growth of silicon ingots for photovoltaic applications, has three valence electrons. Adding a boron atom results in a situation where it will share only one bond with one of the neighboring silicon atoms. This results in a hole in the electron structure. Boron acts as an acceptor when it allows the hole to move by accepting an electron from a neighboring atom. Silicon doped with boron will conduct by positive hole transport and is called p-type. Holes are in this case the majority charge carriers.

A solar cell in its most basic form requires a p-n junction, that is an interface between a layer of p-type and a layer of n-type material. When two such layers are joined together, an electrostatic potential, and thus an electric field is established between them. What happens is that a hole and electron concentration gradients are created by joining materials with different densities of these carriers. Holes diffuse from p-type to n-type, and electrons diffuse in the opposite direction. This leaves the acceptor atoms in the p-type, and donor atoms in the n-type side ionized. Acceptors in the p-type side are negatively ionized, because they accepted additional electrons, and the donors in n-type are positively ionized, because they donated one of their valence electrons. These atoms, fixed in their positions, create a fixed charge distribution and hence an electric field, affecting the movement of free charge carriers. This electric field opposes the diffusion of holes and electrons, and in equilibrium they cancel each other out. A depletion layer is created near the interface, where the density of free charge carriers is reduced, and in which a free charge carrier will be swept to one side by the electric field, depending on its charge. An electron is swept to the n-type side, a hole to the p-type side.

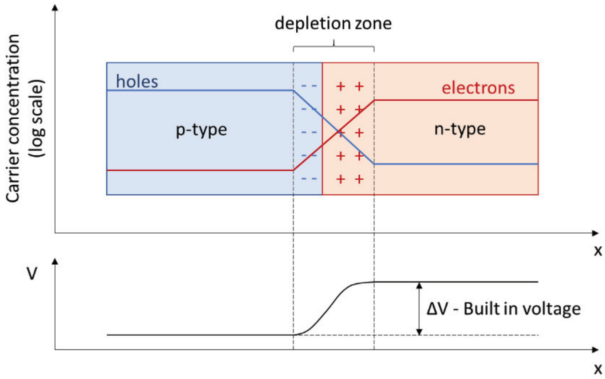

Figure 3. A p-n junction with marked depletion zone and hole and electron concentration (top), and a simplified plot of the voltage built at the junction (bottom).

The photovoltaic effect defined in the beginning of this section can now be explained as an effect occurring between two layers of p- and n-type material joined together, essentially over a p-n junction. When such a junction is illuminated and part of the light is absorbed by the material, the photon with energy larger than the band gap excites an electron from the valence to the conduction band. There is a chance that the free, excited electron will move to the depletion zone, where it will be swept to the n-type layer and extracted to the external circuit. In this manner the energy of the photon is directly converted to electric potential, which can then be applied to the external load.

The photovoltaic effect requires three steps. Light needs to be absorbed by the solar cell material, generating an electron-hole pair. The electron-hole pair needs to be separated. Finally, charge carriers need to be extracted to an external load. Each of these steps creates multiple challenges for solar cell design and manufacturing, and as such are important fields of research. This thesis is mostly concerned with defects and impurities which decrease the probability that a charge carrier pair will be successfully separated. To understand how it is related with solar cell operation, a discussion of recombination is necessary.

2.2 Recombination mechanisms

Recombination is the main factor limiting solar cell efficiency. When a photon is absorbed in a semiconductor, its energy excites an electron from the valence band to the conduction band This is called generation. Generation leads to an excess of both majority and minority charge carriers. An opposite effect where a hole from the valence band recombines with an electron from the conduction band can also occur. The frequency of this recombination depends on the concentration of both types of carriers, but mostly on the concentration of excess minority charge carriers. In a p-type material with electrons as minority charge carriers, the excess minority charge carriers are labeled as Δn and the rate of recombination U can be expressed as:

$$U = \frac{\Delta n}{\tau} \qquad (2.1)$$

where τ is the lifetime of excess minority carriers, simplified as minority carrier lifetime or lifetime. Lifetime is an important parameter for the solar cell material, describing its quality.

There are three main mechanisms by which recombination happens: radiative, Auger and Shockley-Read-Hall (SRH). These mechanisms are schematically illustrated in Figure 4. The first one, radiative recombination, is the exact opposite of photon absorption. An electron relaxes from the conduction band to the valence band and emits a photon with energy equal to the band gap. Radiative recombination is the main mechanism limiting the cell efficiency of ideal solar cell without any defects. The theoretical limit of silicon solar cell efficiency is about 29%, thus the current record of 26.7% in a monocrystalline cell is a good result [10, 27, 28]. The defects present in commercially available multicrystalline silicon solar cells are the cause of lower efficiencies in commercial cells and thus require more attention.

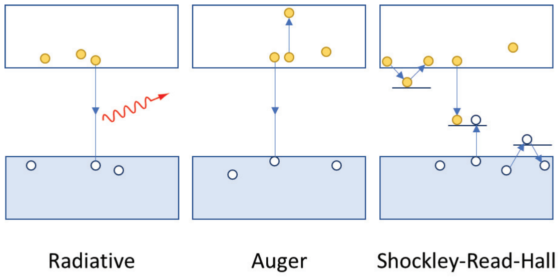

Figure 4 Main mechanisms of recombination: radiative band-to-band, Auger and Shockley-Read-Hall. The diagram for SRH recombination shows also the process of electron trapping and detrapping close to the conduction band, and of analogous hole trapping and detrapping close to the valence band.

Auger recombination occurs by transferring the energy of the relaxing charge carrier to an another carrier of the same type and exciting it to higher energy levels. In the example presented in Fig. 4 an electron recombines with a hole and the released energy is transferred to a second electron in the conduction band, resulting in its larger excitation. The excessive energy of the excited electron is quickly released to the lattice as thermal vibrations – phonons, and the electron relaxes to energy levels close to the conduction band edge. The process in which the energy of an electron excited to states deeper in the conduction band relaxes to its edge and releases energy as thermal vibrations, or an analogous process for holes, is called thermalization. Thermalisation occurs much faster than recombination. While thermalisation requires femtoseconds, the lifetime of separated charge carriers is of the order of microseconds. Auger recombination is an important mechanism particularly when the free charge carrier concentration is large, that is when the material is highly doped, operates at high temperature or in conditions of high injection, when the generation rate is high.

Shockley-Read-Hall recombination is the most important mechanism as far as this thesis is concerned, and it can be said that it is the most important mechanism in multicrystalline silicon-based solar cells. It involves defect energy levels on which the recombination occurs. Holes and electrons can relax to such energy levels positioned in the band gap, and recombine on them instead of relaxing all the way over the band gap. Both defects and impurities introduce such energy levels into the forbidden band gap, and their exact position in the electronic structure depends on the type of the defect. Defect states are usually spatially localized on structural defects in the crystalline lattice, thus they can act as traps capturing mobile electrons and holes. When such a state has an energy level close to the valence or conduction band, the probability that a trapped charge carrier will be excited again to its respective band, that is detrapped, is larger than that it will recombine with a carrier of opposite charge. Because of this defect states close to the valence or conduction band more often act as temporary traps for charge carriers and recombination occurs rather on states deep within the bandgap.

The rate of recombination on traps can be expressed as:

$$U_T = \frac{np - {n_i}^2}{\tau_{h0}(n+n_1) + \tau_{e0}(p+p_1)} \qquad (2.2)$$

where τ_{h0} and τ_{e0} are lifetime parameters depending on the type and volume density of trapping defects; p is the number of holes in the valence band per unit volume of the crystal; n is the analogue of p for electrons in the conduction band; n_i is the intrinsic carrier concentration, that is the concentration of charge carriers in an undoped, perfect semiconductor; and finally n_1 and p_1 are parameters introducing a dependency of the recombination rate upon the energy of the trapping level, E_t:

$$n_1 = N_c \exp\left(\frac{E_t - E_c}{kT}\right) \qquad (2.3)$$

$$n_1 p_1 = {n_i}^2 \qquad (2.4)$$

N_C is constant at a fixed temperature T and it is known as the effective density of states in the conduction band, E_C is the energy of the conduction band edge, and k is the Boltzmann's constant ($k = 1.38 \times 10^{-23}$ J/K) [29].

Equation 2.2 demonstrates what was mentioned above, that the defect levels leading to largest recombination rates lie deep in the band gap, i.e. near its middle. This means that impurities and structural defects introducing such levels are strong recombination centers limiting the minority carrier lifetime, and thus limiting the efficiency of the device.

Except for bulk structural defects such as dislocations and impurities, such deep levels are introduced to the forbidden band gap by the surfaces of the semiconductor and by interfaces between its different parts. This means that the surfaces of the device along with grain boundaries also can provide localized recombination centers. Since these defects are two-dimensional in nature, the recombination rate U on them is often described in terms of surface recombination velocity:

$$U = \frac{S_{e0}S_{h0}(np-n_i{}^2)}{S_{e0}(n+n_1)+S_{h0}(p+p_1)} \qquad (2.5)$$

where S_{e0} and S_{h0} are electron and hole surface recombination velocity, respectively. As opposed to lifetime, the higher the surface recombination velocity, the poorer the performance of a device limited by it.

2.3 Crystalline silicon

The preceding discussion of silicon solar cells and recombination and trapping on defect states was developed for crystalline material. When multiple silicon atoms are joined, they create a crystalline material defined as a solid composed of atoms arranged in a three-dimensionally periodic pattern. This periodicity can be described with a unit cell, which can then be used to re-create the full crystal by translation. The number of systems in which atoms can arrange to form crystals is limited. Eventually all crystal lattices can be described with seven basic systems. Semiconductors such as silicon, germanium and gallium arsenide belong to the simplest system, i.e. the cubic system.

The cubic system is defined with a cubic unit cell, with three equal axes at right angles. The silicon crystal lattice is called face-centered cubic (fcc). In such a cell the lattice points can be found in each corner of the cell and in the middle of each wall. As mentioned before, silicon creates a structure in which each atom bonds with four other atoms. In the crystal lattice this means that each of the lattice points is occupied by a tetrahedron with a silicon atom at its center, and four other silicon atoms in its corners. The result of constructing a face-centered cubic cell with such tetrahedrons is the structure visible in Figure 1 a), called the diamond lattice unit cell. Due to this structure the material is anisotropic. It can be easily understood when looking from different directions at a few unit cells assembled together, just as in Figure 1 b), c) and d). Such directions can be defined as unit vectors within the coordinate system of the unit cell. Crystallographic planes are also defined with the unit cell. Thanks to the regularity of the cubic system a crystallographic plane in it is described with the same coordinates as the coordinates of the crystallographic direction perpendicular to this plane.

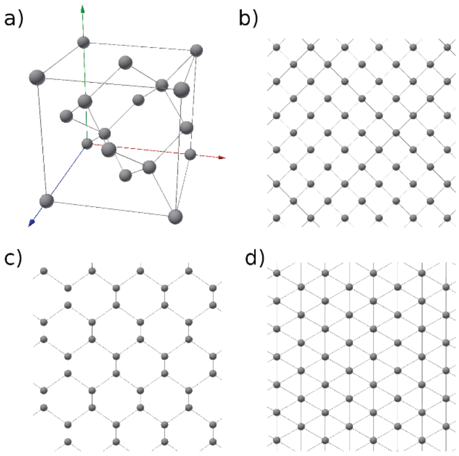

Figure 5. a) The silicon unit cell and a view of three crystallographic planes important for the semiconductor industry: b) (100), c) (111), d) (110).

Table 1. Crystal defects in silicon [30].

Geometry	Defects
Point	Intrinsic point defect
	Vacancy
	Self-interstitial
	Extrinsic point defect
	Substitutional impurity atom
	Interstitial impurity atom
Line	Dislocation
	Edge dislocation
	Screw dislocation
	Dislocation loop
Plane	Stacking fault
	Grain boundary
Volume	Precipitate
	Void

The perfect crystalline lattice is only a model, just as the related band model of the crystal's electronic structure. Real crystals are full of defects introducing defect states into the band gap. The defects can be classified according to their geometry, as listed in Table 1. The point defects are related to inconsistencies in the crystal lattice on the scale of one atom. Line defects occur when the discontinuity in the lattice can be described as a line, such as a dislocation line, and plane defects relate to surfaces such as grain boundaries and stacking faults. Volume defects can be for example larger, three-dimensional precipitates or clusters of one-dimensional vacancies. In addition to these defects, dangling bonds should be mentioned, as they are also related to trapping and defect states. Dangling bonds can be found at the crystal surface or at the surfaces which break the crystal lattice, such as grain boundaries.

2.3.1 Point defects

In thermal equilibrium a small fraction of atoms leave their exact lattice positions and occupy spaces between the lattice points. Such atoms are called interstitials. The unoccupied lattice position is a vacancy. Both of these are intrinsic point defects. Intrinsic point defects play a major role in monocrystalline silicon, where grain boundaries are absent and dislocations can be found in very low densities. Interstitial silicon atoms are for example generated at the interface of an oxide growing on silicon or near oxide precipitates growing in the bulk and they affect the diffusion of impurities through the material. In monocrystalline material the concentration and type of point defects depends on the temperature gradient at the solid liquid interface and the crystal growth rate. Intrinsic point defects are not electrically active.

Extrinsic point defects are impurity atoms, either substitutional atoms on a lattice point, or interstitial atoms in spaces between the regular atoms of the matrix. Impurities will be discussed in subsequent chapters.

2.3.2 Line defects

Dislocations are one-dimensional defects in crystals, and they can be understood as incomplete planes of atoms in the crystal lattice. The line defect is then the edge of the plane where it is incomplete. There are two types of dislocations, the edge and the screw dislocation. The differences between these types can be seen in Fig. 6. Dislocations are created during crystal growth and by plastic deformation of the crystal. Their move during such deformation is the main mechanism of stress relaxation when the material is in temperatures high enough to allow it [31].

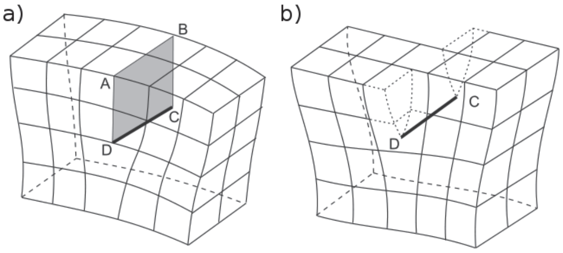

Figure 6. a) Positive edge dislocation, b) Left-handed screw dislocation. Taken from [32].

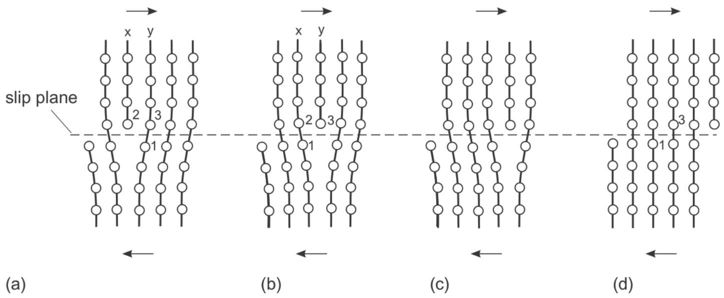

Figure 7. Movement of an edge dislocation - glide. Taken from [33].

Dislocations are defined by their line direction vector l and their Burgers vector b. The Burgers vector for a given dislocation is obtained when an atom-to-atom path is constructed in a crystal around a dislocation, and when the same path is then constructed in a perfect lattice. Due to the nature of the defect, the path will not close, and the vector needed to close it is the Burgers vector [32]. Straight dislocation lines end on the surface of the material or on grain boundaries, but dislocations can also exist in the bulk in the form of dislocation loops with both screw and edge segments.

As seen in Fig. 7, glide, the mechanism of movement of an edge dislocation is relatively simple. It makes this type of dislocation extremely mobile in specific crystal planes and crystal directions. Glide of many dislocations can be referred to as slip. The crystal planes along with crystal directions allowing most mobility are called slip systems. They are in most cases characteristic for the crystal lattice, but the activation of a specific system depends also on the direction of the applied stress. The general rule is that dislocations are most mobile in the most densely packed planes, thus for the diamond lattice this means the {111} slip planes with <110> slip directions. <110>a/2 is then the shortest Burgers vector possible in the {111} system, where a is the silicon lattice constant, that is the main dimension of the silicon unit cell: a = 5.43095 Å [30]. Edge dislocations are limited to one slip plane only, while screw dislocations can perform cross slip, where they change the plane on which they glide.

Dislocations in silicon are mobile above a certain temperature, reported to be between 500°C and 1000°C depending on the strain applied to the material [34]. Below this brittle-to-ductile transition temperature they are immobile and the material is brittle, making it very easy to fracture a silicon wafer. Increasing the temperature, however, allows not only for glide, but also for a different dislocation movement mechanism, climb. Dislocations can climb on planes outside of their crystal slip systems, but this requires vacancies or interstitials to diffuse to the dislocation line and create jogs. A schematic of this type of dislocation movement along with a dislocation line with jogs can be seen in Fig. 8. When jogs occur in the slip plane, they are called kinks. Kinks are often created to reduce the dislocation energy by allowing different segments of the dislocation to lie in energetically preferable directions, while the kinks themselves become the high-energy segments. Dislocations moving by glide or climb interact with themselves and with other crystalline defects. When dislocations with a Burgers vector of an equal value and opposite direction meet, they annihilate. Dislocations moving along different planes can create kinks and jogs on each other. In an irregular array of dislocations some can lie partially in their slip planes, and partially in different planes, and the segment capable of glide can then act as a source for further dislocations. Such a source is called the Frank-Read source [35].

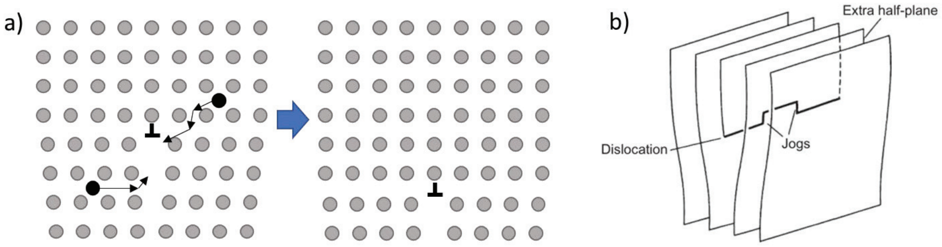

Figure 8. a) Dislocation move by climb, b) dislocation with jogs created by climb. b) taken from [33].

When a network of dislocations is present in the material its energy is increased and it’s a metastable state. When additional energy in the form of high temperature is available, dislocations undergo the recovery process which ends with polygonization [36, 37]. During the recovery process defects in the material rearrange to lower energy configurations, part of the defects annihilate and as the name suggests the resulting material is ‘recovered’ to a state closer to a perfect crystal. This affects both point defects and dislocations, but the grain boundary structure, especially its part consisting of large angle grain boundaries, is not affected. The final phase of recovery is the polygonization process, in which dislocations realign into a network of small angle grain boundaries.

While some types of dislocations are considered to have fully reconstructed cores and don’t introduce deep defect states [38], some others can be understood as dangling bonds arranged in a line in the crystal. Such dislocations would introduce defect states into the bandgap [39]. The density of dislocations is an important factor for the effect of dislocations on such parameters as lifetime or cell efficiency [40-43]. Also the contamination levels in the vicinity of a dislocation is important [44-46]. Clean dislocations can introduce defect states into the band gap, but they become much more harmful when decorated by impurities such as Fe or Ni. This ‘decoration’ can occur in the form of Cottrell atmospheres of interstitial impurity atoms diffusing to the dislocation due to its stress fields. These fields are naturally occurring because of the lattice displacement on a dislocation, and the expanded or contracted or lattice attracts the interstitials [47]. Impurity precipitates can also nucleate on dislocations [48].

2.3.3 Plane defects

The most common two-dimensional defects include stacking faults and grain boundaries. Stacking faults can be understood as errors in the stacking of atom planes with highest density. In the diamond lattice this is the (111) planes, and in a perfect silicon crystal they would be stacked according to an ABC pattern, each of these three shifted into a different position in relation to its neighboring planes. When the stacking is imperfect, and for example an ABABC structure is created, this type of defect is called a stacking fault [30]. It is common in the semiconductor industry, where oxidation is often used in the device manufacturing process. As mentioned before, oxidation causes an emission of interstitial atoms and these interstitials can combine into a stacking fault, causing a defect known as oxidation induced stacking faults [49]. While a native oxide layer is created on silicon during contact with water or in oxygen-atmosphere [50], and silicon oxide is routinely used for solar cell surface passivation and can give high device efficiency [51], stacking faults are a minor problem in multicrystalline silicon used for solar cells, especially when compared to the second plane defect mentioned Table 5, that is grain boundaries.

As the name suggests, multicrystalline material consists of multiple crystals. In a material consisting mostly of one phase, such crystals are called grains and each interface between two grains of the same phase is a grain boundary. Grain boundaries have a thickness of a few atomic distances, and their arrangement depends on the orientations of the two grains they separate. The relationship of the two grains can be described with a rotation by a specific, smallest possible angle θ, the misorientation angle, around a specific axis. The misorientation angle can be used to distinguish between two main types of grain boundaries: small-angle and high-angle grain boundaries. It has been reported that grain boundaries with misorientation angle below 10-15° are small-angle and above are high-angle, though this limit is quite spread in the literature [36, 52, 53].

Small-Angle Grain Boundaries (SAGB) can be approximated as rows of dislocations, spaced proportionally to the grain boundary misorientation angle. The distance between such dislocations can be calculated by a simple equation, presented along with a scheme of such a small-angle boundary in Fig. 9:

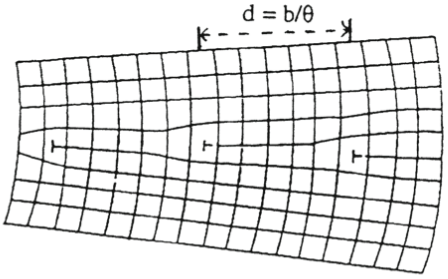

Figure 9. Scheme of a small-angle symmetrical grain boundary.
b is the Burgers vector, θ the misorientation angle Taken from [53].

In the most simple case a pure tilt or twist grain boundary can be distinguished in small-angle grain boundaries. Small-angle grain boundaries in which dislocations can be distinguished can be formed during the recovery process, especially during its final polygonization phase. Another proposed mechanism of small-angle grain boundary growth is during faceted growth of the crystal [54].

Grain boundaries with larger misorientation, the high-angle grain boundaries, cannot be explained with the dislocation model. At larger misorientation the distance between dislocations is reduced to the point where the dislocation cores overlap and a dislocation structure cannot be further resolved. This does not mean, however, that the structure of such grain boundaries is completely chaotic. The surface energy of grain boundaries depends highly on the misorientation angle, as can be seen in Fig. 10. After a sharp increase from 0° to about 15° the relative energy stays in a narrower range, and the local minima correspond to specific misorientation angles with which the grain boundary arrangement is preferred. To explain this behavior the Coincidence Site Lattice (CSL) model was introduced. In this model two grains can have a certain misorientation between them, but still have common lattice sites. The coincidence of the two grains lattices is then described by a coincidence index Σ, equal to the ratio of the density of atoms in the original lattice to the density of atoms in the coincidence site lattice [55]. A grain boundary between two such grains with a coincident lattice is called a CSL grain boundary and its type is defined by the coincidence index. Only certain coincidence indexes are allowed. The most common CSL grain boundary is a Σ3 boundary, also called a twin boundary. It can be the result of rotating a grain by 60° around a <111> axis, but also a rotation of 70.53° around <110>. Other common CSL boundaries are Σ9 and Σ27.

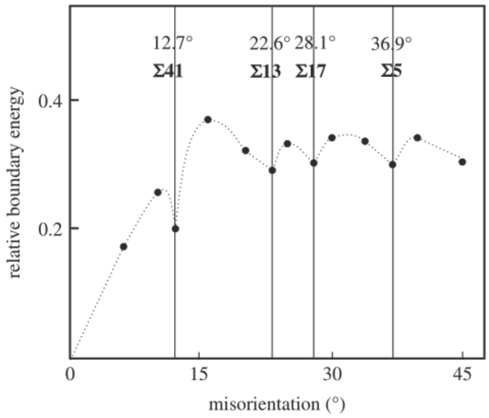

Figure 10. Relation between the misorientation angle and relative boundary energy of a [001] twist boundary in Cu. Taken from [52].

Different criteria can be used to decide the acceptable deviation from the perfect CSL orientation between two grains for which the grain boundary is 'special' [56-58]. The most popular is the Brandon criterion, where a grain boundary is classified as a CSL boundary with index Σ when its misorientation is within the tolerance of:

$$\Delta\theta = 15°\Sigma^{-\frac{1}{2}} \qquad (2.6)$$

from a perfect CSL orientation.

In the articles forming the core of this work, and in its other parts, the more restrictive Palumbo criterion is used unless stated otherwise. This criterion was found to separate different types of grain boundaries into categories correlating better with their properties [58-60]. With this criterion boundaries are classified as CSL when they are within tolerance of:

$$\Delta\theta = 15°\Sigma^{-\frac{5}{6}} \qquad (2.7)$$

High-angle grain boundaries which cannot be classified as CSL are termed random-angle grain boundaries.

The electrical activity of grain boundaries in silicon is a topic of high importance since polycrystalline material started to be used for solar cells [61-63]. It highly depends on the boundary structure and the level of contamination in its vicinity, with a general rule that the higher the contamination level, the larger the recombination at grain boundaries due to the effect of an increased impurity segregation [41, 64]. For small-angle grain boundaries, it was observed that electrical activity depends on misorientation. Chen et al. use the Electron Beam Induced Current (EBIC), a technique measuring the current induced in the material by an electron beam, and allowing to assess the recombination activity of extended defects. They show that this activity increases with increasing the misorientation angle from 0 up to 2°. This corresponds to a decreasing distance between the dislocations creating the small-angle grain boundaries – at 2° they are about 200 nm from each other. At larger misorientation, that is at smaller distances between the dislocations, the EBIC signal stabilizes, meaning that the areas affected by recombination at dislocations overlap. Small-angle grain boundaries are the most detrimental to solar cell efficiency according to this study, followed by Random-Angle Grain Boundaries (RAGB) [63]. Since the electrical activity is related to contamination on the grain boundary, grain boundaries introducing more stress into the lattice tend to attract impurities and also allow for their faster diffusion [53, 65]. For large-angle grain boundaries this means that the electrical activity will increase with increasing coincidence index, and that random-angle grain boundaries should show the largest activity in this group. This was in fact observed by Chen et al. for the case of as-grown silicon material and Karzel et al. for silicon wafers after different processing [66, 67]. An increased level of metal contamination was also correlated with grain boundary type in silicon material [68]. On the other hand clean, uncontaminated grain boundaries showed very little electrical activity, below 2% of EBIC contrast at room temperature [63]. Wang et al. proposed that shallow energy states were introduced by the inherent Σ3 <111> grain boundary structure and deep states acting as recombination centers were introduced at the grain boundary by impurities which segregated on it [69]. Σ3 grain boundaries show the lowest electrical activity of all studied grain boundaries, but their structure can also provide preferential nucleation sites for dislocations when they are macroscopically incoherent, that is they have dangling bonds in their structure due to a mismatch with the lattice. Cases of such incoherent Σ3 grain boundaries with dangling bonds or dislocation networks have been reported in literature [69, 70]. The mechanism behind this incoherency is that the orientation of the two grain boundaries can correspond to a Σ3 CSL, but the boundary plane orientation is different from the most common (111) plane and this leads to a macroscopically incoherent, faceted boundary plane, consisting of coherent segments, for example of planes (1-

12) and (211) [70]. Such faceted grain boundaries were also reported for higher coincidence index types, and it was proposed that they could act as sources of dislocations [71].

2.3.4 Volume defects

As mentioned in the previous sections, both dislocations and grain boundaries have a much stronger influence on electrical parameters of the solar cell, and on semiconductor devices in general, when they are decorated with impurities. Impurities can diffuse towards the defects and decorate them in form of solute atoms, but after a certain concentration above the solubility limit is reached, precipitate nucleation will occur [59, 72, 73]. Precipitates are usually intermetallic phases of the impurity and matrix elements. Precipitates are rarely coherent with the matrix lattice and because of this they introduce stress and dislocations into the material. The effect of precipitates on silicon electrical properties is relatively strong, and it also drew a lot of researchers` attention. Buonassisi et al. showed that the precipitate distribution needs to be carefully assessed when analyzing this effect [74]. Smaller, evenly distributed metal precipitates separated by small distances are more harmful, because they limit the minority carrier lifetime more than larger precipitates or clusters of small precipitates separated by larger distances. Morishige et al. analyzed how the main solar cell processing steps affect the distribution of precipitates and showed that even steps with a very limited thermal budget such as contact firing can lead to changes in their size and density [73]. A lot of effort has been made to quantify the effect of precipitates on the final cell properties [75, 76] and how they interact with other defects in the material [59]. With that said, most of the properties of precipitates in silicon depend on the precipitated element. The element on which many studies focus is iron, considered as the most harmful impurity in silicon solar cells. A more detailed discussion of the effect of precipitates will be possible in the context of particular impurities described in a subsequent section.

The second type of volume defect often found in silicon is a void. Voids are usually created during crystal growth and their presence in the crystal depends on the growth rate and viscosity of the melt [30]. While it has been reported that such voids or pinholes can be for example the cause of structure loss in Czochralski grown monocrystalline ingots [77], they are less important when it comes to the electrical properties of directionally grown multicrystalline silicon.

2.4 Impurities

Previous sections show that extended crystalline defects are usually considered a problem for semiconductor devices. When they are decorated with impurities they introduce deep recombination levels into the bandgap providing recombination centers and limiting the minority carrier lifetime. Because of this, a major effort has already been put into understanding the effect of different impurities on silicon [74, 78-80]. This understanding led to a simple categorization of impurities into dopants, light elements and metallic contamination [78]. Dopants are intentionally added into silicon to control its charge carrier nature and concentration. The most common dopant for p-type silicon is boron, and for n-type – phosphorus. Dopant and impurity levels in the silicon bandgap can be seen in Fig. 11 and the effect of different impurities on solar cell efficiency in Fig. 12.

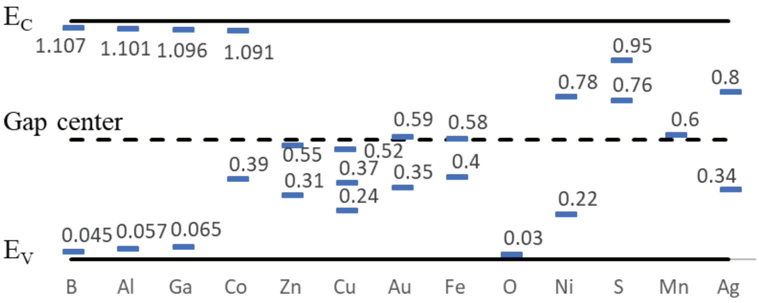

Figure 11. Silicon bandgap, 1.14 eV, with energies of impurity levels relative to the valence band edge energy, as in [29].

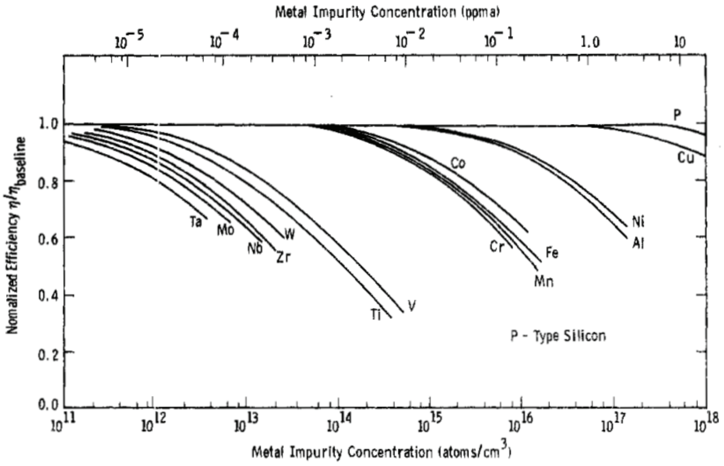

Figure 12. Solar-cell efficiency versus impurity concentration for 4Ω cm p-type CZ ingot. Taken from [80].

2.4.1 Feedstock

Impurities are incorporated into the material all along the production chain. The feedstock for silicon ingot growth can also be a source of impurities. Silicon feedstock is manufactured from quartz or quartzite. Depending on the deposit geographic location, various impurities can be present in the raw material, with iron, aluminium, titanium, calcium, cobalt, boron and phosphorus as the main ones [81]. This raw material is then reduced into silicon with carbon via a carbothermic reaction. Coal, coke, charcoal or woodchips can be used as the reducing agent, and they also introduce impurities such as boron or phosphorus, calcium, sulfur and carbon. The electrodes used in this reaction can also introduce impurities, just as all the furnace elements with direct contact with silicon in subsequent operations or even the handling equipment. Carbothermic reduction of silicon oxide leads to metallurgical grade silicon of about 98-99% purity (up to 2N – 2 nines), often labeled as MG-Si. The energy cost of such material is between 11 and 13 kWh/kg [82]. The standard way to higher purity feedstock for the semiconductor industry leads through a reaction of powdered MG-Si and HCl to obtain gaseous $SiHCl_3$, trichlorosilane or TCS. It is then refined and deposited on thin polysilicon rods. This procedure is called the Siemens process [83]. The Siemens process can give silicon purity of about 10N (nines up to the eighth decimal place, corresponding to a contamination level of about 0.1 ppbw). One of the main drawbacks of the Siemens process is that it requires a large energy input, above 80 kwh/kg for Solar-Grade silicon (SoG-Si), that is more than 7 times the energy cost of MG-Si [84, 85]. Recently, alternative routes for silicon purification have been developed and are gaining market share. The Fluidized Bed Reactor (FBR) process is one such alternative [86]. The FBR process uses silicon granules in a fluidized bed instead of the polysilicon rods. The Siemens process requires heating of the polysilicon rods for silicon deposition and simultaneously cooling the reactor walls to avoid deposition there. The rods need to be changed for each process. The fluidized bed allows to avoid energy losses related with these factors and requires about 50 kwh/kg of SoG-Si – about 60% of the energy needed in the Siemens process [85]. It is worth mentioning that while the polysilicon rods from the Siemens process need to be crushed into proper feedstock, the output from FBR is already in form of granules, which also contributes to the lower energy cost. Finally, it is worth mentioning that solar cells with reasonable efficiencies have also been manufactured from feedstock obtained by metallurgical purification of the MG-Si [87, 88]. Silicon feedstock obtained by these routes is called Upgraded Metallurgical-Grade silicon (UMG-Si). Currently the feedstock used by the industry for large scale production comes from the Siemens and FBR processes.

While different manufacturing routes lead to different cleanliness levels of the feedstock, it is generally assumed that feedstock used for photovoltaic silicon, especially polysilicon from the Siemens process and solar grade from FBR, is not the main impurity source for the final material. The main sources of impurities can be found in the crystallization process.

2.4.2 Impurity sources in crystallization

Crystallization defines the impurity concentration and distribution in the ingot. As mentioned in the introduction, there are currently two main routes for silicon crystallization for photovoltaic applications: the Czochralski process and directional solidification, closely related to the Bridgeman process. The principles of these processes can be seen in Fig. 13. In the Bridgeman process the ingot is grown starting from the bottom of the crucible, and the temperature gradient is introduced by pulling the crucible out of the hot zone. When there is no seeding at the bottom of the ingot, heterogeneous nucleation on the crucible walls leads to a polycrystalline structure. The main modification in directional solidification is that the temperature gradient is obtained not by pulling the crucible, but by opening and careful control of special heat sinks below the crucible bottom. In the Czochralski technique a monocrystalline seed is dipped in the melt and then pulled up, so that the growth interface is very close to the level of the melt-atmosphere interface. The pulled ingot and the crucible are rotated in opposite directions during the process. The ingot grows in a monocrystalline structure according to the seed. Careful control of the process is required so that the seed structure is kept.

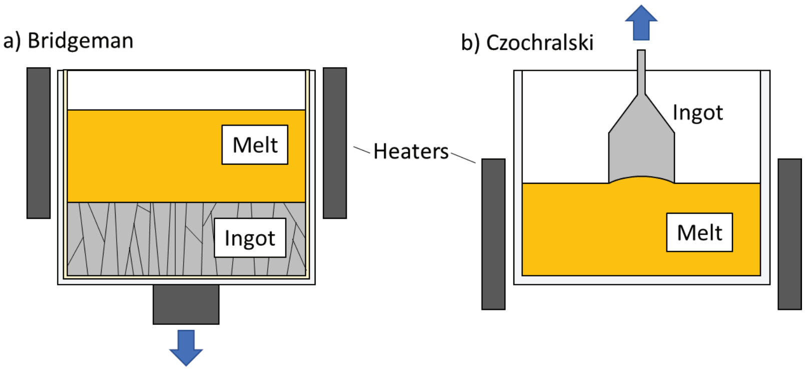

Figure 13. Principles of a) Bridgeman and b) Czochralski ingot growth techniques. The arrow indicates the pulling direction. After [89].

In both cases, and also for alternative crystallization techniques, the solidification process is one of the main sources of impurities. For multicrystalline material, which is the focus of this work, the majority of impurities comes from the crucible, the crucible coating, which is used to inhibit the contamination from the crucible, and from the furnace atmosphere.

The crucible is made of quartz, which is a suitable material to withstand the high melting temperature of silicon – 1414 °C [90]. Two main types of crucibles are used: fused quartz for Czochralski growth and slip cast for directional solidification. Fused quartz crucibles are made by fusing together purified quartz powder in a plasma arc inside a graphite mould. The outer layers of the crucible differ from the inner layers. For silicon crystallization the inner layer is usually manufactured from synthetic quartz. For slip cast crucibles large amounts of quartz sand are fused into a glass phase, cooled down, crushed into powder, which is then used along with water and a special binder to create a silica slurry called slip. Slip is then used to cast the crucible in a plaster mould, which extracts moisture. Finally the crucible is sintered. The main impurities found in quartz crucibles are Fe, Al, Na and Ca [91]. In fused quartz crucibles, these impurities are in the range of ppbw, while in slip cast they are in the range of ppmw. They are introduced into silicon by dissolving the crucible wall and by diffusion from the crucible to the melt, and in case of directional solidification also by diffusion from the crucible to solidified silicon. Oxygen from the dissolved crucible will also be incorporated into the ingot from the melt. The level of oxygen will differ between the growth techniques as well. In Czochralski growth the ingot covers a large part of the free liquid surface, thus oxygen evaporation will be reduced and its concentration in the melt will be increased during the process. In directional solidification oxygen evaporation from the melt is easier with a larger free liquid surface, and also the surface of contact between the crucible and the melt will be reduced more rapidly, leading to lower oxygen concentration in multicrystalline silicon than in CZ material. While for CZ oxygen interaction with point defects during cooling is the main reason for quality loss [92], metallic impurities are the main problem for directionally solidified mc-Si. Recently silicon nitride crucibles were investigated as possible replacement for quartz crucibles with an additional possibility of using the same crucible for several solidification processes [93].

As previously mentioned, a crucible coating is used in directional solidification to inhibit the diffusion of impurities into the melt and into the multicrystalline ingot. The coating is made of silicon nitride. It is deposited on the crucible by air spraying a slurry made of silicon nitride powder, water, an organic binder and a surfactant. Several layers of such slurry are deposited and dried between each deposition. After the final drying, the crucible is fired in air to burn off the organic binder and oxidize the silicon nitride powder, which is important for coating stability and to avoid wettability. Such coatings are the main source of nitrogen in multicrystalline silicon, but they can also contain metallic impurities. Silicon nitride coatings can contain up to ppm levels of metals such as Al, Cu, Fe, K, Na, Co and W [91, 94, 95]. With that said, the coating is still required to block the impurities from the crucible from diffusing to silicon. Except for their main function as impurity diffusion barrier, it was also shown that silicon nitride coatings are important for silicon nucleation during directional solidification [96].

Other furnace elements also contribute to the impurity level in the final ingot. Graphite heaters and hot zone elements are commonly used in silicon crystallization furnaces. The SiO present in the melt due to melting of the quartz crucible evaporates and reacts with the graphite elements, resulting in SiC and CO. Carbon can be then incorporated into the melt from the furnace atmosphere, subsequently being incorporated into the ingot [19].

The distribution of impurities in a silicon ingot depends highly on their concentration in the crucible, coating and furnace atmosphere, but for some elements there is a large difference between their solubility in the melt and in the ingot. This leads to their segregation during growth. This segregation depends on the ratio of impurity concentration in the melt and in the ingot:

$$k_{eq} = \frac{C_S}{C_L} \qquad (2.8)$$

where, k_{eq} is the equilibrium segregation coefficient, C_S is the impurity concentration in the solid and C_L is the impurity concentration in the liquid.

Depending on the value of the segregation coefficient, the impurity present in the melt before crystallization in concentration C_0 is distributed in the solid during the process according to the Scheil equation:

$$C_s = kC_0(1-f)^{k-1} \qquad (2.9)$$

where f is the solidified fraction at which the concentration in the solid is calculated. The Scheil equation results in a distribution depending on the segregation coefficient, as can be seen in Fig. 14 a). Segregation coefficients of selected impurities are presented in Table 2.

Table 2 Effective segregation coefficients k_{eff} of selected impurities [80].

Al	Cu	Fe	Mg	Ti	Mo	W	P	B	C
$3x10^{-2}$	$8x10^{-4}$	$6.4x10^{-6}$	$3.2x10^{-6}$	$2x10^{-6}$	$4.5x10^{-8}$	$1.7x10^{-8}$	0.35	0.8	0.05

Multicrystalline silicon is solidified by the directional solidification technique from the crucible bottom towards the top, with constant impurity diffusion from the crucible bottom and walls. The phenomena described above lead to a concentration of impurities towards the top of the ingot (due to segregation), and at the sides and bottom (due to in-diffusion from the crucible and coating). These areas are described as the "red zone". A typical red zone is visible in Fig. 14 b), which shows a lifetime map of a cross-section of a multicrystalline ingot. Since metallic impurities affect the lifetime, it is lower where their concentration is the highest. This happens to be close to the crucible bottom and walls due to diffusion, and near the top due to segregation. The lifetime is commonly represented with a colorscale on which the lowest values are red and this explains the origin of the term. The red zone can have a width of 2-3 cm [97], and it usually needs to be cut off from the ingot before it is processed further, resulting in yield losses.

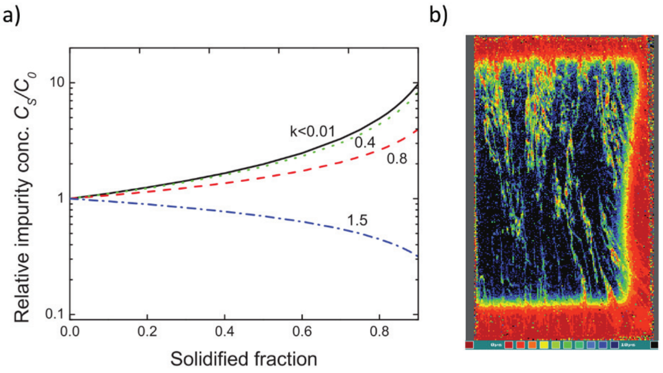

Figure 14. Distribution of impurities in the ingot. a) relative impurity concentration according to the Scheil equation and b) a lifetime map of half of a directionally solidified silicon ingot [81].

2.4.3 Impurity overview

The effect of impurities on silicon properties depends on their concentration, but also on their type and distribution. The three mentioned groups of impurities, that is dopants, light elements and metallic impurities can serve as a general categorization, but it can be useful to describe the effect of different elements.

Dopants

Boron is the primary dopant used in the semiconductor industry for p-type silicon. It is important to control its levels, as it is directly related to the resistivity of the obtained material. The target resistivity for solar cells is approximately 1 Ohm cm, which relates to about 300 ppba of boron. SEMI, an organization dedicated to standardizing the processes in the semiconductor industry, divides silicon feedstock into four classes of feedstock quality with respectively <1, <20, < 300 and <1000 ppba boron concentrations [98]. The last two classes are comparable to metallurgically refined silicon. Using such feedstock requires careful control of resistivity levels. Boron in itself is acting like a dopant, but in monocrystalline cells it is also usually related to the Light Induced Degradation (LID) effect [99]. One of the defects hypothesized to explain this effect is a boron-oxygen complex, which is created under illumination, but can be dissolved by annealing [100]. Boron, a negative ion in the lattice, is also attracted to iron ions, positive in p-type silicon. They form iron-boron pairs, immobile at room temperature. Such pairs introduce defect energy levels shallow in comparison to the levels introduced by interstitial iron. The pairs can be dissociated either by thermal or optical excitation. This allows measurements of interstitial iron concentration, based on measuring lifetime before and after iron-boron pair dissociation [101, 102].

In photovoltaics **phosphorus** is the standard dopant for creating the n-type emitter in boron-doped p-type wafers. The SEMI standard mentioned previously limits phosphorus in feedstock classes respectively by <1, <20, <50 and <720 ppba, which is more strict than for boron. Since phosphorus has a lower segregation coefficient than boron, using highly contaminated feedstock might result in a change of type from p-type to n-type towards the end of crystal growth. Using feedstock with a considerable concentration of boron and phosphorus leads to a requirement for compensation when doping the material. Work on compensation is also an important focus for photovoltaic silicon research [103].

Light elements

Oxygen comes mostly from the quartz crucible. Oxygen is a slow diffuser, thus contamination through the solidified part is negligible in directional solidification. The presence of oxygen in silicon strongly influences many properties of electronic and photovoltaic devices made from the silicon material, and because of this oxygen distribution in the ingot has long been an interesting field of study for many researchers. The segregation coefficient of oxygen in silicon is still debated, and values between 0.2 and 1.25 were reported [104]. While oxygen is not considered harmful in itself, oxides might be detrimental to cell quality. Oxide precipitates, preferentially nucleating on defects such as dislocations or, in the case of CZ material, in the vacancy-rich regions of the crystal, introduce defect states to the bandgap [105]. Such precipitates can also attract other impurities, which leads to increased recombination activity. It was shown using n-type material that the density of oxide precipitate defect states can be correlated with the precipitate interface area [106]. An important phenomenon related to oxygen in silicon are the oxygen complexes called thermal donors. Thermal donors grow during heat treatments, and they might influence the charge carrier concentration [20]. The so called "old thermal donors", are generated in temperatures between 400 and 500°C, and annihilated above 650°C. "New thermal donors" are generated in the range 600-900°C and annihilate above 1100°C.

For **carbon** it has been mentioned previously that the main sources are the furnace graphite parts, which react with silicon oxide coming from the crucible. Carbon is considered electrically inactive, but in too high concentrations silicon carbide precipitates are formed and they may cause problems both in wafering and solar cell operation. Wire from the wire saw can break on SiC and frequent wire changes reduce the process throughput [107]. SiC particles can also act as shunts through which the current is flowing in the cell, reducing the effectiveness of the p-n junction [108].

Nitrogen comes mostly from the crucible coating. It is electrically inactive, but its precipitates might act as shunts and nucleation sites for SiC. The role of silicon nitride coming from the coating in nucleating silicon crystals during directional solidification was already mentioned. In Czochralski crystals nitrogen is known to suppress vacancy and Si interstitial-type defects [109].

Metallic impurities

The amount of equipment parts made of metal and used in solar cell manufacturing is too large to name them all, and they can all be potential sources of metallic contamination. Most of them can be fortunately neglected because they have no direct contact with silicon.

When it comes to metallic impurities, **iron** is the most extensively studied contamination [59, 73, 75]. Its typical concentration in the multicrystalline material is between 10^{12} and 10^{15} at/cm^3. The majority of iron in silicon ingots comes from the coating and crucible and this is the element responsible for the red zone effect. In larger concentrations, it highly affects cell operation. It is highly recombination active, especially in its interstitial form, however only about 1% of the total iron concentration remains in the interstitial form in the ingot [110]. Large part of the subsequent sections about defect-impurity interactions is focused on iron. It is also hypothesized to be the main harmful element in the material described in papers forming the core of the thesis.

Lifetime is also very vulnerable to **titanium** presence, but fortunately the element is a slow diffuser and in-diffusion is unlikely. If its levels are low in the feedstock, crucible and coating, it should not affect the device significantly. It is still worth attention as a potentially severe lifetime killer, with concentration levels of 10^{12} at/cm^3 already affecting cell efficiency [111].

Nickel is part of corrosion resistant steel used for many parts of equipment for silicon processing and as such is very difficult to avoid. It is also a very fast diffuser [112], which makes some researchers consider it having an impact on the device similar to iron even though its concentration in the feedstock, crucible and coating is smaller. Nickel silicides will introduce deep levels into the band gap and act as recombination centers [46]. Nickel is also found co-precipitating with iron in nickel-iron silicides [113].

Aluminium can act as an acceptor, similarly to boron. It is usually used to make back contacts and to generate a back surface field (BSF), which introduces a potential difference on the backside of a solar cell. Such a field is used to reduce surface recombination [114]. It can be also used to form the p-type emitter on n-type silicon solar cells. Similarly to boron it can form complexes with oxygen [115]. The oxygen-aluminium complex introduces an energy state deep in the bandgap and as such can act as a recombination center.

Silver is also used for front contacts in silicon solar cells. It is a fast diffuser [116] and some cross-contamination is inevitable, but the contact firing process is the last high temperature treatment in solar cell processing and it relies on rapid heating to the peak temperature and a rapid cooldown, so the thermal budget is much smaller than that during solidification. Therefore, silver is not as harmful for silicon solar cells as iron.

Copper is an element that rapidly diffuses in silicon as a positively charged interstitial ion. While it is not considered as harmful as iron in multicrystalline silicon due to its lower concentration in the feedstock, crucible and coating materials, it can be a larger problem in CZ material [117]. Copper silicides, Cu_3Si, can cause severe minority-carrier recombination.

Copper can also co-precipitate with iron and nickel, forming strong recombination centers [113]. The element is most problematic in n-type silicon due to the fact that interstitial copper ions are positively charged. Its silicide is also positively charged when the Fermi level is below E_c – 0.2 eV. In n-type silicon the Fermi level can exceed this value for certain doping concentrations. The silicide then becomes neutral or negatively charged, enhancing copper precipitation [99]. In addition, copper is one of the elements responsible for LID, even in material without boron doping [99]. Due to its diffusivity, copper can also be used for delineating defects in monocrystalline silicon [118].

Chromium behaves in a similar manner to iron and discussion on iron can also be applied here [119]. It is a fast diffuser and can be potentially harmful in concentrations as low as 10^{10} at/cm^3 [120]. It is, however, less abundant in the solar cell manufacturing process than iron.

Sodium is present in the coating powder in ppm levels. This means it can diffuse into silicon, but it occupies substitutional sites and as such is a slow diffuser. It is assumed that sodium can also be introduced into the cell from the glass used for cell encapsulation [121]. In silicon solar cells it tends to decorate crystal defects such as stacking faults, and leads to the so-called Potential Induced Degradation (PID) mechanism [122].

Alkali metals are harmful in the semiconductor industry, because they have a strong impact on thermal oxides, but this is not that relevant for multicrystalline silicon solar cells.

Other elements such as magnesium, tungsten, cobalt or zinc can also be found in silicon. Transition metals can all be considered as harmful impurities and need to be controlled during solar cell processing. Especially the steps with a high thermal budget need to be carefully optimized, because in higher temperatures the transition metals have a higher diffusivity and with enough time, this creates a space for harmful defect-impurity interactions.

2.5 Defect-impurity interactions

The main interactions between defects and impurities are related to segregation and precipitation. The segregation mentioned here is different to that described in relation to crystallisation, where impurities are segregated by not being incorporated into the growing crystal and stay in the liquid near the solid-liquid interface. It rather refers to a phenomenon of impurity atoms diffusing towards surfaces of a solid material or to interfaces or defects in its structure. In general, segregation can be defined as an increase in concentration of one or more components near lattice discontinuities [123]. When this definition is limited to one-phase fields on a phase diagram, precipitation can be defined as a similar inhomogeneity, but involving phase separation. Indeed these two are linked – usually segregation leads to precipitation when the segregating element concentration locally exceeds the solubility limit in the material. Both these phenomena are of great importance in materials science and have been studied for a long time – one of the first accounts of how impurities affect iron properties in ways now understood as segregation-based is dated to 1894 [124]. In metallic materials it can affect brittleness, creep, intergranular corrosion, recrystallisation texture or grain boundary migration rates. Similarly the role of segregation and precipitation is also important in photovoltaic applications, and it is especially relevant for multicrystalline material due to its high defect densities.

The main driving force behind segregation is the reduction of the surface energy of the interface towards which the segregation is happening [125]. When the temperature for diffusion is sufficient, impurity elements will diffuse towards the interface or defect and the final ratio between their concentration near the interface and in the bulk of the material can reach several orders of magnitude. Cottrell atmospheres (mentioned before) are an example of segregation of impurities towards a stress field introduced by a dislocation.

After exceeding the solubility limit for a given temperature, precipitate nuclei begin to form. The dependence of solubility on temperature is complex. Solubility of a certain element depends also on the concentration of other elements, including dopants [126]. An example of calculated iron solubility in p-type silicon can be seen in Fig. 15.

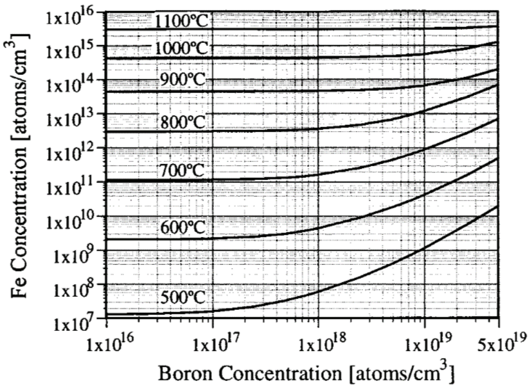

Figure 15. Calculated iron solubility in silicon as a function of boron doping level. Taken from [126].

Nucleation can occur by two main mechanisms: homogeneous and heterogenous. At a given temperature multiple nuclei are formed out of the impurity agglomerates present in a solution. The majority of them dissolves, because there is an energy barrier which needs to be overcome for a nuclei to grow further. This energy corresponds to creating a nucleus with a radius larger than a critical, stable value. The nuclei are created and dissolve in random concentration fluctuations. The majority of these fluctuations result in nuclei smaller than the critical size, but part of them have the necessary energy and develop into larger nuclei which can continue to grow. This can only happen when there is a certain undercooling, that is for a given impurity concentration the temperature is lower than the temperature in which this concentration can remain completely dissolved in the silicon matrix. The difference between these temperatures is the undercooling. Homogeneous nucleation occurs when the undercooling is sufficient for the nuclei to overcome the energy barrier in a defect-free lattice. The energy barrier is relatively lower when defects such as dislocations or grain boundaries are present, providing preferential nucleation sites. An analogous description of nucleation is usually presented when explaining crystal growth and nucleation from the melt, and homogeneous nucleation is then understood as nucleation in a pure melt. Heterogenous nucleation from the melt occurs on crucible walls or particles in the melt, because both lower the nucleation energy barrier.

It was stated that clean defects introduce only shallow levels into the band gap and as such they are not harmful for solar cell operation. It is the impurity segregation and precipitation at defects that leads to minority carrier recombination and a deterioration of material quality. Since segregation occurs when impurity diffusion is fast enough and precipitation depends on solubility, the main defect-impurity interactions affecting cell quality occur at elevated temperatures. There are three main process steps in solar cell production which utilize high temperature treatments. The first is crystallization of silicon ingots with subsequent slow cooling. After the ingot is solidified, blocks are cut out of it and wafers are cut from these blocks. The second high temperature step in the silicon production chain is the phosphorus diffusion, usually performed on p-type wafers to introduce phosphorus and create an n-type emitter. After depositing the anti-reflection coatings and screen-printing the contacts, the cell is then fired to remove the additives from the paste and solidify the contacts. This firing is the third high temperature treatment which can potentially affect the impurity distribution.

As explained previously, the majority of impurities is first introduced into the material during **crystallization**. One of the first interactions between defects and impurities is hypothesized to occur at the growth interface, where segregation is weaker in the vicinity of grain boundaries, acting as sinks for impurities from the melt due to their higher diffusion at the boundaries, and stronger in the intragrain areas of the growing ingot [64]. This could lead to a higher impurity content at grain boundaries just after the material is solidified. In the first hours of cooling down after crystallization the temperature in the ingot is still relatively high, allowing for further segregation, so the defects become decorated with impurities. A SIMS copper distribution of a silicon bicrystal containing a grain boundary can be seen in Figure 16 a). A clear increase in copper concentration on the grain boundary is visible.

Impurity segregation in the form of denuded zones near grain boundaries is visible in Figure 16 b). The map shows the internal quantum efficiency (IQE), a parameter describing the quality of the material for photovoltaic applications, with high resolution. IQE is highest in the zone between the grain boundaries and the middle of the grain. This is because the impurities provide the main minority carrier recombination sites and their distribution after segregating towards the boundaries is related to the IQE presented in the figure. Only impurity atoms from the close vicinity of grain boundaries manage to diffuse towards them during cooling of the ingot, and recombination is weaker in the areas denuded of impurities. Recombination is higher in the middle of the grain, where the impurity concentration is relatively unchanged, and highest at the grain boundaries which attracted the impurities from the denuded zone. Dislocations also attract impurities. Their effect in multicrystalline material can be stronger than that of grain boundaries. Figure 17 shows how dislocation density and lifetime can correlate in such material.

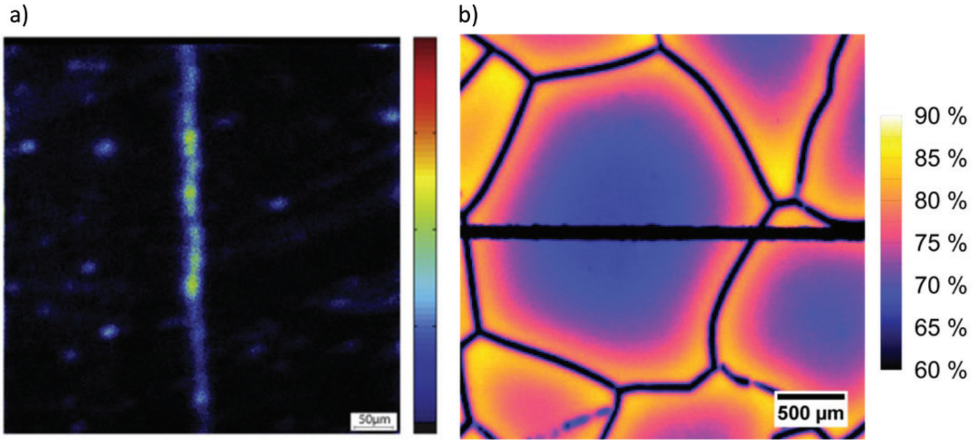

Figure 16. a) SIMS copper distribution mapping of a small-angle grain boundary cross-section in a bicrystal pulled with a speed of 3 µm/s. The spatial scale is 50 µm long, the color scale is in auxiliary units. Taken from [64]. b) High resolution LBIC map of red zone multicrystalline silicon after solidification. The black stripe in the middle of the image is a contact finger.

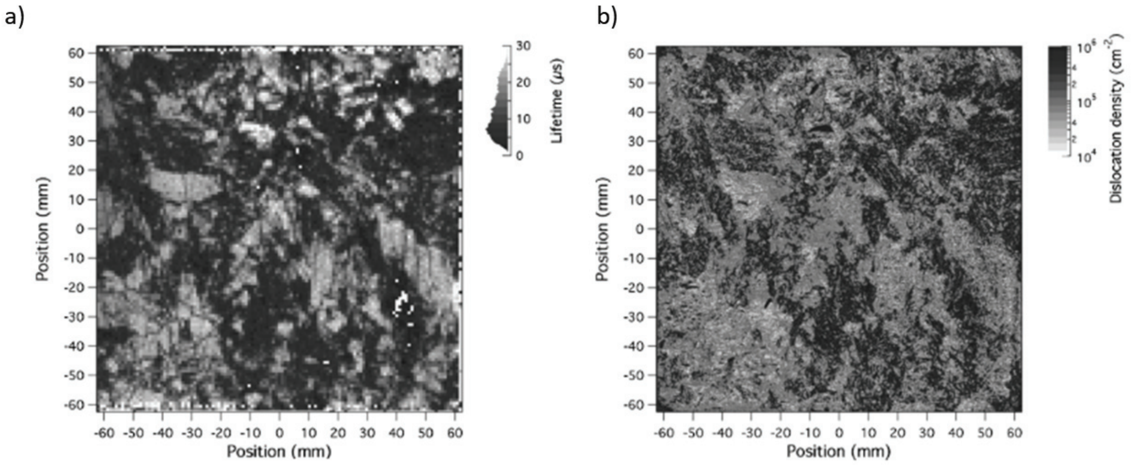

Figure 17. a) Lifetime and b) dislocation density maps of neighbouring 125 x 125 mm^2 wafers. Both taken from *[40]*.

It was shown that if the structure of the material is changed to contain more random-angle grain boundaries, the overall density of dislocations is reduced and higher cell efficiencies can be achieved [16]. To control the structure, a special seeding layer or careful control of the temperature gradients near the crucible bottom is needed. Material obtained this way is termed High Performance Multicrystalline silicon (HPMC-Si).

The next high temperature process in the production chain, phosphorus diffusion, can have a beneficial effect on impurity concentration and distribution. Phosphorus diffusion is usually done using a $POCl_3$ source for depositing a P_2O_5 layer on top of the wafer in a tube furnace. The layer reacts with silicon into SiO_2 and P, which then diffuses into the wafer and creates an n-type emitter layer. The furnace is heated up to about 800-900° C, which is required for the in-diffusion. The process usually lasts from 60 to 100 minutes, and such a thermal budget allows changes in the impurity distribution, particularly for fast-diffusing impurities (e.g. Fe, Ni and Cu). Impurities from the bulk of the wafer diffuse towards the phosphorus rich surface layer. This reduces the overall impurity concentration in the active part of the device. Processes which rely on diffusion of impurities towards noncritical regions of the wafer are called **gettering** [127]. The efficiency of gettering depends highly on the impurity type, because different impurities show different diffusivity in silicon. An overview of diffusivity of different impurities can be seen in Figure 18. It can be seen that copper will be gettered easier than iron, which is easier to getter than titanium or vanadium. The diffusivity directly affects the distances from which impurities can be gettered.

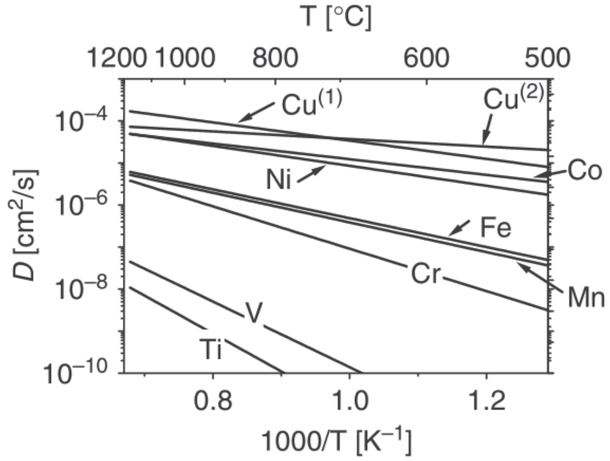

Figure 18. Diffusion coefficients as a function of temperature. Taken from [128].

Gettering accompanies phosphorus diffusion in the silicon solar cell process. In literature this particular process, important for silicon photovoltaics, is often abbreviated as PDG - Phosphorus Diffusion Gettering. It was shown that PDG can lead to a reduction of interstitial iron concentration by about two orders of magnitude [129]. The driving force behind gettering is not completely understood, but the difference in impurity solubility between the phosphorus rich layer and the bulk silicon has been suggested as one hypothesis. Some authors indicate a local decrease of dissolved impurity concentration and a concentration gradient due to easier precipitation of impurities in the phosphorus-rich emitter.

A distinction needs to be made, however, because during PDG impurities diffuse not only towards the emitter layer, but also towards defects. This can also be generalized for other gettering techniques, which can be divided into *external* and *internal* gettering. PDG is a case of external gettering in which the impurity sinks are at or near the surface. Part of the impurities diffuse to the external phosphorus glass layer, which is later removed from the wafer. However, during PDG some impurities diffuse also towards the defects present in the material. This is a case of internal gettering. The segregation and precipitation at defects during the cooling of the ingot can also be understood as internal gettering. It is also worth mentioning that another defect-impurity interaction can be found in the phosphorus diffusion process step. The phosphorus profiles after diffusion depend on the structure of the material, and the diffusion along grain boundaries and intragrain defects is faster than in defect-free material. A deeper penetration of phosphorus into the material have been found with SIMS near such defects when compared with defect-free areas [130].

Different gettering techniques are utilized in the photovoltaic and semiconductor industry, and there is a different understanding of internal and external gettering. In most microelectronic devices only a relatively shallow layer of silicon near the wafer surface are active in the device manufactured on the wafer. The remaining bulk is the noncritical part of the device. This means that except for gettering impurities to the backside surface, for example by artificially introducing defects to the backside by sandblasting it or by depositing a polysilicon layer on it, techniques which introduce defects into the bulk can also be used. In this case internal gettering refers to removing impurities from the active front surface layer into the bulk. An interesting variation of this technique results in a Magic Denuded Zone, as named by MEMC Electronic Materials [131, 132]. In this technique a vacancy concentration profile is introduced into the wafer through a thermal treatment, so that a lower concentration is found near the surface than in the bulk. This leads to a difference in oxygen precipitate density, larger in the middle due to a larger density of vacancies acting as oxygen precipitate nucleation sites and gettering this element. Metal impurities present in the active surface layer or introduced in subsequent process steps are then gettered on the oxygen precipitates in the bulk.

In photovoltaic applications, however, impurities in the bulk will lead to minority carrier recombination and a reduction of solar cell efficiency in consequence, thus only external gettering techniques are suitable and can be understood in the positive sense. Because of this, internal gettering in this field is understood as gettering on defects naturally occurring in the material. Internal gettering can be beneficial to minority carrier lifetime by reducing the concentration of the more harmful interstitial impurities and confining them in the vicinity of structural defects [133], but it is not always positive in photovoltaic applications. Impurities gettered on dislocations and grain boundaries in standard cell processing still act as recombination centers [41]. The general understanding is that even in the presence of defects in the multicrystalline material the minority carrier lifetime can be improved with PDG and that external gettering is stronger than internal gettering systems [21, 134]. Murphy et al. studied this in monocrystalline material by analyzing the effect of oxide precipitation and showed that in the presence of internally gettering oxide precipitates the phosphorus diffusion gettering process was still effective for improving material performance [135]. Different studies, however, showed that lifetime can be increased only slightly where it was high before gettering, and it can be even reduced in areas with high defect densities during annealing with an external gettering layer [21, 136].

Except for PDG, other variants of gettering are known in photovoltaics. Aluminium gettering can be used during fabrication of a p-type emitter layer on n-type wafers. It is also occuring during the fabrication of a p/p+ junction generating the Back Surface Field (BSF) in p-type solar cells [128]. Boron diffusion gettering can be used for n-type wafers, when boron is chosen as the dopant for emitter fabrication.

Since the gettering efficiency depends also on precipitation and impurity distribution, several models have been developed to evaluate precipitation in silicon, mainly with focus on iron as the main impurity diffusing from the crucible and coating [73, 75, 137]. The main models of precipitation are based on either the Ham's law or the Fokker-Plank equation. Both assume that the supersaturation of the precipitating element in its matrix is the precipitation driving force. This means that for precipitation to start the solute concentration needs to be larger than its solubility. Ham's law is based on the assumption that there is a given precipitate density which does not vary over time. The precipitates are modeled as spheres which grow or shrink during processing. It is simple and allows fast computation, but neglects the changes in precipitate density which may occur due to nucleation of new precipitates or dissolution of existing ones. Ostwald ripening, which is the dissolution of existing small precipitates enhancing the growth of larger ones is also neglected. These phenomena are accounted for in the Fokker-Plank equation. It is, however, more complex and computationally demanding. A review of these models with a focus on iron precipitation by Morishige et al. shows that the gettering process highly affects the iron concentration and the size and density of its precipitates [73]. Two different sets of process conditions are studied: i) high temperature gettering at 900°C with a starting iron concentration of 3.5×10^{13} at/cm^3, and ii) low temperature gettering at 815°C with a concentration of 2×10^{14} at/cm^3. In both cases the models show a decrease of interstitial iron in the material, even though the precipitates can be expected to dissolve and introduce iron to the matrix. In the Ham's law model it is shown as a decrease of precipitate size to near full dissolution in the high temperature case. In the Fokker-Plank equation it is shown as the decrease in precipitate density with simultaneous increase in their size. In the high temperature gettering process the Fokker-Plank equations predict a small increase in precipitate density in the end, but to a level lower than in the beginning. In the low temperature treatment, the removal of iron is slower than the precipitate dissolution, as the process is limited by diffusivity, but the out-diffusion lasts even after precipitate dissolution is stopped during cooldown, and in the end the interstitial iron concentration is lower. Del Canizo and Luque have shown how to calculate lifetime given the precipitate distribution [138], and Kwapil et al. refine such modelling by also considering the effect of band bending around the metallic precipitates, which results in a Schottky contact between the precipitate and the surrounding silicon [75].

What Morishige highlights in her overview of precipitate modelling is that the precipitate distribution depends highly on the distribution of defects in the material. Her models are run over four different structural defects distributions. Since defects act as nucleation sites, the results vary between the different scenarios, and a large difference can be seen especially between the scenario without defects present in the material and the ones in which either dislocations, a grain boundary, or both were included. Dislocations can have a different effect on material properties, however, depending on the structure of the dislocation and it's alignment in the crystal. This is also true for grain boundaries, which can have a different effect depending on their type. To provide more precise models this should be evaluated and taken into account.

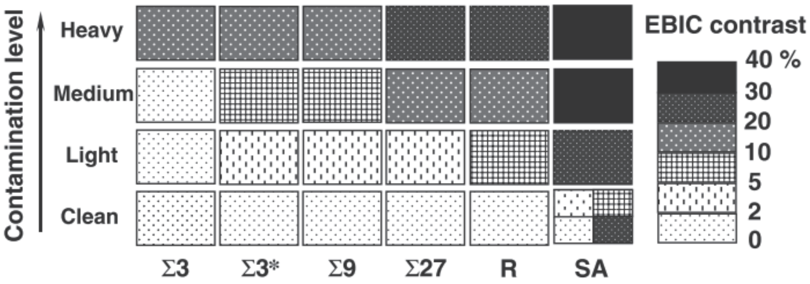

Figure 19. Classification of EBIC contrast of GBs at 300 K with respect to GB character and contamination level (Σ3 - Σ3 (111); Σ3* - Σ3 with other planes). Taken from [63].

For grain boundaries it was already mentioned how their structure can affect their electrical properties. In general, it is considered that Σ3 grain boundaries affect the solar cell the least, and the effect is stronger with a growing coincidence index. Random-angle grain boundaries provide more nucleation sites, and small-angle grain boundaries, understood as dense dislocation networks, have the strongest effect. This is summarized best with a chart by Chen and Sekiguchi, presented in Fig. 19. Since this electrical effect seems strongly correlated with precipitation, and consequently with the availability of nucleation sites and the potential to attract and segregate impurities, it can be also understood as depending on their internal gettering strength.

The strength of internal gettering of dislocations also depends on how they are arranged in the material. According to Donolato, the effect of dislocations on the diffusion length and on the lifetime of minority carriers in the material can be described with a parameter called *recombination strength* – Γ [23, 42]:

$$\Gamma = \frac{\gamma_d}{D} = \frac{N_r}{tl\Delta nD} \qquad (2.10)$$

where γ_d is the linear recombination velocity, defined as the number of recombinations N_r per time t, dislocation length l and excess carrier density Δn. D is the minority carrier diffusion coefficient.

The recombination strength is an important parameter used to describe the relation between the dislocation density ρ in a certain area and the minority carrier diffusion length L in this area. The direct relation is complex, and can be found in the original paper by Donolato [23]. The reason why this relation is mentioned in the context of gettering and defect-impurity interactions is that Rinio at al. showed that the spatial distribution of dislocations seems to have an effect on their recombination strength, and explained it with a relation between the time they are generated in the material and the different thermal budget available for impurities to segregate towards them and precipitate on them [42]. This can be understood easier when looking at Fig. 20. Fig. 20 a) shows how the Donolato theory relates dislocation density to electrical performance of the material, here as internal quantum efficiency (IQE), with the use of the recombination strength parameter. In Fig. 20 b) different dislocation clusters can be seen, and a higher recombination strength is found on unordered dislocation clusters looking like “explosions”, in contrast to a lower recombination strength calculated for ordered clusters, where dislocations tend to align on specific planes [42]. Castellanos et al. showed that in the clusters with a higher recombination strength the etch pits tend to be shaped like ellipses, and indicated a relation between the etch pit eccentricity range in a cluster and the recombination strength of this cluster [43]. These results show how the dislocation cluster structure can have an effect on their interaction with minority carriers, and this interaction is strongly connected with impurity segregation and internal gettering. The dislocations with round etch pits, showing a lower eccentricity range, are perpendicular to the sample surface and relatively ordered. The clusters with high etch pit eccentricity range most probably consist of dislocations tangled together, full of jogs and kinks, at different angles to the surface.

In the light of the discussion above this would mean that the unordered dislocations provide much more nucleation sites and a stronger stress field. This leads to stronger impurity segregation and a larger precipitate density in their vicinity. This was confirmed by Castellanos et al. with several synchrotron-based micro X-Ray Fluorescence measurements, which showed copper precipitation on the highly recombination active cluster E and no copper decoration on cluster A. The group hypothesizes that the differences in dislocation spatial distribution and structure can be explained by differences in the time of their generation.

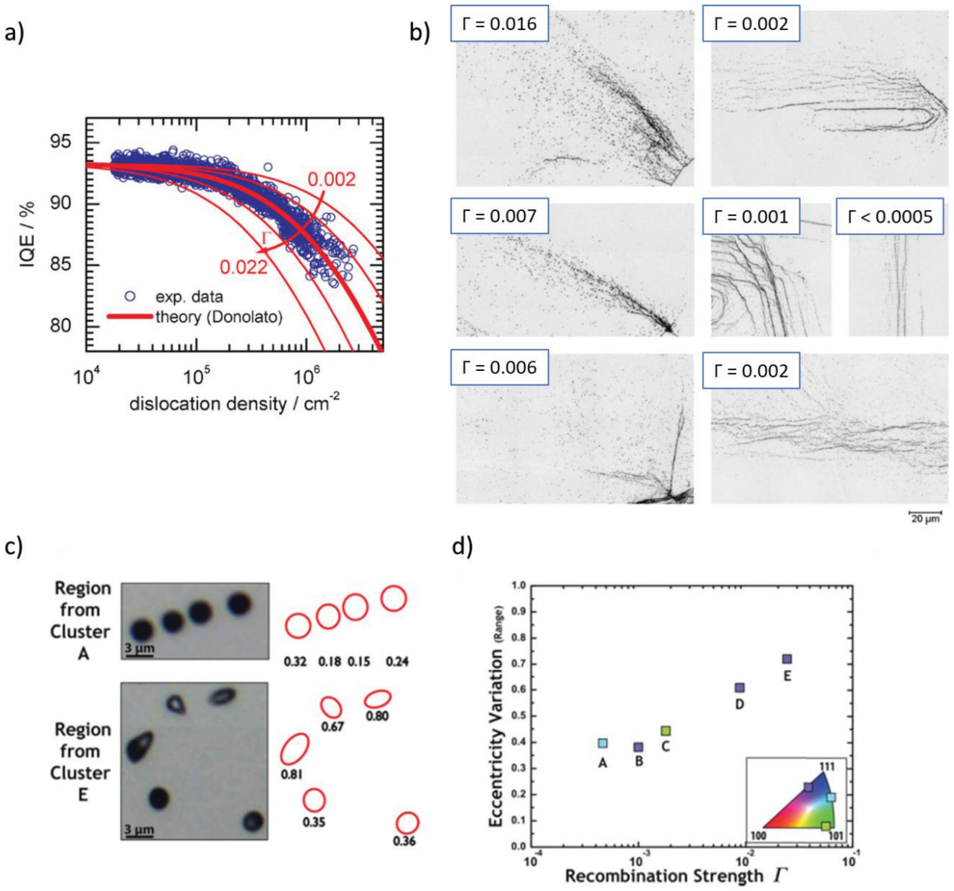

Figure 20. Recombination strength of dislocations based on Donolato's model and its relation with dislocation spatial distribution and structure. a) The relation between internal quantum efficiency (IQE) and dislocation density parametrized with recombination strength Γ, and b) micrographs of selectively etched silicon wafers showing the relation between recombination strength of different dislocation clusters and their spatial distribution, are taken from [42]. The micrographs in b) show selected dislocation clusters from the experimental data partially presented in chart a). Micrographs in c) show differences in eccentricity of dislocation etch pits in two extreme cases of dislocation clusters and the chart in d) shows the relation between dislocation etch pit eccentricity and their recombination strength. c) and d) are taken from [43].

The dislocations with low recombination strength were supposedly generated during crystal growth, even at the solid-liquid interface. This would give them enough time in the high temperature regime for polygonization, which leads to an ordered dislocation structure and decreases the driving forces for segregation and nucleation of precipitates on these clusters. The unordered dislocation clusters with high recombination strength are then supposed to originate later, during cooling of the ingot, and their structure is defined by glide due to thermal stress, which introduces the kinks and jogs serving as preferential nucleation sites for impurities. All this will have a major influence on the gettering process, decreasing the efficiency of external gettering especially in areas with unordered clusters with high recombination strength. Adding to this the dependence on different impurity types and their diffusivity, and the different defect and impurity distribution in the crystallized material makes the gettering process a difficult step, requiring a good understanding of the underlying physics and a lot of effort to optimize.

The final process, which has an effect on the impurities and defects in the bulk, is the contact firing in the presence of hydrogen-rich anti-reflection coating. After the emitter has been formed, the phosphorus glass is removed. The wafer is cleaned, textured and an anti-reflection coating is deposited on the frontside to reduce the optical losses due to reflection. Different anti-reflection coatings such as silicon oxide, aluminium oxide or amorphous silicon are used, but one of the more common coatings is the hydrogen-rich silicon nitride, Si_xN_y:H. The nitride is deposited by breaking down silane, SiH_4, and ammonia, NH_3, in the process of Plasma Enhanced Chemical Vapour Deposition (PECVD). Due to the amount of hydrogen involved in the reaction, the layer is a non-stoichiometric nitride with up to 40% of atomic hydrogen [139]. Recently also stacks of different layers are used to enhance the coating properties. On such layers the contact grid is printed, usually using a silver paste in a screen printing process. The paste contains cutting agents, which allows to cut through the anti-reflection coating and bond to the underlying silicon in a firing process. The firing process is a short annealing, commonly done in a belt furnace. The main aim of this process is the fabrication of contacts by removing the water and organic additives from the silver paste and allowing it to bond with silicon. Additionally part of the hydrogen from the anti-reflective coating diffuses into the bulk of the silicon wafer and passivates the structural defects. This phenomenon is referred to as **hydrogenation**. It is established that hydrogenation improves cell performance by passivating defect levels in the bandgap and shifting them either from deep levels into shallow levels or out of the bandgap completely [139, 140]. In p-type silicon hydrogen can passivate interstitial iron and chromium, as well as boron-oxygen complexes [141]. Typical firing profiles usually depend on a rapid heating from room temperature up to about 800°C and relatively slower cooling. The full thermal processing lasts up to a minute, and only during few seconds of the temperature peak the material is above 600°C. This is enough for hydrogen to diffuse into the bulk and either bond with impurity atoms or saturate the dangling bonds in the defect structure to reduce their strength as recombination centers [142]. Due to this effect the diffusivity of hydrogen in silicon is also an important field of study [143]. Sopori et al. have shown that the hydrogenation process is enhanced by an increased vacancy concentration, meaning that a vacancy-hydrogen complex is probably involved in hydrogen transport [142]. Similarly as for gettering, new models need to be developed due to the rising importance of new, low temperature hydrogenation techniques [141, 143]. The exact mechanism of hydrogenation is still debated. It was also hypothesized that the presence of hydrogen in silicon increases the diffusivity of metal impurities, making them easier to getter [144]. Another study indicates that the silicon nitride layer on the wafer surface also acts as an additional gettering layer [145]. On the other hand the review by Morishige et al. indicates that the firing process influences precipitate distribution by dissolving part of the precipitates and also leads to an out-diffusion of iron from the emitter layer back to the bulk [73]. A presence of a silicon nitride layer and an introduction of hydrogen into the lattice might change the behavior of the excess interstitial iron. The average effect of hydrogenation is more or less understood, even if the exact hydrogenation mechanisms are still discussed. Studying the local effect on different types of defects can give additional information on the interactions occurring in this process, just as it is with gettering. Karzel et al. have studied such an effect on grain boundaries, and they have shown that different types of grain boundaries respond differently to hydrogenation [67]. Their study was based on strong statistics. It analysed both the effect of phosphorus gettering and hydrogenation, and the local effects were studied on CSL and random-angle grain boundaries. The conclusions from analyzing gettering in standard multicrystalline material were similar to the ones presented above, for example to the electron beam induced current study of grain boundaries by Chen et al. They also show that the improvement after hydrogenation is stronger when an externally gettering layer is present, which would confirm that the short temperature peak of contact firing adds a gettering effect. Karzel's results concerning hydrogenation were also in line with the discussion on different types of grain boundaries presented here: the increasing coincidence index was correlated with a poorer response to hydrogenation, that is with a smaller improvement in lifetime at the grain boundary after the process. This would mean that a higher impurity concentration on a grain boundary leads to a decreased hydrogenation effect. Thus, higher impurity concentrations inhibit the hydrogen passivation of dangling bonds. This conclusion led the authors to suggest that a higher density of Σ3 grain boundaries would be beneficial to solar cell performance, which is contradictory to the improvement obtained by using HPMC-Si material with large densities of random-angle grain boundaries and lower dislocation densitites. Castellanos et al. showed that the HPMC-Si material gives larger improvements in lifetime after phosphorus gettering than standard multicrystalline material [146]. The work presented in this thesis aims to analyse this subject in more detail. The main focus is placed on defects and impurities in HPMC-Si, on how they interact during gettering and hydrogenation, and how these interactions affect cell performance.

3. Experimental techniques

3.1 Solidification and wafer processing

The samples studied in this work were prepared by means of directional solidification. Samples presented in article I and II, and reference material presented in articles III and IV were prepared from ingots grown in state-of-the-art facilities in Singapore, owned and operated by the REC Group. Material studied in articles III and IV was grown at NTNU, in a pilot scale Crystalox DS250 furnace. This furnace has capabilities to produce 12-15 kg silicon ingots with diameters of 250 mm and height of about 100 mm. It is a directional solidification furnace, which can be operated in two modes, the Vertical Gradient Freeze (VGF) and as a Bridgman type furnace. The former was used in this work. In VGF the temperature gradient necessary for solidification is obtained with multiple heaters or a variable heat leak. The crucibles used in the process were spray-coated with α-Si_3N_4 from a powder dispersion and heated before filling with feedstock in order to remove the binding and dispersing agents and dry the coating. The ingot was seeded partially with monocrystalline seeds, and partially with FBR feedstock, and the remaining feedstock was high purity. A quartz rod was used during the process to probe the solid-liquid interface to ensure that the seed melted only partially.

After solidification, the ingots were cut into blocks, ground and sent to REC for wafering and thermal processing, i.e. gettering and hydrogenation. Part of the processing on selected wafers was performed at IFE in Kjeller, Norway. 156 x 156 mm^2 wafers after thermal processing performed according to the respective experiment design presented in the included articles were laser-cut into smaller pieces and prepared for the selected characterization techniques. The sample preparation procedure will be presented in the subsequent sections along with the techniques used to characterize the sample.

3.2 Characterization techniques

3.2.1 Microwave detection of photoconductive decay - μPCD

The lifetime of carriers in a semiconductor can be measured by microwave detection of photoconductive decay - μPCD [55, 92]. This contactless technique relies on the fact that microwave reflection in the material depends on conductivity, which in turn changes with the number of free carriers. μPCD measurements are performed by illuminating the sample with a laser pulse while simultaneously using a microwave antenna to emit a signal towards it. The conductivity of the sample decays into the equilibrium state after the laser pulse because of carrier recombination, and the antenna detects the change in microwave reflection due to this decay. The photoconductivity transient curve is then used to calculate the lifetime. The microwaves are of about 10 GHz frequency and the laser pulse lasts a few hundred nanoseconds with an intensity of about 10^{13} photons/s. The technique is non-steady-state, which comes from the fact that it is calculating the lifetime from a transient and the sample is not analysed in equilibrium, with a steady illumination. The laser pulses last only few µs. This non-steady-state aspect of the measurement leads to a limitation of precise interpretation of low lifetime values.

Usually the sample is scanned with the laser and lifetime maps can be obtained with resolution depending on the laser spot size. Due to the weak signal, the lifetime is usually measured in high injection, which is different from the standard, natural one sun illumination. One of the disadvantages of the technique is that the measured lifetime is attributed to the illuminated spot, but the recombination is occurring also outside of this spot because of lateral diffusion of carriers. It is, however, routinely used in industrial applications because it is relatively fast and well known.

The technique, just like photoluminescence and quasi-steady-state photoconductance techniques, measures the effective lifetime in the sample. This parameter is a good indication of the quality of the material, and is given by:

$$\frac{1}{\tau_{eff}} = \frac{1}{\tau_{bulk}} + \frac{1}{\tau_{surface}} = \left(\frac{1}{\tau_{radiative}} + \frac{1}{\tau_{Auger}} + \frac{1}{\tau_{SRH}}\right) + \frac{1}{\tau_{surface}} \qquad (3.1)$$

The equation means that both bulk and surface recombination limit the effective lifetime of the sample. To extract the bulk lifetime value, the surface recombination needs to be minimized and this is obtained by surface passivation. Sample preparation for bulk lifetime measurements is then focused on passivating the surface. In this work the samples were passivated by PECVD deposition of thin layers of hydrogenated amorphous silicon, approximately 40 nm on both wafer surfaces. The layer was deposited with an Oxford Plasmalab 133 system, with the deposition at 230 °C. The resulting layers show surface recombination velocities of about 5 cm/s. The µPCD measurements were performed on a WT-2000PVN instrument from Semilab. The wavelength of the illumination source was about 905 nm with a pulse width of 200 ns and an average power output of 8.5 mW. A spatial step size of 250 µm was used for the measurements.

3.2.2 Photoluminescence - PL

Another technique used to analyse carrier recombination and lifetime utilized in this work is photoluminescence imaging – PL [92, 147]. Here the sample is excited with a laser beam of about 800 nm and the resulting band-to-band emission from the material, a broad spectrum between 1000 and 1100 nm, can be detected with a CCD camera. The rate of spontaneous emission depends on electron and hole densities and on carrier lifetimes. Similarly to µPCD, the technique is contactless and allows for relatively fast in-line measurements, usually done in the form of spatial mapping of wafer lifetime. It is, however, difficult to calibrate and often the results are given in terms of auxiliary units. In this work quasi-steady-state photoconductance (QSSPC) was used to calibrate PL images [148]. QSSPC depends on the photoconductive decay like µPCD, but the transient is obtained in a quasi-steady-state by illuminating the sample with a flash lamp instead of a laser [149]. The time constant of the lamp is measured along with the photoconductive transient and this allows more precise measurements of small lifetimes, where carrier lifetime is lower than the lifetime of the flash, as well as larger lifetimes. The drawback is that the combination of using a flash lamp and microwave reflection measurements makes it impossible to obtain spatial information. The area from which signal is measured is limited to only few cm^2. Proper interpretation of QSSPC results requires also knowledge of sample optical properties and carrier trapping at low injection levels.

Similarly to µPCD, the samples for QSSPC calibrated PL require surface passivation. Again, 40 nm layers of hydrogenated, amorphous silicon were used for this purpose.

A LIS-R1 measurement system from BT Imaging was used for PL measurements presented in this work. It used a high power laser diode with 808 nm wavelength. Up to 75 W illumination with 1 sun intensity could be achieved with this system. Spatial resolution up to 160 µm could be obtained.

3.2.3 Light Beam Induced Current - LBIC

The µPCD and PL setups used in this work offered limited spatial resolution, and to obtain more detailed maps of electrical properties of the samples Light Beam Induced Current (LBIC) measurement was used. This technique uses a laser beam to excite charge carriers in a sample with a p-n junction and the current induced by the beam is measured [42]. Scanning the sample with the laser beam allows to measure the lateral distribution of the photocurrent. The principle of the LBIC measurement is presented in Fig. 21. Different detectors are used to measure the light power of the laser - P_L, reflection – R, and the short circuit current of the cell - I_{sc}. Basing on these parameters, the internal quantum efficiency, IQE is calculated:

$$IQE = \frac{1}{1-R} \cdot \frac{I_{sc}/e}{P_L/(hc/\lambda)} \qquad (3.2)$$

where, e is the electron charge, h is the Planck constant, c is the speed of light in vacuum, and λ is the laser wavelength.

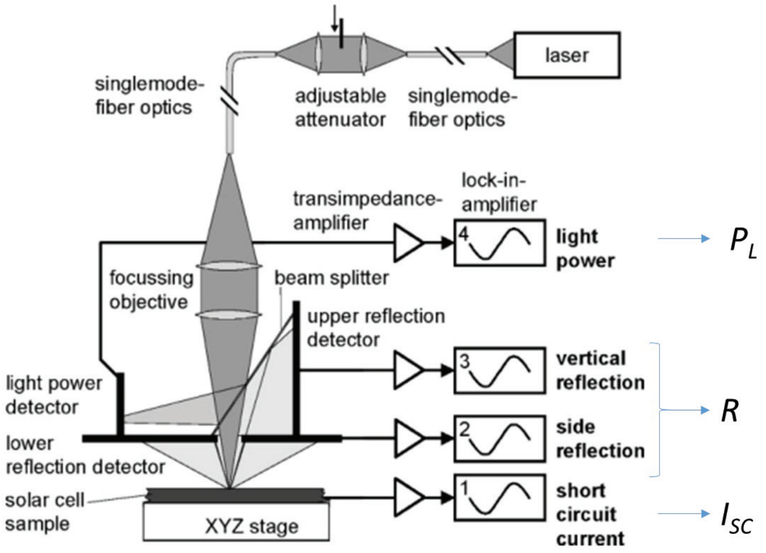
laser
singlemode-fiber optics
adjustable attenuator
singlemode-fiber optics
lock-in-amplifier
transimpedance-amplifier
4
light power
P_L
focussing objective
beam splitter
upper reflection detector
3
vertical reflection
light power detector
2
side reflection
R
lower reflection detector
solar cell sample
XYZ stage
1
short circuit current
I_{SC}

Figure 21. Light Beam Induced Current measurement system. Taken from [42].

IQE is a ratio of the number of collectable carriers obtained after illuminating the cell with a given light source to the number of photons of a given energy that shine on the solar cells from this source and are absorbed by the material. It is a good measure of the quality of the material, giving detailed information on recombination. The sample can be scanned with the laser beam, just as in the previously discussed lifetime measurement techniques, but here the optical system allows a much higher resolution, even down to 6 μm on the homemade system in the Department of Engineering and Physics at the Karlstad University in Sweden, which was used in this work. The laser used in this equipment had a wavelength of about 826 nm with a 2 μW light power.

This measurement technique requires a p-n junction in the sample and contacts through which the short circuit current can be collected, and to this end the wafers after selected thermal treatments were processed into solar cells. The effect of thermal history of the wafers on their properties was the focus of the study, thus low temperature processing into Heterojunction with Intrinsic Thin layer solar cells (HIT) was chosen [150]. The processing was done in temperatures below 200 °C, and consisted of PECVD of amorphous intrinsic silicon, n- or p-type doped amorphous silicon, and indium oxides doped with tungsten as a transparent conductive film. The a-Si layers were approximately 10 nm thick, the tungsten-doped indium oxide layer had about 80 nm on the front and 70 nm on the backside. Silver contacts were printed using the same mesh on both sides of the cell to limit their effect on the LBIC signal in the spatial IQE maps.

3.2.4 Electron Backscatter Diffraction - EBSD

Part of the microstructural analysis was performed with Electron Backscatter Diffraction (EBSD). It can be performed with a Scanning Electron Microscope (SEM) equipped with an EBSD detector. The SEM provides the functionality of scanning the sample surface with an electron beam. Typical energies of the electrons in the beam range from few to about 40 keV. In the case of the technique used in this work, the electrons had 20 keV. The beam interacts with the sample, and several different signals can be measured from this interaction, giving different information about the sample topography and composition. In the case of EBSD, the information comes from a thin layer near the surface, approximately 20 nm deep, from which backscattered electrons can leave the material [151]. Only the electrons diffracting at specific crystal planes are treated as signal, and to increase its strength a large enough volume is required. The sample is tilted and angles from 60° to 80° are recommended. The diffracting electrons are detected by a phosphorus screen and the signal is registered in CCD camera. The registered patterns, called Kikuchi patterns, are characteristic for the crystal orientation of the sample. Scanning the sample surface with the beam allows indexing the grain structure at larger areas. The formation of a Kikuchi pattern can be seen in Fig. 22.

In this work EBSD was used for orientation imaging microscopy (OIM), from which grain boundary information was extracted. To increase the indexed area, a combo-scan feature was used, that is the sample was automatically moved in a raster-like pattern, and each position in this raster was then scanned by the electron beam. 40 mm x 30 mm areas were scanned in this manner. The equipment used for this was a JEOL JSM840 SEM with a Nordif EBSD detector.

In order to obtain the best EBSD signal, the sample needs to have as little topography as possible, because each topographical feature might absorb the electrons diffracted from beneath the surface. Therefore, the sample wafers needed to be ground and polished. All the samples analyzed in this work were about 50 mm x 50 mm wafers with a thickness of about 170 – 180 µm, in most cases after thermal treatment or several cleaning and etching steps. In the case of HIT solar cells made on such wafers, the cell structure was first removed by etching for 2 h in aqua regia, that is HCl : HNO_3 in a molar ratio of 3 : 1, heated to 80 °C. The grinding and polishing were done in the following order:

- Gluing the sample on a steel holder
- Grinding with SiC paper, 1200 grit, 1 minute
- Polishing with 9 µm diamond suspension, 10 minutes
- Polishing with 3 µm diamond suspension, 10 minutes
- Polishing with 1 µm diamond suspension, 5 minutes
- Degluing with a stream of hot water

Special care was required in order not to break the wafers during this procedure.

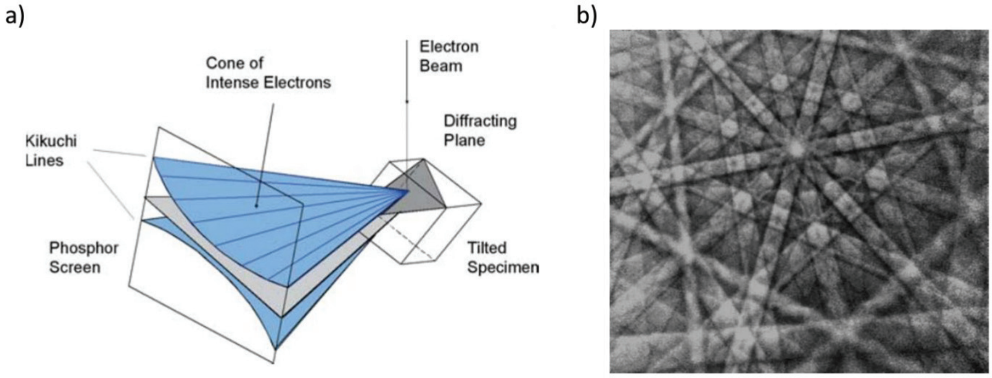

Figure 22. a) Formation of a Kikuchi band in EBSD, b) a Kikuchi pattern of cadmium, obtained with a 20 keV electon beam. The pattern consist of multiple bands coming from different crystal planes. Both images taken from [151].

3.2.5 Selective etching

Additional microstructural information was obtained by selective etching of the polished samples and microscope analysis. Selective etching is a standard technique used in the semiconductor and photovoltaic industry to delineate crystal defects in silicon, and several different etching recipes were developed over the years [152-154]. HF and HNO_3 are the basic components of silicon etchants, because the etching reaction of silicon proceeds in a two step cycle: silicon is oxidized by HNO_3, and the silicon oxide layer is dissolved with HF [155]. The basic principle is that the etching rate is different, usually larger, on dislocations, grain boundaries and other defects, and smaller on perfect crystalline lattice. In the case of Secco or Sopori etchants, this rate is also independent of crystal orientation of the grain. When a polished sample is etched, the resulting topography highlights the defects in the material, and after this procedure quantification of the defects is possible with a light microscope.

The standard procedure for multicrystalline silicon defect delineation at NTNU was to use a Sopori etching step with a 25 s duration. The Sopori etchant composed of HF (48%) : CH_3COOH (100%) : HNO_3 (69%) in a volume ratio of 36 : 15 : 2. The full etching procedure was as follows:

- RCA1 cleaning/10 min
- Dip in deionized water
- 5% HF/3 min
- Sopori/25 s
- HF:HNO_3(1:9)/5 s
- Dip in deionized water
- Flush with ethanol

The RCA1 cleaning mixture used in step 1 was developed in the Radio Corporation of America as the first step in a procedure for cleaning of silicon wafers [156]. This step was aimed at cleaning organic residues and particles off of the wafer. The RCA1 mixture consists of 5 parts of deionized water, 1 part of ammonia water (29% HNO_3) and 1 part of aqueous H_2O_2 (30%). The mixture needs to be heated to 80 °C and used with agitation. For the remaining steps the solutions were applied at room temperature and without agitation, only with delicate mixing by slowly moving the sample holders in the bath.

This procedure was optimized for quick dislocation and grain boundary analysis, but the resulting etch pits were relatively large, and for high dislocation densities above 10^6 per cm^2, they overlapped and made the analysis unprecise.

In article II the Secco etch was used with a 60 s etching step, as this etchant provided a slower etching rate and allowed better control of the etch pit size, so small etch pits without overlap could be obtained. The Secco etch used in this work was a mixture of one part of 0.15

molar solution of $K_2Cr_2O_7$ in H_2O and two parts of 49% HF. In the Secco etch, the $K_2Cr_2O_7$ acts as an oxidizing agent.

Article V deals with the optimization of Sopori etching for different dislocation densities. The etch pit size after different Sopori etching time is also compared with Secco to evaluate the possibility of replacing the Secco etchant, which contains the highly harmful potassium chromate in addition to HF.

3.2.6 PVScan and microscope analysis

Dislocation densities were measured on etched samples with two techniques. The first one was done in a PVScan 6000 instrument by scanning the surface with a laser and analyzing the reflected light after collecting it in an integrating sphere [157]. The laser beam was scattered more when the scanned area had a high etch pit density and this led to a stronger signal collected in the integrating sphere. This technique allowed for fast analysis of an etched sample and gave an overview of the distribution of dislocations in the material, but the measured densities were not precise. This affected especially areas with densities above 10^6 etch pits per cm^2 due to etch pit overlap, and with densities below 10^4 etch pits per cm^2 due to too weak scattering of the laser beam. Grain boundaries also etch faster and are visible after selective etching. The laser beam is scattered on grain boundaries and this affects the precision of PVScan measurements. A typical map of multicrystalline material measured with PVScan can be seen in Fig. 23.

PVScan was used in this work in comparison with μPCD measurements, and the results are presented in Article I.

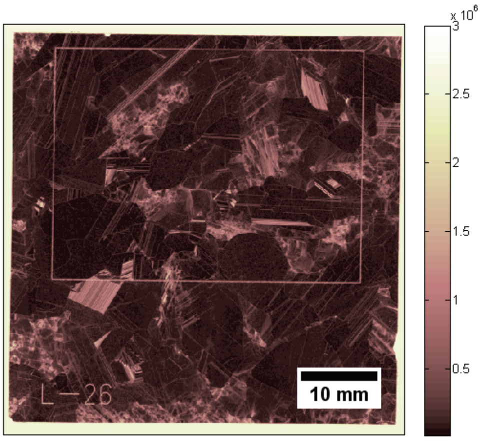

Figure 23. PVScan of a laser marked 50 mm x 50 mm sample after etching 25 s with the Sopori etchant. Scan step size: 100 μm, scan speed: 20 mm/s. The color scale is scaled in etch pits per cm^2.

To obtain more precise information about dislocation densities in the areas previously scanned with LBIC, light microscope imaging was coupled with image analysis software. Microscope images were taken in the regions of interest selected from LBIC maps. Their position on the sample was described in terms of the LBIC coordinate system. The images were manually cleaned in the GNU Image Manipulation Program - GIMP, thus no contamination, scratches or grain boundaries were visible with high contrast, and analysed with an ImageJ script which thresholded them and counted etch pits [158]. The position of each etch pit was saved in the LBIC coordinate system and etch pit maps with coordinates corresponding to the LBIC maps were created basing on this information. These LBIC-dislocation density map pairs allowed an analysis of the dislocation recombination strength in Article II. The relatively large images analysed for this article were composed of an array of images taken with an automated light microscope Olympus MX61A. A comparison of the precision of PVScan and ImageJ analysis of microscope images is presented in Article V.

3.2.7 Secondary Ion Mass Spectrometry – SIMS

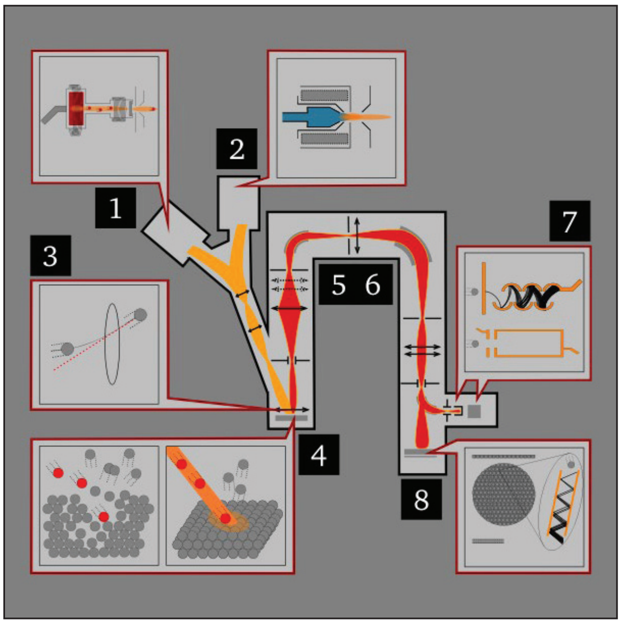

Figure 24. Scheme of SIMS instrument. Description of numbered parts in main text marked with numbers in parentheses. Image in public domain.

Several dislocation clusters with high recombination strength and neighbouring areas with low dislocation densities were analysed for the presence of metallic impurities with Secondary Ion Mass Spectrometry – SIMS. Secondary Ion Mass Spectrometry is a technique of composition analysis. It is especially suitable for studying impurities in semiconductors and thin films and it detects elements at level of $10^{16} – 10^{14}$ atoms/cm^3. This means that SIMS allows analysis of impurities on ppb level. The core principle of SIMS is sputtering of sample surface and analysis of secondary ions with a mass spectrometer. A simple scheme of one type of SIMS equipment can be seen in Fig. 24. The magnetic sector type of SIMS equipment presented in Fig. 1 usually has two primary ion sources – Cs for analysis of electronegative elements (1) and O for analysis of electropositive elements (2). Primary ions are focused on the sample with a system of electromagnetic lenses (3) and usually hit the sample surface with energies in range of 0.5 – 30 keV (4). Ions sputtered out of the surface have much smaller energies – 5 to 15 eV. They are accelerated by appropriate voltage and guided through a system of an electrostatic sector analyser (5) and a magnetic sector analyser (6). The system selects ions based on their mass to charge ratio. The selected ions are then projected to an electron multiplier (7 top), a Faraday cup if the intensity is too high for other detectors (7 bottom) or a CCD camera (8). Such a system gives high mass resolution, low detection limits and high transmission. Other systems are also available, with time of flight systems allowing simultaneous analysis of different elements and measurements of large molecules.

The analysis in this work was performed on a Cameca IMS 7F measurement system at the University of Oslo (UiO, Norway). It allowed studying the impurity content in circular areas with a diameter of about 60 µm. The results of SIMS depth profiling are presented in Article III.

3.2.8 Neutron Activation Analysis - NAA

The scope of the SIMS analysis done in this work and presented in Article III, that is the list of elements which were analysed with SIMS, was limited by the results coming from an earlier Neutron Activation Analysis (NAA) study of the ingot material. This technique consists of two distinguishable steps. The sample is first irradiated with neutrons in a nuclear reactor, so that the different element atoms capture neutrons, and their radioactive isotopes are created. The irradiation can last up to several days and the received dose of neutrons determines the detection limits of the technique. The irradiated samples are then withdrawn from the reactor and the decay of the radioactive isotopes is analysed with γ-ray spectroscopy. Since each isotope has characteristic wavelengths of radiation emitted during decay, the composition of the sample can be analysed with sub-ppm precision [159]. Although the precision of this technique is very good, it can only measure bulk values. The samples analysed in this work were cubic pieces of silicon with a side length of about 20 mm. NAA cannot provide depth profiling or precise mapping like SIMS.

The NAA measurements presented in this work were performed by the staff of the Missouri University Research Reactor in USA.

3.2.9 Micro X-ray fluorescence - μXRF

The composition of several areas in the vicinity of the grain boundaries analysed in Article III was measured with Micro X-ray fluorescence (μXRF). X-ray fluorescence is also based on the characteristic emissions of elements, but here the emission is generated by first irradiating the sample with X-rays or γ-rays. This excites the atoms in the sample, and when they relax, they emit secondary X-rays. This characteristic secondary spectrum is then analysed, allowing for chemical composition determination [160]. The “micro-” prefix in the name of the technique comes from the fact that the analysis is performed with a highly focused X-ray beam, allowing a spot size of about 200 nm [161]. μXRF can be used to obtain composition maps of small areas of the sample, similar to SIMS, but with better spatial resolution.

The μXRF perfomed in this work was carried out at the Advanced Photon Source of the Argonne National Laboratory in USA. The equipment used allowed the detection of metallic precipitates above about 10 nm in diameter.

3.3 Modelling

Combining the LBIC and light microscope analysis allowed to model the recombination strength of dislocations in Article II. The calculations were based on the Donolato theory of charge carrier recombination at dislocations [23], mentioned in the introduction. The steps necessary to perform the recombination strength fitting are presented in Fig. 25.

The LBIC measurements were first to be performed on the samples with HIT cell structure, which was removed with etching afterwards. The samples were selectively etched and microscope images of their surface were taken. First the etch pit – IQE map pairs were prepared as described in 1.2.6. Topograms of the etch pit density were then calculated as in [42], so that their resolution was the same as that of the IQE maps. This allowed to compare the map pairs pixel by pixel, resulting in a relation between the dislocation density and IQE. The selected pixels were then used for fitting the Donolato curves. Since the Donolato model relates the dislocation density with diffusion length, PC1D [162] was used for modelling the IQE for a given set of diffusion lengths in the cell structure used in this experiment. The HIT cells were modelled assuming a shallow emitter with about 2.9x10^{20} cm^{-3} peak doping on an Erfc profile and a front surface recombination velocity of 1000 cm/s. Since the laser used in the LBIC measurements had a wavelength of about 826 nm, which is close to the infrared spectrum and is absorbed in the rear of the cell, the rear surface recombination was fitted to the highest IQE values measured in the cells. The highest IQE values in each sample were measured in areas with the smallest defect density, thus as close to perfect material as possible, and hence the rear surface recombination was used as the parameter limiting the cell. The recombination strength of dislocations in the analysed cluster was extracted from the fitted curve.

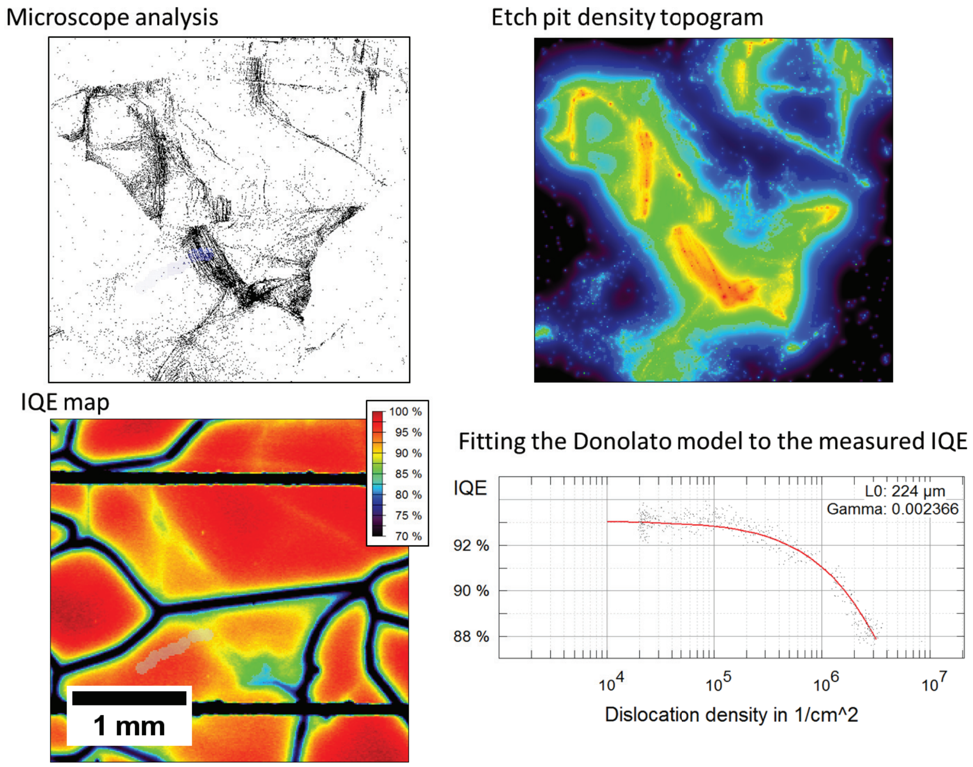

Figure 25. Modelling of the recombination strength of dislocations. The light blue marks visible on the IQE maps and etch pit maps from the microscope analysis show which pixels were selected from the IQE maps and etch pit density topograms for the Donolato curve fitting.

4. Summary of the publications within the four main topics investigated in this PhD thesis

4.1 Effect of grain boundaries on lifetime

The thesis work started with an analysis of the effect of grain boundaries on minority carrier lifetime in industrially grown HPMC-Si during solar cell processing. The results were presented in *Article I*. The µPCD mapping technique was used to measure the lifetime in samples after different processing. Four groups of samples were studied: i) without any thermal processing (ungettered), ii) after gettering, iii) after gettering and hydrogenation, and finally iv) without the gettering step, but after hydrogenation (ungettered and hydrogenated). The gettering was done by a standard phosphorus diffusion gettering process. The hydrogenation was an effect of first depositing a SiN_x layer rich with hydrogen, and then firing with a temperature profile as used for standard contact firing. The processing was done in state-of-the-art facilities of REC Singapore. All samples were etched to remove the surface layers and to have comparable surface properties, and had their surface passivated for lifetime measurements. The results showed that both gettering and hydrogenation are necessary for lifetime improvement from the ungettered state. Both these steps gave a 15% improvement in the mean lifetime of samples from the middle of the ingot, which is the most important part for commercial solar cells. In the case of performing only hydrogenation, or only gettering, the mean lifetime deteriorated from the ungettered state. This was especially visible for hydrogenation. Grain boundaries and the intra-grain areas were studied separately. It was shown that the gettering process considerably increases the lifetime in the intra-grain areas, but also the recombination activity is increased at grain boundaries. Subsequent hydrogenation passivated the grain boundaries and led to an improvement, which was also confirmed by recombination velocity modelling of grain boundaries. This parameter was increased by gettering, and then reduced through hydrogenation to levels comparable with grain boundaries in the unprocessed sample.

The main challenge with this study was that the µPCD technique used for measuring the lifetime maps had poor resolution and did not allow for detailed analysis of the defects. Some grain boundaries could be barely distinguished on lifetime maps of the samples even when carefully compared with their EBSD maps. Dislocation clusters were also found on the samples after selective etching, but due to the µPCD resolution their effect on the lifetime was also hard to assess.

Article II was a continuation of the previous work, where more precise high resolution photoluminescence imaging was used. The study focused on the effect of the gettering process on recombination in HPMC silicon and it was shown that the recombination due to interstitial iron atoms was reduced after PDG in the middle part of the ingot, but a different recombination mechanism was activated or enhanced. The change in impurity distribution, that is the dissolution of metal impurities with lower diffusivity or precipitation within the grains were hypothesized as possible causes.

4.2 Recombination strength of dislocations

Further analysis of extended defects in HPMC Si was performed with LBIC with much finer resolution, and this allowed a deeper insight in both the effect of dislocations and grain boundaries on the electrical properties of the material after different processing. The samples were processed in a similar way as in the previous study, but the analysis of the ungettered and hydrogenated group was dropped because this treatment clearly deteriorated the material quality. Article III focused on dislocations. They were analyzed using the Donolato theory of recombination. The results confirmed the trend observed in previous work that the recombination activity at the defects is increased during gettering and then reduced by hydrogenation. These results were quantified as recombination strength – Γ. In the middle of the ingot the dislocations in the ungettered samples showed values at the level of 10^{-3}, gettering increased them by an order of magnitude in most cases, and hydrogenation reduced them back to 10^{-3}. In the top, where a larger concentration of impurities segregates, the effect of gettering was stronger, increasing the gamma values up to 10^{-1}. SIMS showed that the concentration of nickel on the dislocation clusters is increased after gettering. In the case of one of the analyzed clusters a change in precipitate distribution was found after gettering. The effect of segregation towards defects and changes in precipitate distribution are hypothesized to be the main factors behind the changes of the electrical properties during gettering. The work also confirms the strong effect of hydrogen passivation.

4.3 Recombination activity of grain boundaries

High-resolution LBIC measurements allowed also a more detailed analysis of grain boundaries, and the results are presented in Article IV. The grain boundaries, just like discussed above, increased their recombination activity during gettering. However, 90% of random-angle grain boundaries, described as detrimental to cell operation, were very well passivated by hydrogenation. Only a small fraction of these GBs remained recombination active in the fully processed cell. To answer the question what remains recombination active, a statistic of the grain boundary types was calculated, and the results showed that it is the small-angle grain boundaries that had the largest effect on IQE. This type of GBs consists of dislocation networks, and along with the observations from Article II it shows that even with utilizing the HPMC growth techniques and minimizing their density in the material, dislocations remain the defect having the largest effect on solar cells. A fraction of segments of CSL grain boundaries also remained recombination active. Σ27 GBs showed the highest activity in this group. Some segments of Σ3 GBs also showed recombination activity. Two cases of Σ3 GBs, one active, and one inactive after full processing were analyzed with µXRF. The analysis was done on ungettered and gettered samples. The results showed that the inactive GB was decorated with impurities in the ungettered state, but gettering removed most of the impurities from its vicinity. The case of the active GB was different: it was clean in the ungettered state, but after gettering, probably due to internal gettering processes, became decorated with impurities and recombination active. These results were in line with the results presented in Article III, showing that a change in precipitate distribution due to internal and external gettering affects the electrical properties of the material.

4.4 Selective etching and dislocation density measurements

The work presented in Article I and Article III led to the conclusion that a better understanding of the defect delineation procedures is required for more precise dislocation density analysis. The standard procedures used at NTNU utilized the Sopori etchant, with the main etching step lasting about 25 s. This results in relatively large etch pits, above 2 µm in diameter, which overlap in the large dislocation density areas and leads to an unprecise measurement of dislocation density in such areas when using the PVScan, a technique based on analyzing scattered laser light. More precise measurements can be obtained with light microscopy and computer image analysis, yet still the highest precision is achievable with the Secco etchant used so that the etch pits are small, below 1µm in diameter. The issue with the Secco etchant is that it contains the toxic hexavalent chromium compounds in addition to the standard silicon etching chemicals such as hydrofluoric acid. The aim of the study presented in Article IV was to compare different conditions of Sopori etching and whether it is possible to optimize it for both improving the precision of the fast PVScan technique and achieve results similar to the Secco etching for precise light microscopy analysis.

References

[1] United Nations, Paris Agreement, 2015.
[2] M.Z. Jacobson, M.A. Delucchi, Z.A.F. Bauer, S.C. Goodman, W.E. Chapman, M.A. Cameron, C. Bozonnat, L. Chobadi, H.A. Clonts, P. Enevoldsen, J.R. Erwin, S.N. Fobi, O.K. Goldstrom, E.M. Hennessy, J. Liu, J. Lo, C.B. Meyer, S.B. Morris, K.R. Moy, P.L. O'Neill, I. Petkov, S. Redfern, R. Schucker, M.A. Sontag, J. Wang, E. Weiner, A.S. Yachanin, 100% Clean and Renewable Wind, Water, and Sunlight All-Sector Energy Roadmaps for 139 Countries of the World, Joule 1(1) (2017) 108-121.
[3] REN21, Renewables 2018 Global Status Report, Paris, 2018.
[4] REN21, Renewables 2017 Global Status Report, Paris, 2017.
[5] J. Cook, N. Oreskes, P.T. Doran, W.R.L. Anderegg, B. Verheggen, E.W. Maibach, J.S. Carlton, S. Lewandowsky, A.G. Skuce, S.A. Green, D. Nuccitelli, P. Jacobs, M. Richardson, B. Winkler, R. Painting, K. Rice, Consensus on consensus: a synthesis of consensus estimates on human-caused global warming, Environmental Research Letters 11(4) (2016) 048002.
[6] R. Gledhill, D. Hamza-Goodacre, L.P. Low, Business-not-as-usual: Tackling the impact of climate change on supply chain risk, PwC Resilience: A journal of strategy and risk (2013).
[7] Shell, A better life with a healthy planet - Pathways to net-zero emissions; A New Lens Scenarios Supplement, 2016.
[8] Statoil, Energy Perspectives - Long-term macro and market outlook, 2017.
[9] Fraunhofer Institute for Solar Energy Systems, Photovoltaics Report, (2018).
[10] M.A. Green, Y. Hishikawa, E.D. Dunlop, D.H. Levi, J. Hohl-Ebinger, A.W.Y. Ho-Baillie, Solar cell efficiency tables (version 52), Progress in Photovoltaics: Research and Applications 26(7) (2018) 427-436.
[11] Solar PV Wafer Weekly Spot Price. http://pvinsights.com/, 2018 (accessed 2018-10-10.).
[12] International Renewable Energy Agency, The Power to Change: Solar and Wind Cost Reduction Potential To 2025, 2016.
[13] C.W. Lan, W.C. Lan, T.F. Lee, A. Yu, Y.M. Yang, W.C. Hsu, B. Hsu, A. Yang, Grain control in directional solidification of photovoltaic silicon, Journal of Crystal Growth 360 (2012) 68-75.
[14] L. Arnberg, M. Di Sabatino, E. Øvrelid, Solidification of Silicon for Solar Cells, Transactions of the Indian Institute of Metals 65(6) (2012) 509-513.
[15] D. Hull, D.J. Bacon, Introduction to Dislocations, Elsevier Ltd.2011.
[16] C.W. Lan, A. Lan, C.F. Yang, H.P. Hsu, M. Yang, A. Yu, B. Hsu, W.C. Hsu, A. Yang, The emergence of high-performance multi-crystalline silicon in photovoltaics, Journal of Crystal Growth 468 (2016) 17-23.
[17] D.B. Holt, B.G. Yacobi, Extended defects in semiconductors - Electronic properties, device effects and structures, Cambridge University Press, New York, 2007.
[18] R. Kvande, L. Arnberg, C. Martin, Influence of crucible and coating quality on the properties of multicrystalline silicon for solar cells, Journal of Crystal Growth 311 (2009) 765-768.
[19] C. Schmid, M. Schumann, F. Haas, S. Riepe, Influence of argon flow rate on melt convection and incorporation of SiC in multicrystalline silicon, 28th European PV Solar Energy Conference and Exhibition, Paris, France, 2013.
[20] M. Di Sabatino, S. Binetti, J. Libal, M. Acciarri, H. Nordmark, E.J. Øvrelid, Oxygen distribution on a multicrystalline silicon ingot grown from upgraded metallurgical silicon, Solar Energy Materials and Solar Cells 95(2) (2011) 529-533.
[21] A. Bentzen, A. Holt, Overview of phosphorus diffusion and gettering in multicrystalline silicon, Materials Science and Engineering: B 159-160 (2009) 228-234.
[22] J.F. Lelievre, E. Fourmond, A. Kaminski, O. Palais, D. Ballutaud, M. Lemiti, Study of the composition of hydrogenated silicon nitride SiN(x):H for efficient surface and bulk passivation of silicon, Solar Energy Materials and Solar Cells 93(8) (2009) 1281-1289.

[23] C. Donolato, Modeling the effect of dislocations on the minority carrier diffusion length of a semiconductor, J. Appl. Phys. 84(5) (1998) 2656-2664.
[24] photoelectric effect, in: J. Law, R. Rennie (Eds.) A Dictionary of Physics, Oxford University Press, Oxford, UK, 2016.
[25] semiconductor, in: J. Law, R. Rennie (Eds.) A Dictionary of Physics, Oxford University Press, Oxford, UK, 2016.
[26] J. Nelson, The Physics of Solar Cells, Imperial College Press, London, UK, 2003.
[27] A. Richter, M. Hermle, S.W. Glunz, Reassessment of the Limiting Efficiency for Crystalline Silicon Solar Cells, IEEE Journal of Photovoltaics 3(4) (2013) 1184-1191.
[28] K. Yoshikawa, H. Kawasaki, W. Yoshida, T. Irie, K. Konishi, K. Nakano, T. Uto, D. Adachi, M. Kanematsu, H. Uzu, K. Yamamoto, Silicon heterojunction solar cell with interdigitated back contacts for a photoconversion efficiency over 26%, Nature Energy 2(5) (2017).
[29] M.A. Green, Solar cells - operating principles, technology and system applications, University of New South Wales, Kensington, New South Wales, Australia, 1998.
[30] F. Shimura, Semiconductor Silicon Crystal Technology, Academic Press, San Diego, California, 1988.
[31] D. Hull, D.J. Bacon, Strength of Crystalline Solids, Introduction to dislocations, Elsevier Ltd., Oxford, Great Britain, 2011, pp. 205-249.
[32] D. Hull, D.J. Bacon, Defects in Crystals, Introduction to dislocations, Elsevier Ltd., Oxford, Great Britain, 2011, pp. 1-20.
[33] D. Hull, D.J. Bacon, Movement of Dislocations, Introduction to dislocations, Elsevier Ltd., Oxford, Great Britain, 2011, pp. 43-62.
[34] P.B. Hirsch, S.G. Roberts, J. Samuels, P.D. Warren, The Brittle-To-Ductile Transition in Silicon, in: A.C.F. Cocks, A.R.S. Ponter (Eds.), Mechanics of Creep Brittle Materials 1, Springer, Dordrecht, 1989.
[35] D. Hull, D.J. Bacon, Origin and Multiplication of Dislocations, Introduction to dislocations, Elsevier Ltd., Oxford, Great Britain, 2011, pp. 157-169.
[36] D. Hull, D.J. Bacon, Dislocation Arrays and Crystal Boundaries, Introduction to dislocations, Elsevier Ltd., Oxford, Great Britain, 2011, pp. 171-204.
[37] E.J. Mittemeijer, Recovery, Recrystallization and Grain Growth, Fundamentals of Materials Science, Springer, Berlin, Germany, 2010, pp. 463-496.
[38] J.R. Bigger, D.A. McInnes, A.P. Sutton, M.C. Payne, I.I. Stich, R.D. King-Smith, D.M. Bird, L.J. Clarke, Atomic and electronic structures of the 90 degrees partial dislocation in silicon, Phys Rev Lett 69(15) (1992) 2224-2227.
[39] D.B. Holt, B.G. Yacobi, The electrical, optical and device effects of dislocations and grain boundaries, Extended defects in semiconductors - electronic properties, device effects and structures, Cambridge University Press2007.
[40] A. Bentzen, A. Holt, R. Kopecek, G. Stokkan, J.S. Christensen, B.G. Svensson, Gettering of transition metal impurities during phosphorus emitter diffusion in multicrystalline silicon solar cell processing, Journal of Applied Physics 99(9) (2006) 093509.
[41] M. Knörlein, A. Autruffe, R. Søndenå, M. Di Sabatino, Internal Gettering of Iron at Extended Defects, Energy Procedia 55 (2014) 539-544.
[42] M. Rinio, A. Yodyungyong, S. Keipert-Colberg, D. Borchert, A. Montesdeoca-Santana, Recombination in ingot cast silicon solar cells, Phys. Status Solidi A 208(4) (2011) 760-768.
[43] S. Castellanos, M. Kivambe, J. Hofstetter, M. Rinio, B. Lai, T. Buonassisi, Variation of dislocation etch-pit geometry: An indicator of bulk microstructure and recombination activity in multicrystalline silicon, Journal of Applied Physics 115(18) (2014).
[44] P.R. Wilshaw, An SEM EBIC Study of the Electronic Properties of Dislocations in Silicon, PhD thesis, Department of Metallurgy and Science of Materials, Oxford University, Oxford, England, 1984.
[45] V. Kveder, M. Kittler, W. Schröter, Recombination activity of contaminated dislocations in silicon: A model describing electron-beam-induced current contrast behavior, Physical Review B 63(11) (2001).

[46] M. Seibt, R. Khalil, V. Kveder, W. Schröter, Electronic states at dislocations and metal silicide precipitates in crystalline silicon and their role in solar cell materials, Applied Physics A 96(1) (2008) 235-253.
[47] A.H. Cottrell, B.A. Bilby, Dislocation Theory of Yielding and Strain Ageing of Iron, Proceedings of the Physical Society. Section A 62(1) (1949) 49-62.
[48] B. Shen, J. Jabłoński, T. Sekiguchi, K. Sumino, Influences of Cu and Fe impurities on oxygen precipitation in Czochralski-grown silicon, Japanase Journal of Applied Physics 35 (1996) 4187-4194.
[49] W.M. Bullis, Silicon Material Properties, in: W.C. O'Mara, R.B. Herring, L.P. Hunt (Eds.), Handbook of Semiconductor Silicon Technology, Noyes Publications, Park Ridge, New Jersey, USA, 1990, pp. 347-450.
[50] M. Morita, T. Ohmi, E. Hasegawa, M. Kawakami, M. Ohwada, Growth of native oxide on a silicon surface, Journal of Applied Physics 68(3) (1990) 1272-1281.
[51] J. Zhao, A. Wang, M.A. Green, 24% efficient PERL structure silicon solar cells, Twenty First IEEE Photovoltaic Specialists Conference, IEEE, Kissimmee, FL, USA, 1990.
[52] E.J. Mittemeijer, The Crystal Imperfection; Lattice Defects, (2010) 201-244.
[53] L. Priester, Grain Boundaries - From Theory to Engineering, Springer 2013.
[54] T. Kieliba, Zone-Melting Recrystallization for Crystalline Silicon Thin-Film Solar Cells, PhD thesis, Department of Physics, University of Konstanz, 2006.
[55] G. Stokkan, Characterisation of Multicrystalline Silicon Solar Cells, PhD thesis, Department of Materials Technology, NTNU, Trondheim, 2004.
[56] M. Dechamps, F. Baribier, A. Marrouche, Grain-boundaries: criteria of specialness and deviation from CSL misorientation, Acta Metallurgica 35(1) (1986) 101-107.
[57] D.G. Brandon, The structure of high-angle grain boundaries, Acta Metallurgica 14(11) (1966) 1479-1484.
[58] G. Palumbo, K.T. Aust, E.M. Lehockey, U. Erb, P. Lin, On a more restrictive geometric criterion for "special" CSL grain boundaries, Scripta Mater 38(11) (1998) 1685-1690.
[59] A. Autruffe, M. M'Hamdi, F. Schindler, F.D. Heinz, K.E. Ekstrøm, M.C. Schubert, M. Di Sabatino, G. Stokkan, High performance multicrystalline silicon: Grain structure and iron precipitation, Journal of Applied Physics 122(13) (2017) 135103.
[60] G. Palumbo, K.T. Aust, Structure-dependence of intergranular corrosion in high purity nickel, Acta metallurgica et Materialia 38(11) (1990) 2343-2352.
[61] K. Yang, G.H. Schwuttke, T.F. Ciszek, Structural and electrical charaterization of crystallographic defects in silicon ribbons, Journal of Crystal Growth 50(1) (1980) 301-310.
[62] A. Bary, G. Nouet, Electrical activity of the first- and second-order twins and grain boundaries in silicon, Journal of Applied Physics 63(2) (1988) 435-438.
[63] J. Chen, T. Sekiguchi, Carrier Recombination Activity and Structural Properties of Small-Angle Grain Boundaries in Multicrystalline Silicon, Japanese Journal of Applied Physics 46(10A) (2007) 6489-6497.
[64] A. Autruffe, L. Vines, L. Arnberg, M. Di Sabatino, Impact of growth rate on impurities segregation at grain boundaries in silicon during Bridgman growth, Journal of Crystal Growth 372(2013) (2013) 180-188.
[65] P. Käshammer, T. Sinno, A mechanistic study of impurity segregation at silicon grain boundaries, Journal of Applied Physics 118(9) (2015) 095301.
[66] J. Chen, T. Sekiguchi, D. Yang, F. Yin, K. Kido, S. Tsurekawa, Electron-beam-induced current study of grain boundaries in multicrystalline silicon, J. Appl. Phys. 96 (2004).
[67] P. Karzel, M. Ackermann, L. Gröner, C. Reimann, M. Zschorsch, S. Meyer, F. Kiessling, S. Riepe, G. Hahn, Dependence of phosphorus gettering and hydrogen passivation efficacy on grain boundary type in multicrystalline silicon, Journal of Applied Physics 114(24) (2013) 244902.
[68] T. Buonassisi, A.A. Istratov, M.D. Pickett, M.A. Marcus, T.F. Ciszek, E.R. Weber, Metal precipitation at grain boundaries in silicon: Dependence on grain boundary character and dislocation decoration, Applied Physics Letters 89(4) (2006) 042102.

[69] Z.-J. Wang, S. Tsurekawa, K. Ikeda, T. Sekiguchi, T. Watanabe, Relationship between Electrical Activity and Grain Boundary Structural Configuration in Polycrystalline Silicon, Interface Science 7 (1999) 197-205.
[70] F. Komninou, T. Karakostas, G. Bleris, N. Economou, Grain boundaries analysis in polycrystalline silicon by TEM, Journal de Physique Colloques 43(C1) (1982) 9-14.
[71] A. Autruffe, V.S. Hagen, L. Arnberg, M. Di Sabatino, Dislocation generation at near-coincidence site lattice grain boundaries during silicon directional solidification, Journal of Crystal Growth 411 (2015) 12-15.
[72] H. Hieslmair, A.A. Istratov, S.A. McHugo, C. Flink, E.R. Weber, Analysis of Iron Precipitation in Silicon as a Basis for Gettering Simulations, Journal of the Electrochemical Society 145(12) (1998) 4259-4264.
[73] A.E. Morishige, H.S. Laine, J. Schön, A. Haarahiltunen, J. Hofstetter, C. del Cañizo, M.C. Schubert, H. Savin, T. Buonassisi, Building intuition of iron evolution during solar cell processing through analysis of different process models, Applied Physics A 120(4) (2015) 1357-1373.
[74] T. Buonassisi, A.A. Istratov, M.A. Marcus, B. Lai, Z. Cai, S.M. Heald, E.R. Weber, Engineering metal-impurity nanodefects for low-cost solar cells, Nat Mater 4(9) (2005) 676-9.
[75] W. Kwapil, J. Schön, F. Schindler, W. Warta, M.C. Schubert, Impact of Iron Precipitates on Carrier Lifetime in As-Grown and Phosporus-Gettered Multicrystalline Silicon Wafers in Model and Experiment, IEEE Journal of Photovoltaics 4(3) (2014) 791-798.
[76] W. Kwapil, J. Schön, W. Warta, M.C. Schubert, Precipitate-related Injection-dependent Carrier Lifetime in n- and p-type Silicon, Energy Procedia 77 (2015) 106-112.
[77] A. Lanterne, G. Gaspar, Y. Hu, E. Øvrelid, M. Di Sabatino, Characterization of the loss of the dislocation-free growth during Czochralski silicon pulling, Journal of Crystal Growth 458 (2017) 120-128.
[78] G. Coletti, D. Macdonald, D. Yang, Role of Impurities in Solar Silicon, in: S. Pizzini (Ed.), Advanced Silicon Materials for Photovoltaic Applications, John Wiley & Sons, Ltd 2012.
[79] G. Stokkan, M. Di Sabatino, R. Søndenå, M. Juel, A. Autruffe, K. Adamczyk, H.V. Skarstad, K.E. Ekstrøm, M.S. Wiig, C.C. You, H. Haug, M. M'Hamdi, Impurity control in high performance multicrystalline silicon, physica status solidi (a) 214(7) (2017) 1700319.
[80] J.R. Davis, A. Rohatgi, R.H. Hopkins, P.D. Blais, P. Rai-Choudhury, J.R. McCormick, H.C. Mollenkopf, Impurities in silicon solar cells, IEEE Transactions on Electron Devices 27(4) (1980) 677-687.
[81] G. Coletti, Impurities in silicon and their impact on solar cell performance, PhD thesis, Utrecht University, 2011, p. 115.
[82] A. Schei, J.K. Tuset, H. Tveit, Production of High Silicon Alloys, Tapir Forlag, Trondheim, 1998.
[83] P. Woditsch, W. Koch, Solar grade silicon feedstock supply for PV industry, Solar Energy Materials and Solar Cells 2 (2002) 11-26.
[84] J.O. Odden, G. Halvorsen, H. Rong, R. Gløckner, Comparison of the energy consumption in different production processes for solar grade silicon, Silicon for the Chemical and Solar Industry, Oslo, Norway, 2008.
[85] REC Silicon ASA, Silane-Based Fluidized Bed Reactor (FBR) Technology Development, 2016.
[86] ITRPV, VDMA, International Technology Roadmap for Photovoltaic, ITRPV, VDMA Photovoltaik Equipment, Frankfurt, Germany, 2017.
[87] P. Zheng, F.E. Rougieux, C. Samundsett, X. Yang, Y. Wan, J. Degoulange, R. Einhaus, P. Rivat, D. Macdonald, Upgraded metallurgical-grade silicon solar cells with efficiency above 20%, Applied Physics Letters 108(12) (2016) 122103.
[88] J. Safarian, G. Tranell, M. Tangstad, Processes for Upgrading Metallurgical Grade Silicon to Solar Grade Silicon, Energy Procedia 20 (2012) 88-97.
[89] K.E. Ekstrøm, Structure Control of Multicrystalline Silicon, PhD thesis, Department of Materials Science and Engineering, Norwegian University of Science and Technology, Trondheim, Norway, 2016.

[90] Hanbook of Semiconductor Silicon Technology, Noyes Publications, Park Ridge, New Jersey, USA, 1990.
[91] W. Kwapil, A.S. Zuschlag, I.E. Reis, I. Schwirtlich, S. Meyer, R. Zierer, R. Krain, F. Kiessling, M. Schumann, C. Schmid, S. Riepe, Influence of crucible and coating on the contamination of directionally solidified silicon: first results of the German Research Network "SolarWins", 27th European Photovoltaic Solar Energy Conference and Exhibition, EUPVSEC Proceedings Website, Frankfurt, Germany, 2012.
[92] G.M.M. Gaspar, N-type Czochralski silicon solidification, PhD thesis, Department of Materials Science and Engineering, NTNU, Trondheim, Norway, 2016.
[93] V. Schneider, C. Reimann, J. Friedrich, G. Müller, Nitride bonded silicon nitride as a reusable crucible material for directional solidification of silicon, Crystal Research and Technology 51(1) (2016) 74-86.
[94] E. Olsen, E.J. Øvrelid, Silicon nitride coating and crucible—effects of using upgraded materials in the casting of multicrystalline silicon ingots, Progress in Photovoltaics: Research and Applications 16(2) (2008) 93-100.
[95] T. Buonassisi, A.A. Istratov, M.D. Pickett, J.P. Rakotoniaina, O. Breitenstein, M.A. Marcus, S.M. Heald, E.R. Weber, Transition metals in photovoltaic-grade ingot-cast multicrystalline silicon: Assessing the role of impurities in silicon nitride crucible lining material, Journal of Crystal Growth 287(2) (2006) 402-407.
[96] K.E. Ekstrøm, E. Undheim, G. Stokkan, L. Arnberg, M. di Sabatino, Beta-Si_3N_4 particles as nucleation sites in multicrystalline silicon, Acta Materialia 109 (2016) 267-274.
[97] T.U. Naerland, L. Arnberg, A. Holt, Origin of the low carrier lifetime edge zone in multicrystalline PV silicon, Progress in Photovoltaics: Research and Applications 17(5) (2009) 289-296.
[98] SEMI, SEMI PV17-1012 - Specification for Virgin Silicon Feedstock Materials for Photovoltaic Applications, Photovoltaic, 2012.
[99] J. Lindroos, H. Savin, Review of light-induced degradation in crystalline silicon solar cells, Solar Energy Materials and Solar Cells 147 (2016) 115-126.
[100] P.B. B. Sopori, S. Shet, V. Mehta, J. Binns, J. Appel, Understanding Light-Induced Degradation of c-Si Solar Cells, NREL, 2012.
[101] G. Zoth, W. Bergholz, A Fast, Preparation-Free Method to Detect Iron in Silicon, Journal of Applied Physics 67(11) (1990) 6764-6771.
[102] D.H. Macdonald, L.J. Geerligs, A. Azzizi, Iron detection in crystalline silicon by carrier lifetime measurements for arbitrary injection and doping, Journal of Applied Physics 95(3) (2004) 1021-1028.
[103] C. Modanese, M. Di Sabatino, A.-K. Søiland, K. Peter, L. Arnberg, Investigation of bulk and solar cell properties of ingots cast from compensated solar grade silicon, Progress in photovoltaics: research and applications 19(1) (2011) 45-53.
[104] T. Narushima, A. Yamashita, C. Ouchi, Y. Iguchi, Solubilities and Equilibrium Distribution Coefficients of Oxygen and Carbon in Silicon, Materials Transactions 43(8) (2002) 2120-2124.
[105] J.D. Murphy, R.E. McGuire, K. Bothe, V.V. Voronkov, R.J. Falster, Minority carrier lifetime in silicon photovoltaics: The effect of oxygen precipitation, Solar Energy Materials and Solar Cells 120 (2014) 402-411.
[106] J.D. Murphy, M. Al-Amin, K. Bothe, M. Olmo, V.V. Voronkov, R.J. Falster, The effect of oxide precipitates on minority carrier lifetime in n-type silicon, Journal of Applied Physics 118(21) (2015).
[107] G. Du, N. Chen, P. Rossetto, On-wafer investigation of SiC and Si_3N_4 inclusions in multicrystalline Si grown by directional solidification, Solar Energy Materials and Solar Cells 92(9) (2008) 1059-1066.
[108] J. Bauer, O. Breitenstein, J.P. Rakotoniaina, Electronic activity of SiC precipitates in multicrystalline solar silicon, Phys. Status Solidi A 204(7) (2007) 2190-2195.
[109] W. von Ammon, P. Dreier, W. Hensel, U. Lambert, L. Koster, Influence of oxygen and nitrogen on point defect aggregation in silicon single crystals, European Materials Research Society Symposia Proceedings 36 (1996) 33-41.

[110] D. Macdonald, Iron in Crystalline Silicon Solar Cells, in: UNSW (Ed.) SPREE, YouTube, 2013.
[111] A. Rohatgi, J.R. Davis, R.H. Hopkins, P. Rai-Choudhury, P.G. McMullin, Effect of Titanium, Copper and Iron on Silicon Solar Cells, Solid-State Electronics 23 (1980) 415-422.
[112] J. Lindroos, D.P. Fenning, D.J. Backlund, E. Verlage, A. Gorgulla, S.K. Estreicher, H. Savin, T. Buonassisi, Nickel: A very fast diffuser in silicon, Journal of Applied Physics 113(20) (2013) 204906.
[113] H. Nordmark, M. Di Sabatino, M. Acciarri, J. Libal, S. Binetti, E.J. Øvrelid, J.C. Walmsley, R. Holmestad, EBIC, EBSD and TEM study of grain boundaries in multicrystalline silicon cast from metallurgical feedstock, 33rd IEEE Photovoltaic Specialists Conference, IEEE, San Diego, CA, USA, 2008.
[114] S. Pizzini, Advanced Silicon Materials for Photovoltaic Applications, 2012.
[115] R. Bock, P.P. Altermatt, J. Schmidt, R. Brendel, Formation of aluminum–oxygen complexes in highly aluminum-doped silicon, Semiconductor Science and Technology 25(10) (2010) 105007.
[116] F. Rollert, N.A. Stolwijk, H. Mehrer, Solubility, diffusion and thermodynamic properties of silver in silicon, Journal of Physics D: Applied Physics 20 (1987) 1148-1155.
[117] G. Gaspar, C. Modanese, H. Schøn, M. Di Sabatino, L. Arnberg, E.J. Øvrelid, Influence of Copper Diffusion on Lifetime Degradation in n-type Czochralski Silicon for Solar Cells, Energy Procedia 77 (2015) 586-591.
[118] L. Mule'Stagno, A Technique For Delineating Defects in Silicon, Solid State Phenomena 82-84 (2002) 753-758.
[119] J. Schön, H. Habenicht, W. Warta, M.C. Schubert, Chromium distribution in multicrystalline silicon: comparison of simulations and experiments, Progress in Photovoltaics: Research and Applications (2012) 676-680.
[120] M.A. Jensen, J. Hofstetter, A.E. Morishige, G. Coletti, B. Lai, D.P. Fenning, T. Buonassisi, Synchrotron-based analysis of chromium distributions in multicrystalline silicon for solar cells, Applied Physics Letters 106(20) (2015) 202104.
[121] V. Naumann, D. Lausch, C. Hagendorf, Sodium Decoration of PID-s Crystal Defects after Corona Induced Degradation of Bare Silicon Solar Cells, Energy Procedia 77 (2015) 397-401.
[122] B. Ziebarth, M. Mrovec, C. Elsässer, P. Gumbsch, Potential-induced degradation in solar cells: Electronic structure and diffusion mechanism of sodium in stacking faults of silicon, Journal of Applied Physics 116(9) (2014) 093510.
[123] J.C. Shelton, H.R. Patil, J.M. Blakely, Equilibrium segregation of carbon to a nickel (111) surface: a surface phase transition, Surface Science 43 (1974) 493-520.
[124] M.P. Seah, Interface adsorption, embrittlement and fracture in metallurgy, Surface Science 53 (1975) 168-212.
[125] D. Raabe, M. Herbig, S. Sandlöbes, Y. Li, D. Tytko, M. Kuzmina, D. Ponge, P.P. Choi, Grain boundary segregation engineering in metallic alloys: A pathway to the design of interfaces, Current Opinion in Solid State and Materials Science 18(4) (2014) 253-261.
[126] S.A. McHugo, R.J. McDonald, A.R. Smith, D.L. Hurley, E.R. Weber, Iron solubility in highly boron-doped silicon, Applied Physics Letters 73(10) (1998) 1424-1426.
[127] S.M. Myers, M. Seibt, W. Schröter, Mechanisms of transition-metal gettering in silicon, Journal of Applied Physics 88(7) (2000) 3795.
[128] M. Seibt, V. Kveder, Gettering Processes and the Role of Extended Defects, in: S. Pizzini (Ed.), Advanced Silicon Materials for Photovoltaic Applications, John Wiley & Sons, Ltd., Chichester, United Kingdom, 2012.
[129] R. Kvande, L.J. Geerligs, G. Coletti, L. Arnberg, M. Di Sabatino, E.J. Øvrelid, C.C. Swanson, Distribution of iron in multicrystalline silicon ingots, Journal of Applied Physics 104(6) (2008) 064905.
[130] A. Bentzen, Phosphorus diffusion and gettering in silicon solar cells, PhD thesis, Department of Physics, University of Oslo, Oslo, Norway, 2006.
[131] R. Falster, M. Cornara, D. Gambaro, M. Olmo, Ideal Oxygen Precipitating Silicon Wafers and Oxygen Out-Diffusionless Process Therefor, US6306733B1, 2001.

[132] R. Falster, V.V. Voronkov, The engineering of intrinsic point defects in silicon wafers and crystals, Materials Science and Engineering B 73 (2000) 87-94.
[133] M. Al-Amin, J.D. Murphy, Increasing minority carrier lifetime in as-grown multicrystalline silicon by low temperature internal gettering, Journal of Applied Physics 119 (2016).
[134] M. Rinio, A. Yodyunyong, S. Keipert-Colberg, Y.P.B. Mouafi, D. Borchert, A. Montesdeoca-Santana, Improvement of multicrystalline silicon solar cells by a low temperature anneal after emitter diffusion, Progress in Photovoltaics: Research and Applications 19(2) (2011) 165-169.
[135] J.D. Murphy, R.E. McGuire, K. Bothe, V.V. Voronkov, R.J. Falster, Competitive gettering of iron in silicon photovoltaics: Oxide precipitates versus phosphorus diffusion, Journal of Applied Physics 116(5) (2014) 053514.
[136] M.S. Wiig, K. Adamczyk, H. Haug, K.E. Ekstrøm, R. Søndenå, The Effect of Phosphorus Diffusion Gettering on Recombination at Grain Boundaries in HPMC-Silicon Wafers, Energy Procedia 92 (2016) 886-895.
[137] J. Schön, A. Haarahiltunen, H. Savin, D.P. Fenning, T. Buonassisi, W. Warta, M.C. Schubert, Analyses of the Evolution of Iron-Silicide Precipitates in Multicrystalline Silicon During Solar Cell Processing, IEEE Journal of Photovoltaics 3(1) (2013) 131-137.
[138] C. del Canizo, A. Luque, A comprehensive model for the gettering of lifetime-killing impurities in silicon, Journal of the Electrochemical Society 147(7) (2000) 2685-2692.
[139] F. Duerinckx, J. Szlufcik, Defect passivation of industrial multicrystalline solar cells based on PECVD silicon nitride, Solar Energy Materials and Solar Cells 72 (2002) 231-246.
[140] S. Martinuzzi, Hydrogen passivation of defects in multicrystalline silicon solar cells, Solar Energy Materials and Solar Cells 80(3) (2003) 343-353.
[141] B.J. Hallam, P.G. Hamer, S. Wang, L. Song, N. Nampalli, M.D. Abbott, C.E. Chan, D. Lu, A.M. Wenham, L. Mai, N. Borojevic, A. Li, D. Chen, M.Y. Kim, A. Azmi, S. Wenham, Advanced Hydrogenation of Dislocation Clusters and Boron-oxygen Defects in Silicon Solar Cells, Energy Procedia 77 (2015) 799-809.
[142] B. Sopori, X. Deng, J.P. Benner, A. Rohatgi, P. Sana, S.K. Estreicher, Y.K. Park, M.A. Roberson, Hydrogen in silicon: current understanding of diffusion and passivation mechanisms, Twenty Fourth IEEE Photovoltaic Specialists Conference, IEEE, Waikoloa, HI, USA, 1994.
[143] P. Hamer, B. Hallam, R.S. Bonilla, P.P. Altermatt, P. Wilshaw, S. Wenham, Modelling of hydrogen transport in silicon solar cell structures under equilibrium conditions, Journal of Applied Physics 123(4) (2018) 043108.
[144] P. Karzel, A. Frey, S. Fritz, G. Hahn, Influence of hydrogen on interstitial iron concentration in multicrystalline silicon during annealing steps, Journal of Applied Physics 113 (2013) 114903.
[145] A.Y. Liu, C. Sun, V.P. Markevich, A.R. Peaker, J.D. Murphy, D. Macdonald, Gettering of interstitial iron in silicon by plasma-enhanced chemical vapour deposited silicon nitride films, Journal of Applied Physics 120(19) (2016) 193103.
[146] S. Castellanos, K.E. Ekstrom, A. Autruffe, M.A. Jensen, A.E. Morishige, J. Hofstetter, P. Yen, B. Lai, G. Stokkan, C. del Canizo, T. Buonassisi, High-Performance and Traditional Multicrystalline Silicon: Comparing Gettering Responses and Lifetime-Limiting Defects, IEEE Journal of Photovoltaics 6(3) (2016) 632-640.
[147] X. Cheng, Development and Characterization of Surface Passivation Materials on Silicon Wafers for Solar Cells, PhD thesis, Department of Materials Science and Engineering, Norwegian University of Science and Engineering, Trondheim, Norway, 2017.
[148] T. Trupke, R.A. Bardos, M.C. Schubert, W. Warta, Photoluminescence imaging of silicon wafers, Applied Physics Letters 89(4) (2006).
[149] R.A. Sinton, A. Cuevas, M. Stuckings, Quasi-steady-state photoconductance, a new method for solar cell material and device characterization, Twenty Fifth IEEE Photovoltaics Specialists Conference, IEEE, Washington, DC, USA, 1996.
[150] M. Taguchi, A. Terakawa, E. Maruyama, M. Tanaka, Obtaining a higherVoc in HIT cells, Progress in Photovoltaics: Research and Applications 13(6) (2005) 481-488.

[151] R.A. Schwartzer, A.J. Schwartz, M. Kumar, B.L. Adams, D.P. Field, Present State of Electron Backscatter Diffraction and Prospective Developments, in: A.J. Schwartz, M. Kumar, B.L. Adams, D.P. Field (Eds.), Electron Backscatter Diffraction in Materials Science, Springer, Boston, MA, USA, 2009.
[152] F. Secco d'Aragona, Dislocation Etch for (100) Planes in Silicon, J. Electrochem. Soc 119(7) (1972) 948-951.
[153] B. Sopori, A New Defect Etch for Polycrystalline Silicon, J. Electrochem. Soc 131 (1984) 667-672.
[154] M. Wright Jenkins, A New Preferential Etch for Defects in Silicon Crystals, J. Electrochem. Soc 124(5) (1977) 757-762.
[155] H. Robbins, B. Schwartz, Chemical etching of silicon I. The system HF, HNO3 and H2O, J. Electrochem. Soc 106(6) (1959) 505-508.
[156] W. Kern, The Evolution of Silicon Wafer Cleaning Technology, Journal of The Electrochemical Society 137(6) (1990) 1887-1892.
[157] B. Sopori, Extending PVSCAN to Meet the Market Needs for High-Speed, Large-Area Scanning, 9th Workshop on Crystalline Silicon Solar Cell Materials and Processes, National Renewable Energy Laboratory, Breckenridge, Colorado, 1999.
[158] C.A. Schneider, W.S. Rasband, K.W. Eliceiri, NIH Image to ImageJ: 25 years of image analysis, Nature Methods 9(7) (2012) 671-675.
[159] T.Z. Hossain, Neutron Activation Analysis, in: R.C. Brundle, C. Evans, S. Wilson, L.E. Fitzpatrick (Eds.), Encyclopedia of Materials Characterization, Butterworth-Heinemann1992.
[160] T.C. Huang, X-Ray Fluorescence, in: R.C. Brundle, C. Evans, S. Wilson, L.E. Fitzpatrick (Eds.), Encyclopedia of Materials Characterization, Butterworth-Heinemann1992.
[161] Z. Cai, B. Lai, W. Yun, I. McNulty, A. Khounsary, J. Maser, P. Ilinski, D. Legnini, E. Trakhtenberg, S. Xu, B. Tieman, G. Wiemerslage, E. Gluskin, Performance of a high-resolution x-ray microprobe at the Advanced Photon Source, in: P. Pianetta, J. Arthur, S. Brennan (Eds.) Synchrotron Radiation Instrumentation: SRI99, American Institute of Physics Conference Proceedings, Stanford, California, USA, 1999, pp. 31-34.
[162] D.A. Clugston, P.A. Basore, PC1D version 5: 32-bit solar cell modeling on personal computers, Twenty-Sixth IEEE Photovoltaic Specialists Conference, IEEE, Anaheim, CA, USA, 1997.

Paper I

Article I:

Grain boundary effect on lifetime in high performance multicrystalline silicon during solar cell processing

K. Adamczyk, R. Søndenå, M. Mhamdi, A. Autruffe, G. Stokkan, M. Di Sabatino, 2016,
Physica Status Solidi C, vol. 13, issue 10-12, p. 812-815

Phys. Status Solidi C **13**, No. 10–12, 812–815 (2016) / **DOI** 10.1002/pssc.201600059

physica status solidi c
www.pss-c.com
current topics in solid state physics

Grain boundary effect on lifetime in high performance multicrystalline silicon during solar cell processing

Krzysztof Adamczyk[*,1], **Rune Søndenå**[2], **Mohammed Mhamdi**[1,3], **Antoine Autruffe**[1], **Gaute Stokkan**[4], **and Marisa Di Sabatino**[1]

[1] Department of Materials Science and Engineering, NTNU, 7491 Trondheim, Norway
[2] Department of Solar Energy, IFE, 2007 Kjeller, Norway
[3] Sintef Materials and Chemistry, 0314 Oslo, Norway
[4] Sintef Materials and Chemistry, 7465 Trondheim, Norway

Received 14 May 2016, revised 27 May 2016, accepted 2 June 2016
Published online 13 July 2016

Keywords silicon, solar cells, gettering, hydrogenation, grain boundaries

---

[*] Corresponding author: e-mail krzysztof.adamczyk@ntnu.no

High performance multicrystalline silicon wafers used in solar cell processing have been investigated with focus on quantification of the grain boundary effect on lifetime. The lifetime of a set of 16 wafers from different positions along the ingot and after different process steps – phosphorus gettering, SiN_x:H layer deposition and firing – is measured by µPCD and compared with microstructural information from EBSD. This allows for analysis of the behaviour of grain boundaries and their influence on lifetime during solar cell processing. The minority carrier lifetime of HPMC-Si wafers is not increased after the gettering step, but even reduced for some samples. It is shown that the lifetime in areas close to grain boundaries is reduced during the gettering step and this has a stronger effect on the average value than the improvement within the grains. Only wafers after both gettering and hydrogenation show an overall improvement in carrier lifetimes. However, in the regions close to the bottom of the ingot, wafers show lifetime degradation after the hydrogenation process. The results are used to obtain quantitative information on recombination velocity of grain boundaries.

© 2016 WILEY-VCH Verlag GmbH & Co. KGaA, Weinheim

1 Introduction

Multicrystalline silicon (mc-Si) is widely used in the photovoltaic industry, despite the performance limiting defects and impurities that are abundant in this material [1, 2]. One route to improve efficiency is to use the so-called high performance multicrystalline silicon (HPMC-Si). The structure of such material is based on reduced grain size and increased number of random grain boundaries, which correlates to an overall reduced dislocation density and a lower number of dislocation clusters [3]. Recombination activity of both grain boundaries and dislocations has been shown to correlate to the level of impurity content in the material [4, 5]. Conventional multicrystalline silicon has been studied extensively in regard to changes in defect recombination activity during solar cell processing [6-8]. Two main process steps affecting this mechanism are phosphorus diffusion gettering and hydrogenation. Gettering has a thermal budget high enough to allow impurity diffusion towards the electrically inactive emitter, but also to dissolve precipitates decorating bulk defects. This leads to a competition between the extraction of harmful, interstitial impurity atoms from the bulk and impurity re-precipitation with a different precipitate distribution, possibly leading to new defect mechanisms [9, 10]. Subsequent contact firing, usually with a hydrogen rich antireflection coating present, also requires high temperatures. Even though the firing time is much shorter than the gettering process, it can also affect impurity distribution [9]. During the firing step hydrogen from passivation layers or antireflection coatings is able to diffuse into the bulk and passivate bulk defects, reducing their impact on minority carrier lifetimes [11]. In conventional multicrystalline p-type material the response to these processes varies, depending on process conditions and initial impurity content and distribution. In general, it is assumed that gettering increases the average bulk carrier lifetime in multicrystalline silicon by removing impurities, while hydrogenation has a positive effect on the recombination strength in crystal de-

© 2016 WILEY-VCH Verlag GmbH & Co. KGaA, Weinheim

fects. There are differences between conventional mc-Si and the HPMC-Si studied in this work, mostly due to different defect distribution. While conventional mc-Si suffers from dislocations multiplicating in relatively large grains, HPMC-Si is characterized by reduced grain size and more random angle grain boundaries, on which dislocations annihilate. These different defect distributions result in different behaviour upon solar cell processing [12]. This work investigates this behaviour in industrially processed wafers.

2 Experimental methods

The material used in this study comes from an ingot solidified, wafered and processed largely in industrial conditions. Sample wafers were taken from 4 different positions in the ingot, at 6, 25, 43 and 62% of relative height. Neighbouring wafers from each position were divided in 4 different groups. The sample groups have been processed as presented in Fig. 1.

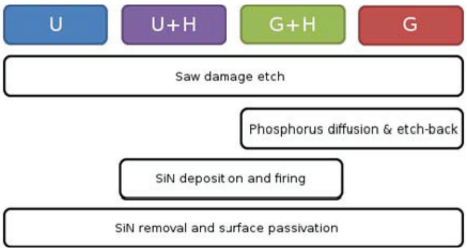
U
U+H
G+H
G
Saw damage etch
Phosphorus diffusion & etch-back
SiN deposition and firing
SiN removal and surface passivation

Figure 1 Processing scheme for the experiment. U and G refer to ungettered and gettered, respectively. H represents an additional hydrogenation process, i.e. a simulated contact firing with a SiN-layer present.

State-of-the-art industrial processing was utilized for both high temperature steps. All samples, both gettered and ungettered, are etched for the same amount of time in order to obtain comparable surface properties. After the industrial processing, hydrogenated samples had their SiN layer removed. Prior to minority carrier lifetime measurements the surfaces were electrically passivated by deposition of approximately 40 nm hydrogenated amorphous silicon on both sides, followed by a short anneal [13]. Sample lifetime has been mapped with µPCD (microwave photoconductive decay) on a WT-2000PVN instrument from Semilab. After lifetime measurements, the samples were polished down to 1 µm for electron backscatter diffraction (EBSD), which was performed on Jeol SEM – JSM 840, with Nordif EBSD detector. Grain boundaries have been classified as coincident site lattice (CSL) boundaries vs. random angle grain boundaries according to the Palumbo criterion [14]. Sub-grain boundaries with misorientation angle below 5° are not detected.

Carrier lifetimes values in the intra-grain area and on the recombination active grain boundaries have been averaged from plateau and peak values in linescans perpendicular to recombination active grain boundaries.

The lifetime-prediction model, designed in Comsol, is based on Donolato's theory on dislocation recombination strength [15, 16]. The model has been designed to fit the predicted lifetime to linescans perpendicular to GBs. Measured intra-grain lifetime (τ_0) has been used to adjust for intra-grain dislocation recombination. The boundary's recombination velocity S was obtained by fitting predicted lifetime values to measured linescans.

3 Results and discussion

EBSD measurements show that wafers along the ingot contain on average 49% CSL $\Sigma3$ boundaries, and 39% random angle grain boundaries. Σ 9 and Σ 27 grain boundaries have also been detected, with average share of 8 and 4%, respectively. Of the two dominating grain boundary orientations $\Sigma3$ GBs are the least, and random angle grain boundaries are the most recombination active [4]. Therefore the focus here is on random angle grain boundaries.

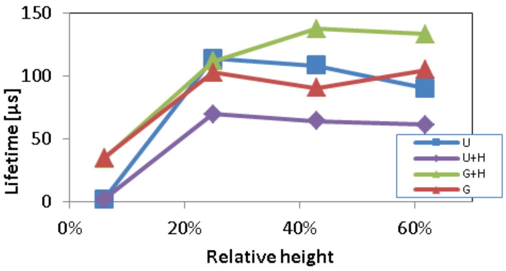

Figure 2 Mean lifetimes of measured HPMC-Si samples.

Mean lifetime values, shown in Fig. 2, indicate that for the middle part of the ingot both phosphorus gettering and a subsequent hydrogenation step are required in order to exceed the ungettered lifetime. Both gettering and hydrogenation will, if used separately, deteriorate the wafer electrical performance in the middle of the ingot. This HPMC-Si behaviour is different from the results presented by Karzel et al. for a standard multicrystalline wafer, where gettering resulted in increasing values relative to the ungettered state, but is in agreement with observations by other works on mc-Si [6, 7, 13]. Improvement of lifetime only by gettering is obtained in the bottom of the ingot, at 6% of the ingot height. Impurities dissolved in the lattice are more easily gettered than those in precipitates. The ratio between dissolved and precipitated impurities is higher in bottom wafers, where the total amount of impurities is higher due to in-diffusion from the crucible during cooling of the ingot. In order to distinguish between the random angle GBs in the bottom area and the middle of the ingot, samples from 6% height are discussed separately from samples from 25, 43 and 62% of height.

© 2016 WILEY-VCH Verlag GmbH & Co. KGaA, Weinheim

3.1 Bottom of ingot

Lifetime images and values in the bottom part of the ingot are presented in Fig. 3 and in Table 1, respectively.

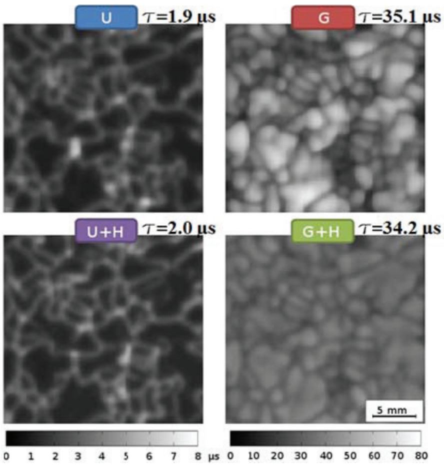

Figure 3 Spatially correlated lifetime maps of neighbouring wafers from about 6% relative height, processed in different routes. Note the different lifetime scales for gettered and ungettered samples. Average lifetime for each map presented on its upper right corner.

Table 1 Lifetime values extracted from samples at 6% height. Both intra-grain and GB lifetime values were extracted from the maps using linescans. IG stands for intra-grain.

process	No. of GBs	IG avg. [µs]	IG std. dev.	GBs avg. [µs]	GBs std. dev.
U+H	65	1.5	0.2	2.5	0.3
U	58	1.4	0.4	2.4	0.5
G+H	58	37.9	2.8	30.8	2.5
G	50	49.4	8.8	33.9	6.5

The ingot fraction rich in impurities is mostly affected by gettering process. In ungettered state, both with and without a hydrogenation process, areas near grain boundaries show higher lifetime values than intra-grain. This is probably because grain boundaries act as precipitation sites while the ingot is cooling after solidification, resulting in denuded zones close to grain boundaries [17]. Lateral carrier diffusion leads to smearing in the images, and only the denuded zones close to grain boundaries are visible, while decreased lifetime values directly at the boundaries are not detected.

Gettering considerably improves the intra-grain lifetime and to a lesser extent lifetime measured at GBs. The intra-grain improvement is varied from grain to grain. Grain boundaries and dislocations are known to reduce the efficiency of the gettering process [18]. Hydrogen defect passivation is not effective in this ingot part. It leads to a slight decrease in both GB and intra-grain lifetime values relative the gettered state. In addition to reducing the intra-grain lifetime, the variation in lifetime between grains is reduced. Passivation of certain defects must be assumed.

3.2 Middle and top of ingot

In the middle of the ingot, where impurity levels are lower, lifetimes in both grains and GBs are higher. The data are presented in Fig. 4 and Table 2.

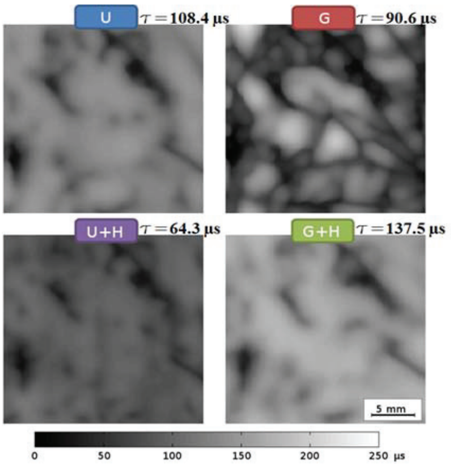

Figure 4 Spatially correlated lifetime maps of neighbouring wafers from about 43% relative height, processed in different routes. Average lifetime for each map presented on its upper right corner.

Table 2 Lifetime values extracted from samples at 25, 43 and 62% heights.

process	No. of GBs	IG avg. [µs]	IG std. dev.	GBs avg. [µs]	GBs std. dev.
U+H	22	82.3	9.4	65.7	9.5
U	34	134.6	20.0	106.8	17.2
G+H	18	143.1	17.2	113.0	20.2
G	47	159.0	41.0	97.9	25.7

Gettering increases intra-grain lifetimes from the ungettered state in the middle of the ingot by about 8%, but lifetimes measured near GBs deteriorate by 15%. Since the HPMC-Si material contains more GBs than conventional mc-Si, this effect leads to a reduction of average wafer lifetime. This is, however, mitigated by subsequent hydrogenation.

The results show that hydrogenation reduces the lifetime difference between GB and intra-grain areas from ungettered state, but it also deteriorates the mean lifetime of

© 2016 WILEY-VCH Verlag GmbH & Co. KGaA, Weinheim

the wafer. When hydrogenation is performed after gettering, the impurity concentration is already reduced in the active wafer part and since passivation reduces GB recombination, this leads to about 15% improvement of mean lifetime for the middle of the ingot.

3.3 Modeling results

Recombination strengths of 10 GBs are calculated using the lifetime prediction model. Linescans from samples from the middle of the ingot were used, and the study was limited to recombination active boundaries. The results are presented in Table 3.

Table 3 Recombination velocities (S) of GBs.

process	Avg. S [cm/s]	Std. dev. S [cm/s]
U+H	1106	871
U	816	584
G+H	800	708
G	1413	866

The model predictions are in line with values presented in previous section and show that gettering increases the recombination velocity of grain boundaries, but this effect is then reduced by hydrogenation, which allows full lifetime improvement. When hydrogenation is applied without previous gettering, recombination velocity decreases. Highest recombination velocities are shown after gettering without hydrogenation, but since intra-grain lifetime is also increased by gettering, the average measured GB lifetime is not far from that on ungettered samples. Both hydrogenation and gettering increase recombination velocity when applied without the other. This suggests that the associated heat treatments activate new defects or the precipitate distribution rearranges.

4 Conclusions

Combining microstructural analysis with electrical properties measurements gives good insight into the mechanisms governing wafer performance. We have shown that in the middle section of commercially available ingots both gettering and hydrogenation are needed to achieve lifetime improvement from the ungettered state. The mean lifetime of wafers from the main part of the ingot studied in this work improved by approximately 15%. Gettering alone deteriorates the average wafer lifetime relative to ungettered state, even though intra-grain lifetime is increased, because of the increased recombination activity of random angle grain boundaries after this step. The firing required for hydrogenation used without previous gettering also has a negative effect on mean wafer lifetime.

This is also confirmed by a lifetime prediction model, which shows that the values measured on samples from middle of the ingot can be obtained when the recombination velocity of grain boundaries increases by gettering, and is subsequently reduced by hydrogenation. For samples hydrogenated without gettering the model also predicts increased recombination velocities.

Bottom wafers react differently to processing due to higher impurity content. While hydrogenation has minor effect on such wafers, gettering can enhance their quality considerably, mainly by removing fast diffusing impurities.

Acknowledgements The work reported in this paper was performed in the project Impurity Control in High Performance Multicrystalline Silicon, 228930/E20, funded by the Norwegian Research Council's ENERGIX programme and industry partners REC Solar, REC Silicon, Steuler Solar and The Quartz Corp.

References

[1] International Technology Roadmap for Photovoltaic (ITRPV.net), Results 2015, 7th ed., vers. 2, 2016.
[2] L. Arnberg, M. Di Sabatino, and E. J. Øvrelid, J. Cryst. Growth **360**, 56 (2012).
[3] C. W. Lan, W. C. Lan, T. F. Lee, A. Yu, Y. M. Yang, W. C. Hsu, B. Hsu, and A. F. Yang, J. Cryst. Growth **360**, 68 (2012).
[4] J. Chen, T. Sekiguchi, D. Yang, F. Yin, K. Kido and S. Tsurekawa, J. Appl. Phys. **96**, 5490 (2004).
[5] M. I. Bertoni, D. P. Fenning, M. Rinio, V. Rose, M. Holt, J. Maser, and T. Buonassisi, Energy Environ. Sci. **4**, 4252 (2011).
[6] M. Rinio, A. Yodyungyong, S. Keipert-Colberg, D. Borchert, and A. Montesdeoca-Santana, Phys. Status Solidi A **208**, 760 (2011).
[7] P. Karzel, M. Ackermann, L. Gröner, C. Reimann, M. Zschorsch, S. Meyer, F. Kiessling, S. Riepe, and G. Hahn, J. Appl. Phys. **114**, 244902 (2013).
[8] H. C. Sio, S. P. Phang, T. Trupke, and D. Macdonald, IEEE J. Photovolt. **5**, 1357 (2015).
[9] A. E. Morishige, H. S. Laine, J. Schön, A. Haarahiltunen, J. Hofstetter, C. del Cañizo, M. C. Schubert, H. Savin, and T. Buonassisi, Appl. Phys. A **120**, 1357 (2015).
[10] M. S. Wiig , K. Adamczyk, H. Haug, K. E. Ekstrøm, and R. Søndenå, Energy Procedia (2016) (to be published).
[11] B. Sopori, J. Electron. Mater. **31**, 972 (2002).
[12] S. Castellanos, K. E. Ekstrøm, A. Autruffe, M. A. Jensen, A. E. Morishige, J. Hofstetter, P. Yen, B. Lai, G. Stokkan, C. del Canizo, and T. Buonassisi, IEEE J. Photovolt. **6,** 632 (2016).
[13] R. Søndenå, J. Gjessing, H. Angelskår, Ø. Norseth, S. E. Foss, and E. S. Marstein, in: 28th EUPVSEC, Paris, France, 2013.
[14] G. Palumbo, K. T. Aust, E. M. Lehockey, U. Erb, and P. Lin, Scr. Mater. **38**, 1685 (1998).
[15] C. Donolato, J. Appl. Phys. **84**, 2656 (1998).
[16] G. Stokkan, S. Riepe, O. Lohne, and W. Warta, J. Appl. Phys. **101**, 053515 (1998).
[17] M. Knörlein, A. Autruffe, R. Søndenå, and M. Di Sabatino, Energy Procedia **55**, 539 (2014).
[18] A. Bentzen and A. Holt, Mater. Sci. Eng. B **159-160**, 228 (2009).

© 2016 WILEY-VCH Verlag GmbH & Co. KGaA, Weinheim

Paper II

Article II:

The effect of phosphorus diffusion gettering on recombination at grain boundaries in HPMC-Silicon wafers

M. S. Wiig, K. Adamczyk, H. Haug, K. E. Ekstrøm, R. Søndenå, 2016, Energy Procedia, vol. 92, p. 886-895

Available online at www.sciencedirect.com

ScienceDirect

Energy Procedia 92 (2016) 886 – 895

Energy Procedia

6th International Conference on Silicon Photovoltaics, SiliconPV 2016

The effect of phosphorus diffusion gettering on recombination at grain boundaries in HPMC-Silicon wafers

Marie S. Wiig[a*], Krzysztof Adamczyk[b], Halvard Haug[a], Kai E. Ekstrøm[b], Rune Søndenå[a]

[a]*Institute for Energitechnology, Instituttveien 18, 2007 Kjeller, Norway*
[b]*Norwegian University for Science and Technology, Alfred Getz vei 2, 7491 Trondheim, Norway*

Abstract

The influence of phosphorus diffusion gettering on recombination at grain boundaries has been studied in a commercially cast high performance multicrystalline silicon block. Wafers from four different heights have been studied with high resolution photoluminescence-imaging. The recombination at grain boundaries was studied from linescans perpendicular to the grain bounadary of interest. The change in recombination activity at grain boundaries after gettering has been correlated with grain orientation measured by electron backscatter diffraction and classified according to Brandon criterion. The relative change in carrier lifetime after gettering depends on the height in the cast, and is very sensitive to the injection level. Iron concentrations were also found from photoluminescence-imaging of iron in Fe_i and FeB states, respectively. After gettering recombination grain boundaries in the middle section of the ingot has become strongly recombination active. $Fe_{i,}$ has been efficiently removed and no longer constitute the main recombination path at any height.

© 2016 Published by Elsevier Ltd. This is an open access article under the CC BY-NC-ND license
(http://creativecommons.org/licenses/by-nc-nd/4.0/).
Peer review by the scientific conference committee of SiliconPV 2016 under responsibility of PSE AG.

Keywords: Photoluminesce-imaging, grain boundary recombination, HPMC-Si, EBSD, \

---

1. Introduction

The performance of multicrystalline silicon (mc-Si) solar cells is limited by impurities, crystal defects and interactions thereof[1-3]. Crystal defects such as grain boundaries and dislocations are easily decorated with impurity species, forming recombination active defects in the material[4-6]. Dislocation clusters are especially

---

[*] Corresponding author. E-mail address: Marie.Syre.Wiig@ife.no

1876-6102 © 2016 Published by Elsevier Ltd. This is an open access article under the CC BY-NC-ND license
(http://creativecommons.org/licenses/by-nc-nd/4.0/).
Peer review by the scientific conference committee of SiliconPV 2016 under responsibility of PSE AG.
doi:10.1016/j.egypro.2016.07.098

detrimental to the minority carrier lifetime in conventional mc-Si as dislocations multiply and grow during solidification[7-9]. In addition phosphorus diffusion gettering (PDG) has proven to be less effective in removing impurities trapped by these crystal defects[10].

Recent years the industry has moved toward new methods for casting multicrystalline silicon ingots. High performance multicrystalline silicon (HPMC-Si) denotes mc-Si with improved material properties [11]. A seed layer or seed structure is typically used to control the initial growth of the ingot in order to avoid much of the dislocation growth[11, 12]. As a result HPMC-Si typically has smaller grain sizes, but less dislocations than conventional mc-Si[13]. However, smaller grain sizes alone is not beneficial for the minority carrier lifetime, as an increase in grain boundaries is implied. Improved understanding of the electrical properties of grain boundaries during the different solar cell processing steps is therefore important as it allows for further improvement of the final cell performance.

Phosphorus diffusion gettering is routinely used in solar cell processing to remove metallic impurities, and to form the emitter. PDG is commonly known to improve the lifetime of multicrystalline silicon[14], however, recent publications have shown a decrease in average lifetime despite the removal of metallic impurities during the gettering process[9, 15]. Increased recombination after PDG can in some cases be reversed by H-passivation after SiN-fireing[6, 16].

In the present work the effect of phosphorus diffusion gettering on the recombination activity of grain boundaries in commercially available HPMC-Si wafers is studied by investigating the photoluminescence of both passivated and non-passivated wafers. Gettered and ungettered wafers are compared in order to better understand the local effects on the recombination activity. Grain boundaries are classified using electron backscatter diffraction (EBSD).

2. Experimental

Four wafers from four positions in a commercially cast p-type high performance multicrystalline silicon block were studied. The processing of neighbouring wafers from each height is illustrated in Figure 1. Four wafers from each position were etched to remove saw damage. This etched state will later be referred to as ungettered. Phosphorus diffusion gettering at 835°C was then carried out on two wafers from each position, followed by etching to remove the diffused emitter. The samples were then split in two batches were one received double side surface passivation by hydrogenated amorphous silicon, the other half were kept unpassivated.

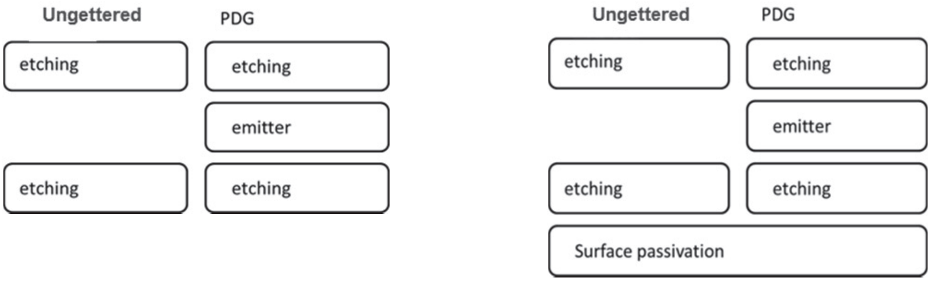

Fig. 1. Illustration of how the four samples from each height is processed.

Band-to-band photoluminescence (PL) imaging shows the local recombination activity with high resolution. From unpassivated images one can observe sharp features where strong recombination centres are present. The images show a 2x2 cm^2 area captured with a high magnification lens (20 pixels/mm) which resolves fine features not visible when imaging the full wafer. The recombination activity at and in the vicinity of grain boundaries has been studied from linescans perpendicular to the GB of interest in PL-images. For material with high lifetime and good surface passivation the diffusion length of carriers is sufficient to cause a smearing of the PL-signal, due to transport of carriers from high lifetime to low lifetime regions. The PL signal scales with excess carrier concentration ($\triangle$n) which is the sum of the recombination current (U) and net carrier diffusion. In order to eliminate this effect, and locate the region where the recombination actually takes place, unpassivated samples were evaluated. In this case the surface recombination is very high eliminating the contribution from net diffusion of carriers, beyond the wafer thickness.

Grain orientations have been found by EBSD and grain boundary degree of fit has been identified according to Brandon criterion.

PL imaging calibrated by harmonically modulated photoluminescence[17] in combination with metastable defect imaging provides images of the concentration of interstitial iron[18]. These measurements were performed at Fraunhofer ISE.

3. Results and Discussion

3.1. Lifetime and Fe-concentration

The mean lifetime measured by Quasi Steady State Photoconductance (QSSPC) along the height of the block before and after PDG is show in Figure 2. After PDG the lifetime in the top and bottom section with initially very low lifetimes improved. However, in the middle section of the block the mean lifetime slightly decreased after PDG. Iron imaging of wafers from the same positions showed a reduction of Fe_i concentration in top and bottom with approximately two orders of magnitude, and one order of magnitude in the middle section. In the ungettered top and bottom wafers almost 90% of the carrier recombination was due to Fe_i. In the middle section this fraction was around 35-50%, see more details in Table 1. After PDG Fe_i was no longer the dominating recombination path at any height.

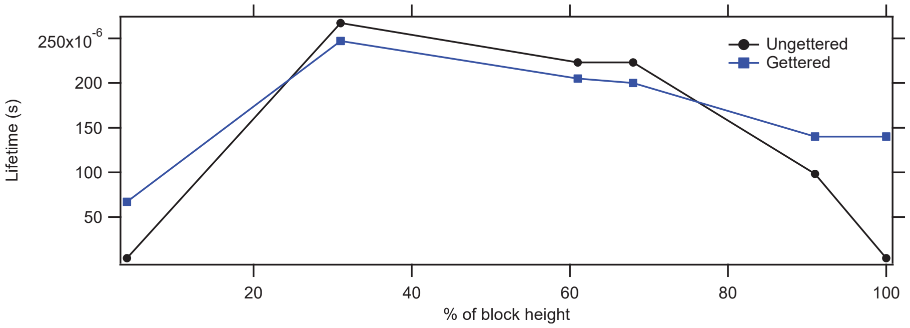

Fig. 2. QSSPC lifetime at 1e15 cm-3 (or maximum injection level) as a function of height in the block.

Table 1: Iron concentrations measured by metastable defect imaging photoluminescence imaging by calibrated by harmonically modulated photoluminescence. Calculated recombination fraction due to Fe_i.

	%Fe_i recomb. gettered	% Fe_i recomb. Ungettered	Fe_i gettered	Fe_i ungettered
Bottom	8.8%	87%	1.3e10	3e12
Lower center	2.7%	37%	2.6e9	3.4e10
Upper center	4.8%	48%	5.4e9	5.2e10
Topp	3.6%	88%	6.2e9	2.2e12

3.2. Bottom of ingot

PL-images of unpassivated samples do not suffer from smearing, which occur in PL-images of passivated samples with high lifetime. Figure 3 show distinct difference in recombination at and around the grain boundaries before and after PDG. The ungettered bottom wafer had highly recombination active grain boundaries in the ungettered state surrounded by a region of higher lifetime, seen as a bright region surrounding the GB in the PL-image. After PDG gettering, most GB's are still strong recombination centers but the bright region has vanished.

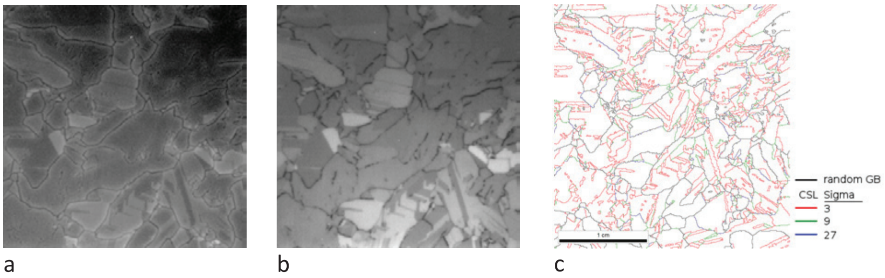

Fig. 3. High magification PL-image of an unpassivated a) ungettered and b) gettered wafer from the bottom section of the cast (4% of ingot height). EBSD map from same wafer position is shown in c).

A linescan perpendicular to a GB in the bottom wafer is shown in Figure 4. The average Fe_i concentration in this bottom wafer was reduced by two orders of magnitude and the overall lifetime after PDG increased.

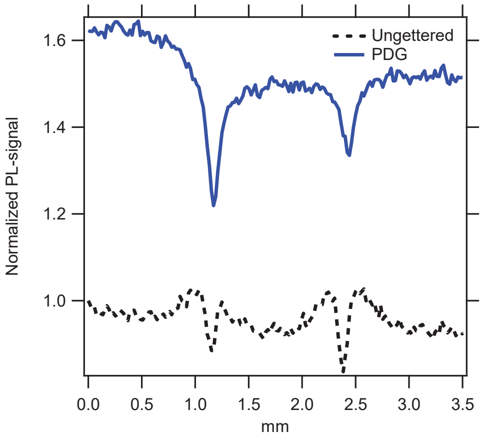

Fig. 4. Linescan from PL-image perpendicular to a GB. The black/dashed line represent the ungettered wafer.

The increased PL-signal next to the GB after PDG corresponds well with a denuded zone formed around the GB due internal gettering of impurities to precipitates formed during cooling of the ingot[5]. Grain boundaries are known as preferred nucleation sites for iron precipitation, there is a smaller barrier to growth of already existing precipitates, compared to the nucleation of new precipitates[19]. Attributing this denuded zone to diffusion of iron also agree well with profiles from high resolution iron imaging[5, 20]. The highly recombination active region observed in the centre of the grain boundary is likely due to existence of Fe precipitates. This phenomenon is only observed in the bottom region with high iron concentration. After PDG the denuded zone around the GB vanished. In literature EBIC studies has also revealed a denuded zone around moderately and heavy contaminated Σ27 and RA grain boundaries[21]. Σ3 GB's were inactive and unaffected by PDG, this has also been reported previously by others[22].

3.3. Middle section of ingot

Wafers from these centre positions represent typical properties in the major part of the ingot. Opposed to the highly recombining GB's in the ungettered bottom wafer, no strongly recombining grain boundaries are visible in the ungettered wafers from 30% and 60% of the block height, Figure 5. After PDG recombination at some of the GB's has been activated. Most of the strongly activated GB's have been classified as random angle (RA) and a few as $\Sigma27$. The inactive grain boundaries in the ungettered material may imply that there are no preexcisting precipitation sites around the GB's, resulting in a larger number of small precipitates and strong activation of recombination after PDG[23]. As in the bottom wafer GB's classified as $\Sigma3$ are inactive both before and after PDG.

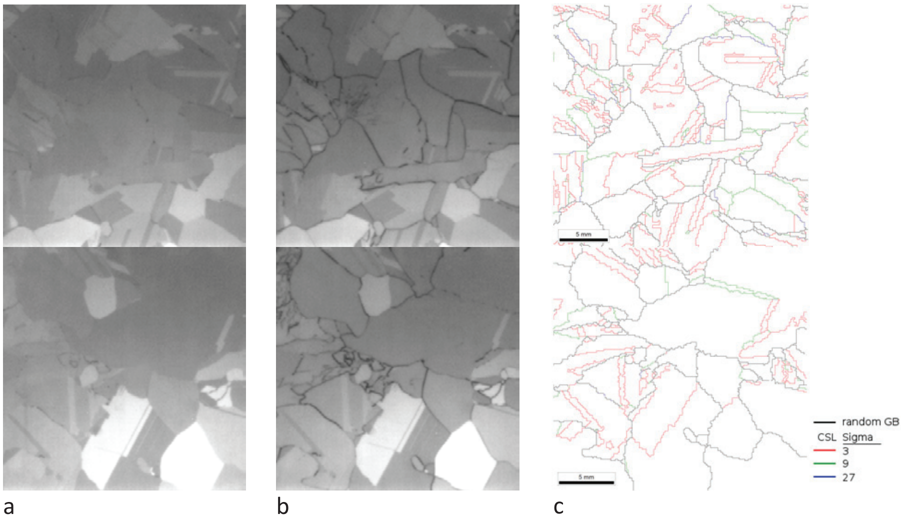

Fig. 5. High magification PL-image of unpassivated a) ungettered and b) gettered wafer from the middle section of the cast (Upper row 30% and lower row 60% of ingot height). EBSD map from same ingot height is shown in c).

A linescan for such an activated GB is shown in Figure 6. After PDG a previously inactive grain boundary has become strongly recombination active, as previously also reported by Rinio[6] and Geerlings[15]. Figure 6 shows the grain boundary as an abrupt decrease in the PL signal where it appears as a step in the PL signal between two adjacent grains in the ungettered sample. The higher levels of the left grain compared to the right is due to higher reflectivity, surface recombination velocities or light emission for different grain orientations. $\Sigma3$ grain boundaries between grains with equal bulk signal cannot be observed from the PL signal. Increased recombination in vicinity of GB's after PDG has previously been attributed out-diffusion of impurities, also referred to as bleeding or poisoning of the bulk silicon, from the grain boundaries during the high temperature emitter in-diffusion process[6]. Or it can be due to increased recombination activity of certain GB's after PDG[15, 19] due to precipitation.

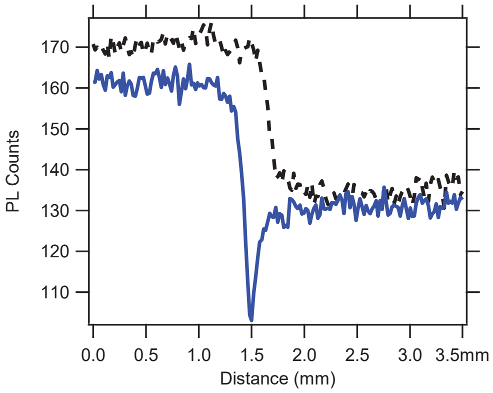

Fig. 6.PL signal at a RA grain boundary. Dashed line show ungettered and solid line is after PDG.

Figure 7b show coincidence of the inflection point ($d^2y/dx = 0$) of two peak fitted PL-signals (Figure 7a) of a grain boundary which were recombination active already in the ungettered state. The coincidence of the inflection point for these two profiles indicate that the width of the recombination active GB is unaffected by PDG. This indicates that the increased recombination after PDG in this case is rather due to increased precipitate density than out-diffusion of supersaturated dissolved impurity atoms from the extended defect[6, 24]. The rapid cooling after PDG freezes the small precipitates, which results in larger recombination activity than a few large precipitates formed during slow cooling of the ingot[15].

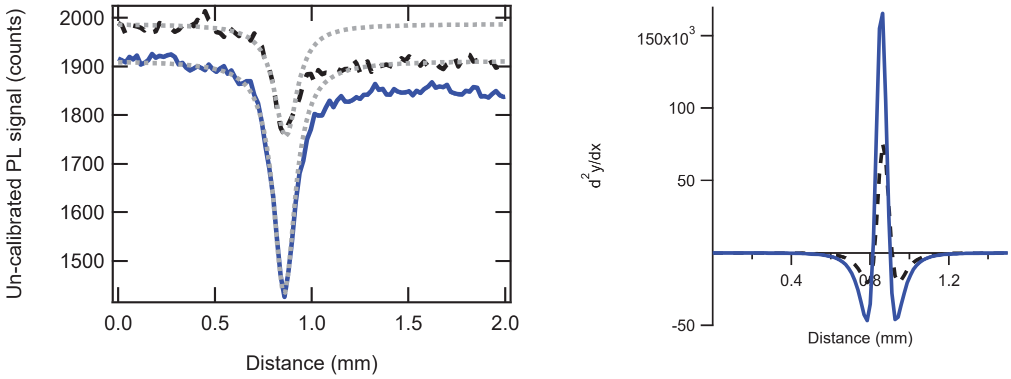

Fig. 7. (a) Uncalibrated PL signal at GB. Solid line PDG and dashed line ungettered samples. The dotted lines are peak fitted curves with respect to the left grain. Double derivatives of the peak fitted signals are shown in (b).

3.4. Upper section of ingot

In the top wafer the same GB's are recombination active both before and after PDG. Similar to all the samples from lower heights Σ3 GB's are inactive and unaffected by PDG. Only a few inactive Σ9 GB and no long Σ27 GB's were detected. Even though the iron concentration is comparable to the bottom section, there is no sign of a denuded zone which was observed in the bottom wafer. This can be because the top of a cast is allowed shorter time for diffusion of impurities after it has solidified.

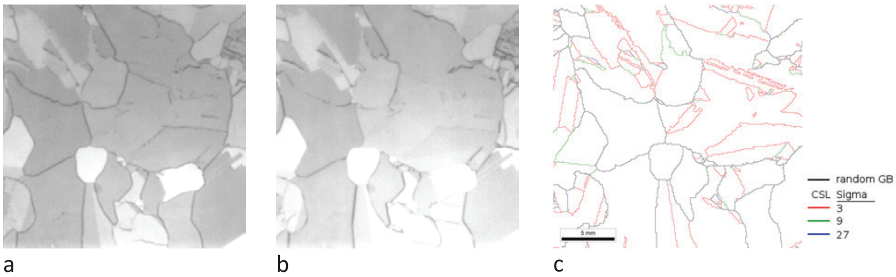

Fig. 8. High magification PL-image of an un-passivated a) ungettered and b) gettered wafer from the upper section of the cast (100% of wafered block height). EBSD map from same wafer position is shown in c).

3.5. Injection dependence of GB recombination

Recombination strength and injection dependence of the recombination processes has been studied on double side passivated wafers from the middle section of the ingot.

Fe_i was efficiently removed after PDG, and the typical crossover point in the QSSPC signature of Fe_i and FeB disappeared. Still the PL signal from the bulk grains measured after PDG was reduced. One reason for measuring a lower lifetime with QSSPC calibrated PL after PDG is strong recombination of carriers at the grain boundaries and diffusion of carriers toward this sink. This reduces the number of free carriers far into the bulk grains on samples with good surface passivation. On HPMC-Si with a small to moderate grain size this may dominate the measured lifetime after PDG, where real bulk lifetime values are never reached. This strong gradient in the injection level toward the GB's makes QSSPC calibration of the PL-signal to lifetime after PDG inaccurate. QSSPC calibration of PL-images depends on an injection dependent calibration constant which is not globally valid for strongly inhomogeneous samples. To study the injection dependent recombination uncalibrated images were acquired at different illumination flux. The recombination activity after PDG as a function of illumination intensity has been extracted from the uncalibrated PL-signal divided by illumination flux for bulk and GB's separately in Figure 9. After PDG there is a clear activation of recombination at the grain boundary relative to the neighboring grains. There is also an increased dissimilarity between different grains. However, whether there is an increase or decrease in recombination activity in the grains after PDG with respect to the ungettered state, depends on the injection conditions. At moderate to high injection there is an increase in the recombination activity after PDG, Figure 9c). However, at low injection the lifetime appears to improve, Figure 9b).

After PDG the recombination strength of the different grains and grain boundaries varies, but the dependence on illumination intensity is the same. This indicates that the recombination mechanism which limits the carrier lifetime is the same in bulk and at active GB's, but the concentration may vary depending on location.

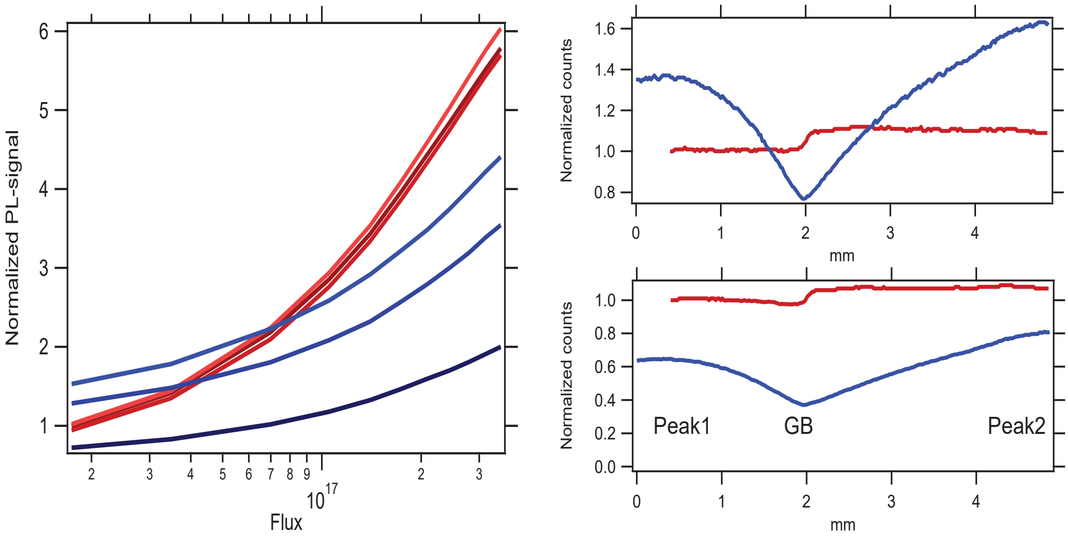

Fig. 9. (a) Normalized PL-signal (against Peak1 ungettered) vs illumination flux for Peak1, GB and Peak2. red) ungettered and blue) PDG. b) Linescans across a the grain boundary b) 1.7e16 and c) 2.1e17 Photons/cm2

The Fe_i concentrations are reduced by 90% or more by phosphorus diffusion gettering. If the Fe_i was the only recombination mechanism influenced by PDG, one would from Shockley-Read-Hall (SRH) recombination theory expect reduced injection dependence and improved lifetime after PDG. However, we observe a crossover point between the injection dependent recombination before and after PDG, Figure 9a. According to this an additional recombination mechanism has been activated after PDG, and it is active both in bulk and at GB's. This is in agreement with findings of Scott et al.[25] also ruling out iron as a cause for reduced lifetimes after gettering at increasing temperatures. It is currently not clear what this additional recombination mechanism is, however, dissolution of metal impurities with lower diffusivity and solid solubility[25] or precipitation within the grains[26] are possible candidates. Also in the ungettered state the recombination is not completely dominated by Fe_i as about half of the recombination processes are through other paths, of which some may be enhanced after PDG.

We observe a reduced injection dependence of the recombination at GB's after PDG. SiO et al.[23, 27] quantified recombination at GB's according to surface recombination velocity. Contrary to our finding they found two classes of GB's one with increased in injection dependence after PDG and one which had similar injection dependence before and after.

Recombination at GB's after PDG can be reduced after subsequent H-passivation during SiN-fireing[15, 16]. This may reduce the severity of GB activation on the final solar cell. The effect of H-passivation has not been part of this study.

4. Conclusion

The influence of PDG on recombination activity at the GB's strongly depends on the height in the cast. For all positons Σ3 CSL grain boundaries were unaffected by PDG. Grain boundaries in the bottom wafer were surrounded by a higher lifetime region, denuded zone. This was completely removed after PDG and the overall lifetime improved.

In the middle section of the ingot a large number of RA grain boundaries inactive in the ungettered state became recombination active after PDG gettering. Even though the recombination strength changed, the width of an initially recombination active GB remained constant after phosphorus diffusion. For the wafers from the middle section strong recombination at the grain boundaries caused strong gradients in the carrier density in the sample and enhanced diffusion toward the grain boundaries. These locally large gradients in carrier concentrations also made QSSPC calibrated lifetime less accurate and evaluating recombination from uncalibrated PL signal were preferred. After PDG recombination due to Fe_i has been reduced, however a new recombination path has been activated. This recombination path has the same injection dependence both on GB's and in bulk grains.

In the top wafer the same GB's were recombination active both before and after PDG.

Carrier recombination due to Fe_i is no longer the main lifetime limiting recombination path after PDG at any height. Only the top and bottom wafer positions with initially high iron concentration showed reduced recombination activity after PDG.

Acknowledgements

Funding was partly provided by the Norwegian Research Council and industry partners in Norway through the EnergiX programme. The authors would like to thank Florian Schindler and Martin Schubert for their support with Fe_i-measurements at Fraunhofer ISE and the European Community for funding within the frame of the SOPHIA project (7FP7-SOPHIA grant agreement n° 262533), which financed the measurements of dissolved iron.

References

[1] Coletti G, Sensitivity of state-of-the-art and high efficiency crystalline silicon solar cells to metal impurities, Progress in Photovoltaics: Research and Applications, 2013:21: 1163-1170.

[2] Kveder V, Kittler M, Schröter W, Recombination activity of contaminated dislocations in silicon: A model describing electron-beam-induced current contrast behavior, Physical Review B, 2001:63: 115208.

[3] Schindler F, Michl B, Schon J, et al., Solar Cell Efficiency Losses Due to Impurities From the Crucible in Multicrystalline Silicon, Photovoltaics, IEEE Journal of, 2014:4: 122-129.

[4] Buonassisi T, Istratov AA, Peters S, et al., Impact of metal silicide precipitate dissolution during rapid thermal processing of multicrystalline silicon solar cells, Applied Physics Letters, 2005:87: 121918.

[5] Liu AY, Walter D, Phang SP, et al., Investigating Internal Gettering of Iron at Grain Boundaries in Multicrystalline Silicon via Photoluminescence Imaging, Photovoltaics, IEEE Journal of, 2012:2: 479-484.

[6] Rinio M, Yodyungyong A, Keipert-Colberg S, et al., Recombination in ingot cast silicon solar cells, physica status solidi (a), 2011:208: 760-768.

[7] Ryningen B, Stokkan G, Kivambe M, et al., Growth of dislocation clusters during directional solidification of multicrystalline silicon ingots, Acta Materialia, 2011:59: 7703-7710.

[8] Stokkan G, Hu Y, Mjøs Ø, et al., Study of evolution of dislocation clusters in high performance multicrystalline silicon, Solar Energy Materials and Solar Cells, 2014:130: 679-685.

[9] Søndenå R, Gjessing J, Angelskår H, et al., Effect of dislocations on the electrical response of mulicrystalline silicon solar cells. , in: 28th European Photovoltaic Solar Energy Conference and Exhibition, Paris, 2013.

[10] Bentzen A, Holt A, Overview of phosphorus diffusion and gettering in multicrystalline silicon, Materials Science and Engineering: B, 2009:159–160: 228-234.

[11] Yang YM, Yu A, Hsu B, et al., Development of high-performance multicrystalline silicon for photovoltaic industry, Progress in Photovoltaics: Research and Applications, 2015:23: 340-351.

[12] Wong YT, Hsu C, Lan CW, Development of grain structures of multi-crystalline silicon from randomly orientated seeds in directional solidification, Journal of Crystal Growth, 2014:387: 10-15.

[13] Ekstrøm K, Stokkan G, Autruffe A, et al., Microstructure of multicrystalline silicon seeded by polysilicon chips and fluidized bed reactor granules, Journal of Crystal Growth, 2016: 95-100.

[14] Gindner S, Karzel P, Herzog B, et al., Efficacy of Phosphorus Gettering and Hydrogenation in Multicrystalline Silicon, Photovoltaics, IEEE Journal of, 2014:4: 1063-1070.

[15] Geerligs LJ, Komatsu Y, Rover I, et al., Precipitates and hydrogen passivation at crystal defects in n- and p-type multicrystalline silicon, J. Appl. Phys., 2007:102: 093702-093702-093709.

[16] Karzel P, Ackermann M, Gröner L, et al., Dependence of phosphorus gettering and hydrogen passivation efficacy on grain boundary type in multicrystalline silicon, J. Appl. Phys., 2013:114: 244902.

[17] Giesecke JA, Schubert MC, Michl B, et al., Minority carrier lifetime imaging of silicon wafers calibrated by quasi-steady-state photoluminescence, Solar Energy Materials and Solar Cells, 2011:95: 1011-1018.

[18] Macdonald D, Tan J, Trupke T, Imaging interstitial iron concentrations in boron-doped crystalline silicon using photoluminescence, J. Appl. Phys., 2008:103: 073710.

[19] Buonassisi T, Istratov AA, Pickett MD, et al., Chemical natures and distributions of metal impurities in multicrystalline silicon materials, Progress in Photovoltaics: Research and Applications, 2006:14: 513-531.

[20] Schubert MC, Habenicht H, Warta W, Imaging of Metastable Defects in Silicon, Photovoltaics, IEEE Journal of, 2011:1: 168-173.
[21] Chen J, Sekiguchi T, Yang D, et al., Electron-beam-induced current study of grain boundaries in multicrystalline silicon, J. Appl. Phys., 2004:96: 5490-5495.
[22] Takahashi I, Usami N, Mizuseki H, et al., Impact of type of crystal defects in multicrystalline Si on electrical properties and interaction with impurities, J. Appl. Phys., 2011:109: 033504.
[23] Sio HC, Phang SP, Trupke T, et al., Impact of Phosphorous Gettering and Hydrogenation on the Surface Recombination Velocity of Grain Boundaries in p-Type Multicrystalline Silicon, IEEE Journal of Photovoltaics, 2015:5: 1357-1365.
[24] Habenicht H, Riepe S, Schultz W, et al., Out-diffusion of metal from grain boundaries in multicrystalline silicon during thermal processing, in: EUPVSEC, Milan, Italy, 2007.
[25] Scott SM, Hofstetter J, Morishige AE, et al., Sacrificial high-temperature phosphorus diffusion gettering process for lifetime improvement of multicrystalline silicon wafers, in: Photovoltaic Specialist Conference (PVSC), 2014 IEEE 40th, 2014, pp. 3014-3016.
[26] Liu AY, Macdonald D, Precipitation of iron in multicrystalline silicon during annealing, J. Appl. Phys., 2014:115: 114901.
[27] Sio HC, Trupke T, Macdonald D, Quantifying carrier recombination at grain boundaries in multicrystalline silicon wafers through photoluminescence imaging, J. Appl. Phys., 2014:116: 244905.

Article III:

Recombination strength of dislocations in high-performance multicrystalline/quasi-mono hybrid wafers during solar cell processing

K. Adamczyk, R. Søndenå, C. C. You, G. Stokkan, J. Lindroos,
M. Rinio, M. Di Sabatino, 2018, Physica Status Solidi A, vol. 215,
issue 2, p. 1700493

Paper III

ORIGINAL PAPER

Silicon Hybrid Wafers

physica status solidi a

www.pss-a.com

Recombination Strength of Dislocations in High-Performance Multicrystalline/Quasi-Mono Hybrid Wafers During Solar Cell Processing

Krzysztof Adamczyk, Rune Søndenå, Chang Chuan You, Gaute Stokkan, Jeanette Lindroos, Markus Rinio, and Marisa Di Sabatino*

Wafers from a hybrid silicon ingot seeded in part for High Performance Multicrystalline, in part for a quasi-mono structure, are studied in terms of the effect of gettering and hydrogenation on their final Internal Quantum Efficiency. The wafers are thermally processed in different groups – gettered and hydrogenated. Afterwards, a low temperature heterojunction with intrinsic thin layer cell process is applied to minimize the impact of temperature. Such procedure made it possible to study the effect of different processing steps on dislocation clusters in the material using the Light Beam Induced Current technique with a high spatial resolution. The dislocation densities are measured using automatic image recognition on polished and etched samples. The dislocation recombination strengths are obtained by a correlation of the IQE with the dislocation density according to the Donolato model. Different clusters are compared after different process steps. The results show that for the middle of the ingot, the gettering step can increase the recombination strength of dislocations by one order of magnitude. A subsequent passivation with layers containing hydrogen can lead to a decrease in the recombination strength to levels lower than in ungettered samples.

1. Introduction

Crystalline silicon maintains its status as the main material used in solar cells. The latest reports show that multicrystalline silicon has gained more ground in the last years and made up 70% of the market in 2016.[1,2] While the Czochralski (CZ) crystallization technique provides high-quality monocrystalline material leading to higher cell efficiencies, the directional solidification of multicrystalline ingots allows for higher throughput and lower production costs, offsetting its lower efficiency.[3,4] Still much effort is aimed at decreasing the negative effect of structural defects on the device performance.[5,6] One approach is to control the structure of the final ingot by changing the nucleation phase, such as growing Quasi-Mono (QM) silicon[7] or High Performance Multicrystalline (HPMC) ingots.[8] Quasi-mono growth requires a seeding layer consisting of monocrystalline silicon slabs of specific orientation, which are laid out next to each other and melted partially, before the ingot starts to crystallize. This approach leads to a crystalline structure replicating that of the seeds. Defects originate from the joints between the seeds and from grains nucleated on the crucible walls.[9,10]

Seeding can also be used to grow HPMC-Si, e.g., by fluidized bed reactor Si feedstock.[6,8,11,12] This method results in a structure with grains smaller than in standard multicrystalline silicon. HPMC-Si also contains an increased number of random angle grain boundaries, in contrast to standard multicrystalline ingots that are dominated by Σ3 Coincidence Site Lattice grain boundaries. Random angle grain boundaries were shown to be more detrimental to performance than Σ3 boundaries, since they are more heavily decorated with impurities.[13–16] However, in HPMC, random angle grain boundaries offset some of their own recombination activity by annihilating dislocations.[17] This leads to increased performance in HPMC cells, when compared with the standard multicrystalline cells that contain higher densities of efficiency-limiting dislocations.[18]

The effect of defects and impurities present after crystallization on cell performance can be mitigated during cell processing through impurity gettering and defect passivation. Both grain boundaries and dislocations present in the material are less harmful when clean, but their negative effect increases with impurity decoration.[14,19] Gettering can be used to introduce

---

K. Adamczyk, Prof. M. Di Sabatino
Department of Materials Science and Engineering
NTNU, A. Getz vei 2B, NO-7491 Trondheim, Norway
E-mail: krzysztof.adamczyk@ntnu.no

Dr. R. Søndenå, Dr. C. C. You
Department for Solar Energy, IFE
NO-2007 Kjeller, Norway

Dr. G. Stokkan
Sintef Materials and Chemistry
NO-7465 Trondheim, Norway

Dr. J. Lindroos, Prof. M. Rinio
Karlstad University
651 88 Karlstad, Sweden

The ORCID identification number(s) for the author(s) of this article can be found under https://doi.org/10.1002/pssa.201700493.

DOI: 10.1002/pssa.201700493

© 2017 WILEY-VCH Verlag GmbH & Co. KGaA, Weinheim

sinks for fast diffusing metallic impurities, such as Fe, Ni, or Cu, into the noncritical parts of the device.[16,20–24] A subsequent technique in the solar cell production chain, hydrogen passivation or hydrogenation for short, passivates part of the metallic impurities and dangling bonds of the crystal lattice near structural defects, resulting in an increased minority carrier lifetime.[25–30]

Even though gettering and hydrogenation are applied in standard solar cell manufacturing, the HPMC-Si material is still limited in efficiency by defects, particularly by dislocations.[17,18] The effect of dislocations on the recombination of minority charge carriers was modeled by Donolato with a parameter describing the recombination strength γ_d, normalized to a dimensionless parameter $\Gamma = \gamma_d / D$, where D is the minority carrier diffusion coefficient.[31] γ_d is the number of recombinations per time, the dislocation length, and the excess carrier density.[32] The normalized value of this parameter G serves as a measure of the recombination strength of dislocation clusters. Rinio et al.[32] showed that the effect of dislocations on the cell efficiency depends on their spatial pattern. An interesting observation was that larger recombination strengths were typically found at dislocation clusters with random arrangement, while lower recombination activity is seen at clusters of ordered and aligned dislocations. The difference has been explained to result from different evolution and structures of the dislocations after crystal growth, with or without recovery and polygonization.[33] Polygonization, a process where dislocations arrange in low energy structures by glide and climb processes, leads to a certain degree of ordering. The tensile stress field of a dislocation aligns with the compressive stress field of its neighboring dislocation, reducing the strain. This process can be expected only at higher temperatures because it requires climb and glide. It is possible that after polygonization the dislocations have a lower gettering strength as a result of a smaller number of kinks and jogs on the dislocations in ordered structures and a weaker stress field around them, which both lead to a higher precipitate nucleation energy barrier.

The question how dislocation clusters in HPMC-Si react to gettering and hydrogenation requires further work in order to reduce their effect on device performance. This study aims to analyze this issue in terms of recombination strength in HPMC-Si. A hybrid ingot, consisting of both HPMC and quasi-mono silicon, is used to investigate this effect. The quasi-mono part serves as a reference material grown in the same crystallization process as the HPMC part, but without the effect of grain boundaries.

2. Experimental Section

2.1. Ingot Growth

A hybrid ingot with an approximate diameter of 25 cm and a weight of 15 kg was grown with a Crystalox DS 250 directional solidification furnace. Boron was added to achieve a resistivity of about 1.0–1.3 Ω cm. The ingot structure was defined by placing a seeding layer on the bottom of a high-purity quartz crucible coated with Si_3N_4. Such a crucible is normally only used for CZ growth, but it was chosen for this directional solidification experiment, in order to obtain an ingot purity comparable to the industrial quality in a pilot scale furnace.

The quasi-mono part of the ingot was seeded by placing two slabs cut from a CZ ingot in [100] orientation over one half of the crucible bottom as shown in **Figure 1**(a) and (b). The other half was filled with Fluidized Bed Reactor (FBR) granules up to the CZ slab level to seed the HPMC part. The whole crucible was filled with high purity feedstock. During the melting, a quartz rod was used to probe the solid–liquid interface to check that the seeding structure had melted only partially, allowing for seeded growth in both parts of the crucible. The result was a hybrid ingot consisting of HPMC and quasi-mono. Additional details on ingot growth can be found in Ref. [34]. After growth a slab containing the seeds, of about 3 cm thickness was cut off from the bottom of the ingot and from the remaining part a 156 × 156 mm^2 block was cut, according to the scheme in Figure 1(b). The resulting block had about 10 cm height. The block was grinded and industrially wafered into 180 μm thick hybrid wafers.

2.2. Wafer and Cell Processing

The wafers were divided into groups and processed according to the scheme in **Figure 2**. Industrial reference HPMC-Si material was added to each respective group. All groups were first damage etched in a HF:Nitric acid:Acetic acid solution (CP5) and

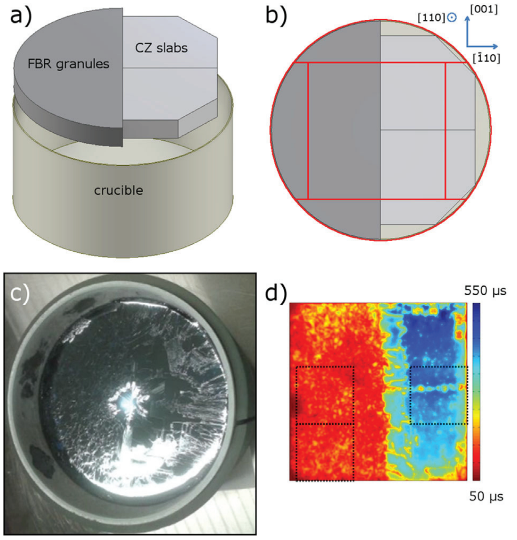

Figure 1. a) Seeding structure for the hybrid ingot. b) Top view of the seeding structure with an overlaid block cutting scheme (red lines), and the orientation of the seeding with CZ slabs. c) The grown hybrid ingot in its crucible. d) Minority carrier lifetime map (PL) of an ungettered, but surface-passivated wafer (156 × 156 mm^2) cut from the middle of the ingot. Dashed lines on the PL map show the 50 × 50 mm areas, which were cut from the full wafers and processed into HIT cells for LBIC measurements.

© 2017 WILEY-VCH Verlag GmbH & Co. KGaA, Weinheim

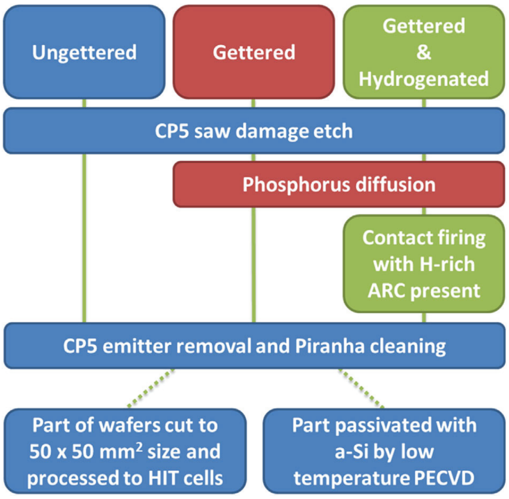
Ungettered
Gettered
Gettered & Hydrogenated
CP5 saw damage etch
Phosphorus diffusion
Contact firing with H-rich ARC present
CP5 emitter removal and Piranha cleaning
Part of wafers cut to 50 x 50 mm² size and processed to HIT cells
Part passivated with a-Si by low temperature PECVD

Figure 2. Processing steps for three groups of full (156 × 156 mm^2) hybrid wafers.

cleaned. The ungettered (U) group was only etched and cleaned after wafering. The gettered (G) group underwent a phosphorus in-diffusion process (PDG) in about 830 °C where $POCl_3$ gas was used as a phosphorus source to create a 75 Ω $sq.^{-1}$ emitter. In the third group, gettered and hydrogenated (G + H), PDG was followed by surface passivation with a hydrogen-rich SiO_xN_y/SiN_x stack layer using plasma-enhanced chemical vapor deposition (PECVD). The SiO_xN_y layer was deposited at 130 °C and capped with SiN_x deposited at 400 °C.

With layers deposited in such manner the wafers were subsequently hydrogenated through a standard high-temperature contact firing process, with a 720 °C peak temperature. Finally, all the wafers were etched in a fresh CP-5 solution to remove a layer thicker than the emitter in the G and G + H groups. Some sister wafers from all three groups were passivated on both sides with amorphous Si layers (about 40 nm thick) by PECVD at about 230 °C for lifetime measurements. Other sister wafers were cut into 50 × 50 mm^2 samples and processed further into Heterojunction with Intrinsic Thin layer solar cells (HIT)[35] for LBIC measurements. The HIT structure with its low-temperature processes (<200 °C) was chosen to prevent thermally induced changes to the bulk recombination activity in all three wafer groups. The HIT process consisted of subsequent PECVD of different layers: amorphous intrinsic Si, n-type or p-type doped amorphous Si, and indium-wolfram oxides as a transparent conducting film.[36] The a-Si layers were ≈10 nm thick, the IWO layer had about 80 nm on the front and 70 nm on the backside. The Ag contacts were printed using the same mesh on both the front and the back sides, to create overlapping contacts with minimal effect on the LBIC signal. Following electrical characterization, the HIT cells contacts were removed by etching in aqua regia at 80 °C for 2 h, followed by mechanical polishing. The polished samples were selectively etched in the Secco etchant for 60 s[37] to obtain optimal etch pit size.

2.3. Characterization

The wafer set for lifetime measurements was characterized by band-to-band photoluminescence (PL) imaging during uniform illumination with a 808 nm laser, calibrated with quasi-steady state photoconductance measurements on an LIS-R1 instrument from BTImaging.[38,39] The average minority carrier lifetime was determined at one sun light intensity corresponding to a constant carrier generation rate of 1.13E 19 cm^{-3} s^{-1}.

The HIT samples were first characterized using a custom-built LBIC system with a 826 nm laser as excitation source, with resolution of 12.5 μm and about 2 μW light power[32] to obtain maps of the internal quantum efficiency (IQE). Microscopic images were measured in an array using an automated optical microscope (Olympus MX61A) combined with the ImageJ analysis software to measure the positions of etch pits.[40] Based on this, topograms of the dislocation density with a resolution identical to the IQE topograms of the same area were calculated[41] to allow for a direct pixel by pixel comparison of EPD and IQE.[42] The carrier diffusion length and dislocation density were related by the Donolato model, with the recombination strength as a fitting parameter.[31,32] IQE was related to the carrier diffusion length in the cell through a simple PC1D model.[43] The HIT-like cells were modelled assuming a shallow emitter with about 2.9 × 10^{20} cm^{-3} peak doping on an Erfc profile and a front surface recombination velocity of 1000 cm s^{-1}. The rear surface recombination was fitted to the highest IQE values measured in the cells. Plots of IQE as a function of etch pit density were drawn and fitted with the Donolato recombination model for the analysed dislocation clusters. The recombination strength of the dislocations was extracted from curve fitting of each dislocation cluster.

The impurity content in the ingot was measured by Neutron Activation Analysis (NAA) at the Missouri University Research Reactor. A precise measurement with this technique required relatively large, roughly cubic pieces of material with a 20 mm edge. The results presented in this work come from a piece of the HPMC part of the ingot, which was cut out next to the 156 × 156 mm block at 44–66% of fraction solidified. The error of NAA for each element is given with the respective results. The segregation of impurities into the dislocation clusters was analyzed by Secondary Ion Mass Spectrometry (SIMS) on a Cameca IMS 7F measurement system. This system allowed studying the impurity content in selected circular areas with a diameter of about 60 μm. The SIMS measurement error was at its highest 10% of the measured value and it originated from an instrument error along with the uncertainty in the implanted dose of the reference sample.

3. Results and Discussion

3.1. General Trends

The average minority carrier recombination lifetimes (lifetimes for short) obtained from PL measurements and shown in **Figure 3** indicate that the QM part of the ingot has higher lifetimes than the HPMC part in all three wafer groups at all ingot heights. What can also be seen for both QM and HPMC is

© 2017 WILEY-VCH Verlag GmbH & Co. KGaA, Weinheim

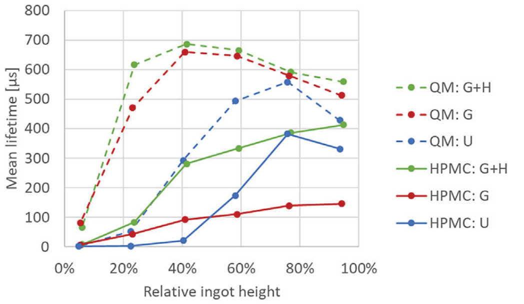

Figure 3. Average lifetimes from QSSPC calibrated PL measurements for both HPMC and Quasi Mono parts of the wafers along the ingot height.

that the bottom and top parts of the ingot show reduced lifetime values, with the lowest values in the bottom. This should be attributed to the impurity distribution in the ingot, i.e., the red zone effect related to both segregation during crystal growth, and diffusion of impurities from the crucible walls during cooling of the ingot. An interesting observation is that this effect is much stronger in the HPMC part, where a high density of defects is present, possibly allowing for faster diffusion in the ingot.[44,45]

Gettering is also less efficient in the HPMC part. In the upper part of the ingot, gettering of HPMC even results in a decrease of the mean lifetime, similar to a previous study on commercially available multicrystalline wafers.[46] It has been shown that such a deterioration of the wafers by gettering typically can take place at the extended defects. In line with recent reports an additional hydrogenation step is required to obtain an improvement to values higher than in the ungettered state in the top and middle of the ingot.[15,47,48] The situation is different in the bottom wafers, as gettering alone improves the mean lifetime, probably because of the higher initial impurity content. In the QM part, the gettering process increases the mean lifetime for each position. Hydrogenation slightly increases the mean lifetime even further. This is because the QM part of the ingot has a low density of extended defects (grain boundaries, dislocations) when compared with the HPMC part. The detailed study of how the dislocation recombination strength changes after each process step and affects the electrical performance of the device has been performed by LBIC measurements and is presented below for different ingot positions.

3.2. HPMC – Bottom of Ingot

In the bottom of the ingot, on samples from about 10% relative ingot height, dislocation clusters were too few to allow for quantification of their recombination strength. The dislocations that were available for analysis were found too close to grain boundaries, their effect on IQE was also too low to extract any data allowing a fit with the Donolato curves. The IQE maps allowing for a qualitative comparison are presented in **Figure 4**. The main observation, already mentioned, is that even with relatively large dislocation densities, about $8 \times 10^5\,\mathrm{cm}^{-2}$ in the case of the area marked in Figure 4, the effect of dislocations on the overall performance seems small when compared to the effect of grain boundaries. In the ungettered state, the IQE in high dislocation density areas is higher than in neighboring grains with dislocation densities below $10^4\,\mathrm{cm}^{-2}$. The IQE in the ungettered state is overall much smaller than after subsequent process steps. The major difference occurs in areas of low densities of extended defects, where values of about 70% are measured in the middle of the grains in the ungettered state, while in the gettered and gettered and hydrogenated the same areas show values of about 95%. This shows that PDG can be an efficient way of improving the efficiency of samples from the red zone area of the ingot.

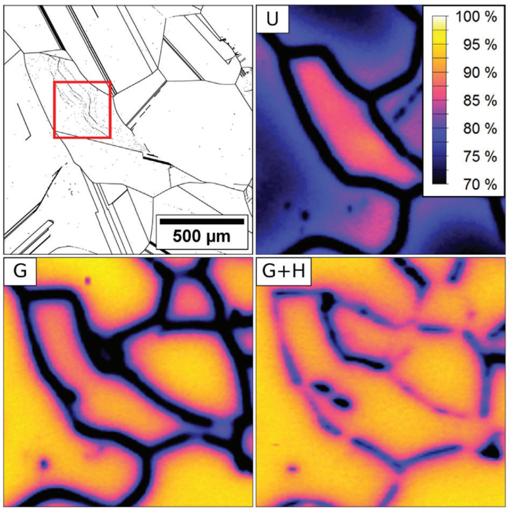

Figure 4. Micrograph of dislocation structures in the bottom of the ingot and IQE maps of the neighboring wafers after different processing. The micrograph has been processed with "make binary" and "dilute" ImageJ algorithms for presentation purposes. The dislocation density measured in the area marked with a red square is about $8 \times 10^5\,\mathrm{cm}^{-2}$.

3.3. HPMC – Middle of Ingot

The middle of the ingot contains dislocation clusters that are recombination-active enough for quantification. **Figure 5** shows the recombination strength of dislocation clusters in the middle and top of the hybrid ingot and in the middle of an industrial HPMC reference ingot. Dislocations from the HPMC part of the hybrid ingot grown in laboratory scale furnace show very similar recombination strength values to the ones observed in industrial reference.

The main trend is a considerable increase in dislocation recombination strength after gettering and a subsequent reduction by hydrogenation. This is in agreement with the lifetime measurements, where gettering causes only a relatively small improvement or even deterioration of the measured average value.

© 2017 WILEY-VCH Verlag GmbH & Co. KGaA, Weinheim

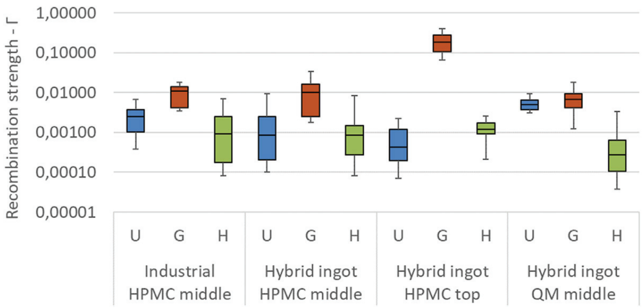

Figure 5. The recombination strength of dislocation clusters in the hydrid ingot and an industrial HPMC ingot after different processing steps. The results for different gamma values are presented in terms of a box plot: for each group the middle line is the median, the box contains 50% of the population centered on the median, and the whiskers show the upper and lower quartiles.

IQE maps of a larger dislocation structure from the middle of the ingot can be seen in **Figure 6**. These maps show that while the signal from low defect density areas is improved during gettering, with an increase from about 96 to 98%, recombination at crystal defects increases considerably. The improved performance of the hydrogenated cell can be attributed to a decrease of recombination at grain boundaries and dislocations, while maintaining the higher bulk lifetime gained during gettering. As mentioned, there is also a difference between the dislocation clusters that are visible especially after gettering but also present after other process steps. The top row of Figure 6 presents two clusters with different dislocation distributions. The cluster on the left shows a type of ordered dislocations, while the right cluster is unordered. Both of these clusters have a similar dislocation distribution on the neighboring wafers. When comparing the recombination strength of these clusters, it can be noted that after every process step, the dislocations distributed randomly show higher recombination activity, even though the dislocation density in the ordered cluster is considerably larger. This is in agreement with previous, similar work performed on standard multicrystalline silicon material.[32]

3.4. HPMC – Top of Ingot

The top part of the ingot differs from the middle in terms of much lower mean lifetime values after gettering (G), as seen in Figure 3. Nevertheless, lifetime recovery and improvement were possible through hydrogenation (G + H). This effect can also be seen in IQE maps, presented in **Figure 7**. The difference in the IQE scale should be noted, when comparing the top maps to other ingot positions. The effect of gettering on recombination activity of the defects was considerably stronger, and while values of about 70% IQE were measured on high dislocation density areas in the middle of the ingot, in the top these levels nearly reached 0%, especially in larger dislocation structures like the one visible in Figure 7. The recombination strength of dislocations in the top is similar to the middle ingot part in ungettered (U) and fully processed (G + H) states in Figure 5. In the gettered state, however, the recombination activity of dislocations is higher in the top than in the middle of the ingot.

3.5. Quasi-Mono

In the middle of the quasi-mono part, the only extended defects are dislocation clusters originating from the horizontal seed joint. These clusters are visible in the PL map in Figure 1d. **Figure 8** shows a fine resolution IQE map of this area on neighboring wafers. Dislocation structures originating at the seed junction are visible after all process steps. The low defect density areas in the ungettered sample show relatively lower IQE than in the gettered and fully processed samples. The IQE contrast and recombination strength of the dislocations is relatively high in the ungettered state, higher than in HPMC. The increase in Γ of dislocation clusters in the QM part during gettering is not as strong as in HPMC, indicating an increased efficacy of the gettering process in the QM part. This may be caused by a lower defect density in this part of the ingot, resulting in a an overall lower concentration of impurities trapped on these defects. A lower density of defects, acting as nucleation sites for precipitates during gettering, also allows for a more efficient gettering process. The precipitates present in the material before gettering can dissolve more easily, allowing also more of the impurities to diffuse to the gettering layer. This leads to a better performance after hydrogenation and lower Γ-values after full processing, even though only the unordered dislocation clusters were found in this part of the ingot. Another important factor is that during the ingot growth the

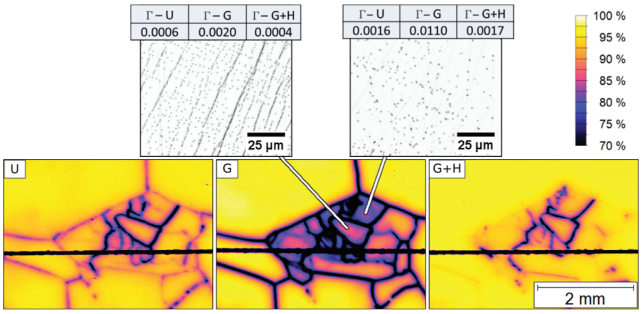

Figure 6. Bottom row – IQE maps of a high dislocation density structure on neighbouring wafers after different process steps. Top row – micrographs of selected dislocation clusters from this structure are presented along with their Γ-values. Dislocation densities for the ordered cluster on left and unordered on the right are 7×10^6 and 1×10^6 cm^{-2}, respectively.

© 2017 WILEY-VCH Verlag GmbH & Co. KGaA, Weinheim

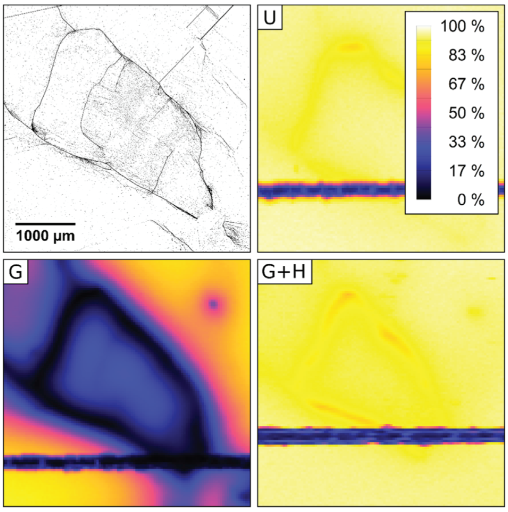

Figure 7. A binarized and diluted micrograph and IQE maps of areas on samples from neighboring wafers from the top of the ingot. A large dislocation structure can be seen in the images. The dislocation density in the middle of the visible grain reached 4 × 10^6 cm^{-2}. Note the differences in the IQE scale when compared to other maps presented in this work.

incorporation of impurities in the QM part is probably slower than in the HPMC part due to the differing defect densities. Such a factor would affect both the performance of the ungettered samples, as well as the IQE/lifetime levels after gettering.

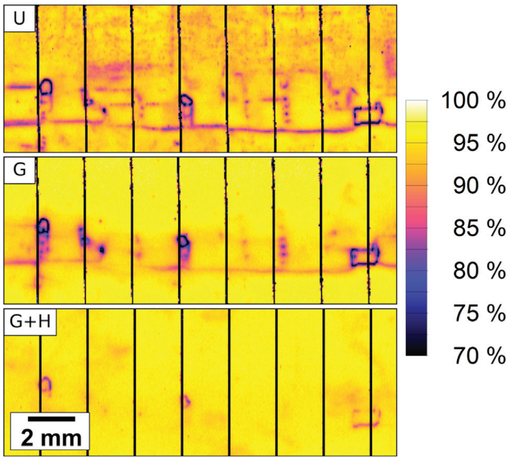

Figure 8. IQE maps of areas on samples from neighboring wafers from the QM part from the middle of the ingot. Dislocation structures originating at the seed joint are visible along a horizontal line in the middle of the maps.

Table 1. Impurity concentrations found in the ingot by NAA. Given in atoms cm^{-3}.

Co	Cr	Ni	Zn
$2.2 \pm 2 \times 10^{10}$	$2.6 \pm 0.04 \times 10^{12}$	$2.3 \pm 0.08 \times 10^{13}$	$2.8 \pm 0.4 \times 10^{11}$

3.6. Impurity Concentration

Since impurity decoration is known to determine the dislocation recombination strength after various process steps, their concentration in the material and segregation to defects was assessed with NAA and SIMS. The mean concentration of impurities in the ungettered material was measured with NAA on a large, 20 × 20 × 20 mm^3 sample. It revealed that the ingot was relatively pure. The only transition metals found in concentrations above the detection limit are listed in **Table 1**. **Table 2** presents the detection limits of other expected impurities.

While NAA only detected the mean impurity concentrations in relatively large volumes of the unprocessed wafers, SIMS was used to measure the impurity concentration in and the impurity segregation toward dislocation clusters, enclosed within a sputtered area of about 60 μm in diameter. Ungettered and gettered samples were analyzed by SIMS, but only Ni was detected due to poor detection limits. Changes in impurity distribution during hydrogenation by firing were not expected to be large enough to allow for detection. **Figure 9** shows the Ni concentration per cluster along with two depth profiles on one of the analyzed clusters. In the ungettered middle of the ingot, a clear difference is seen between the mean Ni bulk concentration of $2.3 \pm 0.08 \times 10^{13}$ atoms cm^{-3} (NAA) and the Ni concentration in the dislocation clusters in the order of 10^{16} atoms/cm^3 measured by SIMS. This indicates a strong impurity gettering of fast-diffusing Ni[49] from the bulk towards the dislocations, during the ingot cooling. Even though interstitial Ni is harmless, it is unstable and prefers to precipitate at extended defects, forming recombination-active $NiSi^2$.[50] After PDG, the Ni concentration is even higher in the dislocation clusters, showing strong collection of Ni to the dislocations during PDG. Therefore, increased Ni precipitation might explain the increase in the recombination strength of the dislocation clusters after gettering in Figure 5. Nickel precipitates can also be readily passivated by hydrogen, which could partly explain the decreased recombination activity after gettering and hydrogenation.[51] In the ingot top, the Ni concentration at the dislocations in the ungettered state is relatively larger than in the middle. We can probably assume that also other harmful elements like Fe should be present in higher, but still undetectable concentrations. In the case of the top samples, impurities could then diffuse to the dislocations from a smaller volume and still affect their

Table 2. Detection limits of impurities not found by NAA. Given in atoms cm^{-3}.

Fe	Cu	K	Ti	Mo
2.3×10^{12}	7.1×10^{12}	5.5×10^{12}	6.7×10^{14}	4.4×10^{11}

© 2017 WILEY-VCH Verlag GmbH & Co. KGaA, Weinheim

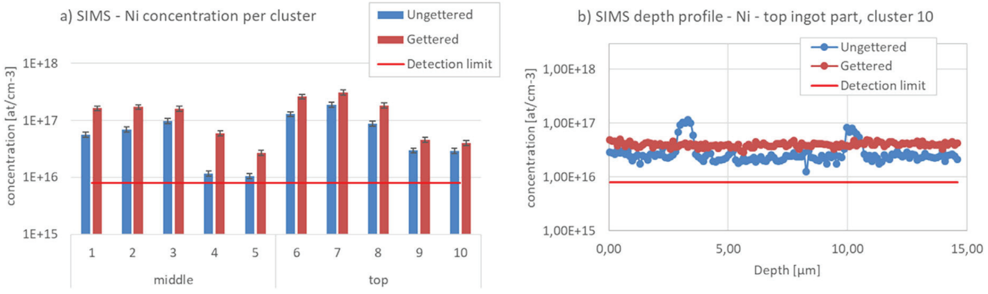

Figure 9. SIMS measurement results. a) Nickel concentration at dislocation clusters, numbered from 1 to 10, in the middle and the top samples. b) Nickel depth profiles in a cluster in top of the ingot. For the remaining analysed cases, the depth profiles were flat like the ungettered profile, only on levels presented in (a).

recombination strength. Considering this, elements diffusing in silicon slower than Ni could be the reason for the very high recombination strength of dislocations in the gettered samples in the top of the ingot. Another possible explanation of the increase of recombination strength during the gettering process is a change in the precipitate distribution.[50] The depth profiles of Ni presented in Figure 9 indicate this. Two peaks were found in the depth profile of one of the clusters with higher recombination strength, each about 0.8 µm wide. They possibly came from large precipitates or precipitate agglomerates on this cluster. A lack of similar peaks in the profile from the gettered sample might mean that while the impurity content was similar, the size of precipitates at these dislocations was different, leading to different recombination mechanisms and differences in recombination strength. Such explanation is based only on a profile obtained from 1 out of 10 analyzed dislocation clusters. If a change in precipitate distribution occurred on the other clusters as well, it was not detected.

The SIMS measurements aimed also at analyzing the ordered and disordered dislocation clusters in terms of impurity concentration, but no significant differences were found.

4. Conclusions

Overall the recombination strength of dislocations Γ is increased by an order of magnitude during the gettering process, often leading to a decreased material performance in the gettered state. Subsequent hydrogenation reduces the recombination strength to levels lower than in the ungettered state. Both processes are necessary to obtain optimal device performance.

In the bottom of the ingot there are few dislocation clusters and their recombination activity is affecting the material performance much less than grain boundaries. The dislocations and the effect of thermal processing on these are largely negligible in the bottom wafers.

Dislocations are present in higher densities in the middle and top of the ingot. A difference in recombination strength between unordered and ordered dislocation clusters was found, where the unordered clusters exhibit higher Γ values.

While such difference has been previously shown in standard mc-Si, this work shows that it also exists in HPMC-Si. There are various explanations for this effect, but they highlight the possible difference in impurity segregation toward ordered and unordered dislocations.

The effect of segregation plays an important role in defining the recombination activity, which could explain the difference in recombination strength between the gettered clusters in QM and HPMC parts. The decreased density of internal gettering sites in the QM might result in a larger amount of impurities being internally gettered to dislocations, and thus in a higher recombination strength of dislocations in this part of the ingot.

The role of impurity segregation and precipitate distribution for device performance is confirmed by the SIMS measurements of impurity concentration at different dislocation clusters.

Acknowledgments

The work reported in this paper was performed in the project Impurity Control in High Performance Multicrystalline Silicon, 228930/E20, funded by the Norwegian Research Council's ENERGIX programme and industry partners REC Solar, REC Silicon, Steuler Solar and The Quartz Corp. Part of this work was also supported by the SOPHIA project "HPSS," the Solar-Era.Net project "HighCast" via the Swedish Energy Agency, and the project "Advanced analysis of industrial silicon wafers for solar cells" by J. Gust. Richert stiftelse, which is gratefully acknowledged.

Conflict of Interest

The authors declare no conflict of interest.

Keywords

dislocations, gettering, hydrogenation, silicon, solar cells

Received: July 17, 2017
Revised: September 14, 2017
Published online: November 7, 2017

---

[1] Fraunhofer Institute for Solar Energy Systems, Photovoltaics Report, **2016**.

© 2017 WILEY-VCH Verlag GmbH & Co. KGaA, Weinheim

[2] Fraunhofer Institute for Solar Energy Systems, Photovoltaics Report, **2017**.
[3] L. Arnberg, M. Di Sabatino, E. J. Øvrelid, *J. Cryst. Growth* **2012**, *360*, 56.
[4] L. Arnberg, M. Di Sabatino, E. Øvrelid, *Transact. Indian Inst. Metal* **2012**, *65*, 509.
[5] M. Di Sabatino, G. Stokkan, *Phys. Status Solidi (A)* **2013**, *210*, 641.
[6] G. Stokkan, A. Ciftja, *SINTEF Mater. Chem*. **2014**.
[7] N. Stoddard, B. Wu, I. Witting, M. C. Wagener, Y. Park, G. A. Rozgonyi, R. Clark, *Solid State Phenom*. **2008**, *131–133*, 1.
[8] C. W. Lan, A. Lan, C. F. Yang, H. P. Hsu, M. Yang, A. Yu, B. Hsu, W. C. Hsu, A. Yang, *J. Cryst. Growth* **2016**, *468*, 17.
[9] M. Trempa, C. Reimann, J. Friedrich, G. Müller, D. Oriwol, *J. Cryst. Growth* **2012**, *351*, 131.
[10] K. E. Ekstrøm, G. Stokkan, R. Søndenå, H. Dalaker, T. Lehmann, L. Arnberg, M. Di Sabatino, *Phys. Status Solidi (A)* **2015**, *212*, 2278.
[11] C. W. Lan, W. C. Lan, T. F. Lee, A. Yu, Y. M. Yang, W. C. Hsu, B. Hsu, A. Yang, *J. Cryst. Growth* **2012**, *360*, 68.
[12] K. E. Ekstrøm, G. Stokkan, A. Autruffe, R. Søndenå, H. Dalaker, L. Arnberg, M. Di Sabatino, *J. Cryst. Growth* **2016**, *441*, 95.
[13] J. Chen, T. Sekiguchi, D. Yang, F. Yin, K. Kido, S. Tsurekawa, *J. Appl. Phys*. **2004**, *96*, 5490.
[14] J. Chen, T. Sekiguchi, *Jap. J. Appl. Phys*. **2007**, *46*, 6489.
[15] K. Adamczyk, R. Søndenå, M. Mhamdi, A. Autruffe, G. Stokkan, M. Di Sabatino, *Phys. Status Solidi (C)* **2016**, *13*, 812.
[16] M. S. Wiig, K. Adamczyk, H. Haug, K. E. Ekstrøm, R. Søndenå, *Energy Procedia* **2016**, *92*, 886.
[17] G. Stokkan, Y. Hu, Ø. Mjøs, M. Juel, *Sol. Energy Mater. Sol. Cells* **2014**, *130*, 679.
[18] S. Castellanos, K. E. Ekstrom, A. Autruffe, M. A. Jensen, A. E. Morishige, J. Hofstetter, P. Yen, B. Lai, G. Stokkan, C. del Canizo, T. Buonassisi, *IEEE J. Photovolt*. **2016**, *6*, 632.
[19] D. B. Holt, B. G. Yacobi, *The Electrical, Optical and Device Effects of Dislocations and Grain Boundaries, Extended Defects in Semiconductors – Electronic Properties, Device Effects and Structures*, Cambridge University Press, Cambridge **2007**.
[20] S. M. Myers, M. Seibt, W. Schröter, *J. Appl. Phys*. **2000**, *88*, 3795.
[21] A. Bentzen, Phosphorus diffusion and gettering in silicon solar cells, Phd thesis. Department of Physics, University of Oslo, Oslo, Norway, **2006**.
[22] A. Bentzen, A. Holt, R. Kopecek, G. Stokkan, J. S. Christensen, B. G. Svensson, *J. Appl. Phys*. **2006**, *99*, 093509.
[23] D. Macdonald, A. Cuevas, F. Ferrazza, *Solid-State Electron*. **1999**, *43*, 575.
[24] T. Buonassisi, A. A. Istratov, S. Peters, C. Ballif, J. Isenberg, S. Riepe, W. Warta, R. Schindler, G. Willeke, Z. Cai, B. Lai, E. R. Weber, *Appl. Phys. Lett*. **2005**, *87*, 121918.
[25] B. Sopori, *J. Electron. Mater*. **2002**, *31*, 972.
[26] B. J. Hallam, P. G. Hamer, S. Wang, L. Song, N. Nampalli, M. D. Abbott, C. E. Chan, D. Lu, A. M. Wenham, L. Mai, N. Borojevic, A. Li, D. Chen, M. Y. Kim, A. Azmi, S. Wenham, *Energy Procedia* **2015**, *77*, 799.
[27] N. H. Nickel, N. M. Johnson, W. B. Jackson, *Appl. Phys. Lett*. **1993**, *62*, 3285.
[28] S. Leonard, V. P. Markevich, A. R. Peaker, B. Hamilton, *Appl. Phys. Lett*. **2013**, *103*, 132103.
[29] J. Szlufcik, S. Sivoththaman, J. F. Nlis, R. P. Mertens, R. Van Overstraeten, *Proc. IEEE* **1997**, *85*.
[30] X. Cheng, H. Haug, M. Di Sabatino, J. Zhu, E. S. Marstein, *IEEE J. Photovolt*. **2016**, *6*, 1103.
[31] C. Donolato, *J. Appl. Phys*. **1998**, *84*, 2656.
[32] M. Rinio, A. Yodyungyong, S. Keipert-Colberg, D. Borchert, A. Montesdeoca-Santana, *Phys. Status Solidi A* **2011**, *208*, 760.
[33] S. Castellanos, M. Kivambe, J. Hofstetter, M. Rinio, B. Lai, T. Buonassisi, *J. Appl. Phys*. **2014**, *115*.
[34] G. Stokkan, D. S. Marisa, R. Søndenå, M. Juel, A. Autruffe, K. Adamczyk, H. V. Skarstad, K. E. Ekstrøm, M. S. Wiig, C. C. You, H. Haug, M. M'Hamdi, *Phys. Status Solidi (A)* **2017**, *214*, 1700319.
[35] M. Taguchi, A. Terakawa, E. Maruyama, M. Tanaka, *Progr. Photovolt.: Res. Appl*. **2005**, *13*, 481.
[36] Z. Lu, F. Meng, Y. Cui, J. Shi, Z. Feng, Z. Liu, *J. Phys. D: Appl. Phys*. **2013**, *46*, 075103.
[37] F. Secco d'Aragona, *J. Electrochem. Soc* **1972**, *119*, 948.
[38] T. Trupke, R. A. Bardos, M. C. Schubert, W. Warta, *Appl. Phys. Lett*. **2006**, *89*, 044107.
[39] S. Herlufsen, J. Schmidt, D. Hinken, K. Bothe, R. Brendel, *Phys. Status Solidi RRL* **2008**, *2*, 245.
[40] C. A. Schneider, W. S. Rasband, K. W. Eliceiri, *Nature Methods* **2012**, *9*, 671.
[41] M. Rinio, S. Peters, M. Werner, A. Lawerenz, H. J. Möller, *Solid State Phenom*. **2002**, *82–84*, 701.
[42] M. Rinio, A. Hauser, H. J. Möller, Topography correlation – a powerful tool applied to the visualisation of remote plasma hydrogen passivation effects, 3rd World Conference on Photovoltaic Energy Conversion, IEEE, Osaka, Japan, **2003**.
[43] P. A. Basore, D. A. Clugston, PC1D version 5: 32-bit solar cell modeling on personal computers, Twenty-Sixth IEEE Photovoltaic Specialists Conference, IEEE, Anaheim, CA, USA, **1997**.
[44] J. Pelleg, *Diffusion in Dislocations, Diffusion in Ceramics*, Springer International Publishing, Cham **2016**, pp. 87–94.
[45] J. Pelleg, *Diffusion in Grain Boundaries, Diffusion in Ceramics*, Springer International Publishing, Cham **2016**, pp. 75–86.
[46] R. Søndena, J. Gjessing, H. Angelskår, Ø. Nordseth, S. E. Foss, E. S. Marstein, Effect of dislocations on the electrical response of multicrystalline silicon solar cells, European Photovoltaic Solar Energy Conference and Exhibition, EU PVSEC Proceedings, Paris, **2013**, pp. 872–876.
[47] H. C. Sio, S. P. Phang, T. Truppke, D. Macdonald, *IEEE J. Photovolt*. **2015**, *5*, 1357.
[48] M. Rinio, E. Zippel, D. Borchert, Spatial redistribution of recombination centres by the solar cell process, 20th European Photovoltaic Solar Energy Conference, Barcelona, **2005**.
[49] J. Lindroos, D. P. Fenning, D. J. Backlund, E. Verlage, A. Gorgulla, S. K. Estreicher, H. Savin, T. Buonassisi, *J. Appl. Phys*. **2013**, *113*, 204906.
[50] M. Seibt, R. Khalil, V. Kveder, W. Schröter, *Appl. Phys. A* **2008**, *96*, 235.
[51] M. V. Trushin, O. F. Vyvyenko, M. Seibt, *Solid State Phenom*. **2007**, *131–133*, 155.

© 2017 WILEY-VCH Verlag GmbH & Co. KGaA, Weinheim

Article IV:

Recombination activity of grain boundaries in high-performance multicrystalline Si during solar cell processing

K. Adamczyk, R. Søndenå, G. Stokkan, E. Looney, M. Jensen, B. Lai, M. Rinio, M. Di Sabatino, 2018, Journal of Applied Physics, vol. 123, issue 5, p. 055705

Paper IV

JOURNAL OF APPLIED PHYSICS **123**, 055705 (2018)

Recombination activity of grain boundaries in high-performance multicrystalline Si during solar cell processing

Krzysztof Adamczyk,[1,a)] Rune Søndenå,[2] Gaute Stokkan,[3] Erin Looney,[4] Mallory Jensen,[4]
Barry Lai,[5] Markus Rinio,[6] and Marisa Di Sabatino[1]
[1]*Department of Materials Science and Engineering, NTNU, A. Getz vei 2B, NO-7491 Trondheim, Norway*
[2]*Department for Solar Energy, IFE, NO-2007 Kjeller, Norway*
[3]*SINTEF Materials and Chemistry, NO-7465 Trondheim, Norway*
[4]*Massachusetts Institute of Technology, Cambridge, Massachusetts 02139, USA*
[5]*Advanced Photon Source, Argonne National Laboratory, Lemont, Illinois 60439, USA*
[6]*Karlstad University, 651 88 Karlstad, Sweden*

(Received 9 December 2017; accepted 24 January 2018; published online 7 February 2018)

In this work, we applied internal quantum efficiency mapping to study the recombination activity of grain boundaries in High Performance Multicrystalline Silicon under different processing conditions. Wafers were divided into groups and underwent different thermal processing, consisting of phosphorus diffusion gettering and surface passivation with hydrogen rich layers. After these thermal treatments, wafers were processed into heterojunction with intrinsic thin layer solar cells. Light Beam Induced Current and Electron Backscatter Diffraction were applied to analyse the influence of thermal treatment during standard solar cell processing on different types of grain boundaries. The results show that after cell processing, most random-angle grain boundaries in the material are well passivated, but small-angle grain boundaries are not well passivated. Special cases of coincidence site lattice grain boundaries with high recombination activity are also found. Based on micro-X-ray fluorescence measurements, a change in the contamination level is suggested as the reason behind their increased activity. *Published by AIP Publishing.*
https://doi.org/10.1063/1.5018797

I. INTRODUCTION

With multicrystalline silicon being the dominant material used for solar cells, the mechanisms of how crystalline defects affect final device performance require more attention.[1,2] It is established that both dislocations and grain boundaries are detrimental in this regard[3–6] due to the interactions between these structural defects and impurities introduced to the material at various processing stages.[3,7] It was reported that the increased recombination strength of dislocations during solar cell processing can be related to a change in precipitate distribution.[8] In the so-called High Performance Multicrystalline (HPMC) silicon, material grain boundaries are an important part of the structure. Traditionally, grain boundaries were considered as harmful to device performance, and crystal growth processes were optimized to obtain large grains with small grain boundary densities. Recently, it was discovered that decreasing the grain size while maintaining a structure where random-angle grain boundaries (RAGBs) were prevalent led to increased cell efficiency.[9–11] RA grain boundaries allow a better relaxation of thermal stress, acting as sinks for recombination active dislocations. The second type of grain boundaries most often found in HPMC Si are the Coincidence Site Lattice (CSL) grain boundaries with $\Sigma3$ index of coincidence.[11] Most of the $\Sigma3$ grain boundaries are coherent twin boundaries, meaning that the interface plane has the same orientation of the $\{111\}$ type in the two adjacent grains.[12] Grain boundaries, where the grains still have a CSL orientation relative to each other but where the boundary plane is random, can also occur. Because of the orientation of the plane in such cases, the resulting boundary often consists of small facets coherent on their own. Some cases of such $\Sigma3$ grain boundaries consist of facets with $\{111\}$ and $\{112\}$ orientations, and the $\{112\}$ facets introduce a lattice mismatch relaxed by an extended bond of a silicon atom with 5-fold-coordination.[13] Cases of macroscopically incoherent $\Sigma3$ grain boundary planes with a random plane orientation but microscopically coherent $\{111\}$ and $\{112\}$ facets with a neighboring array of dislocations were also found.[14] Small-angle grain boundaries (SAGBs), i.e., grain boundaries with their misorientation angle below 15°, can be also found in the material. This type of grain boundary is structurally equivalent to a line of densely packed dislocations. According to Chen and Sekiguchi, this type of grain boundary is the most detrimental to the electrical performance.[15]

The focus of this work is to study the different types of grain boundaries in HPMC Si and to quantify the effects of different thermal processes in standard solar cell manufacturing on the recombination activity at these grain boundaries, in order to better understand how they affect the final cell efficiency.

II. EXPERIMENTAL METHODS

A. Growth and processing

The material used in this study comes from a hybrid ingot consisting of half HPMC and half Quasi-Mono (QM) material. The ingot has been grown in a Crystalox DS 250

[a)] Author to whom correspondence should be addressed: krzysztof.adamczyk@ntnu.no. Telephone: +47 415 419 94.

furnace with a specific seeding structure allowing for simultaneous growth of HPMC and quasi-mono in one ingot. A high purity crucible was used to obtain purity in the ingot grown in a pilot scale furnace comparable with industrially grown ingots. A detailed description of the seeding structure can be found elsewhere.[8,16] More information about wafer processing and sample preparation can also be found therein, but the basic details are presented below.

The ingot was cut into a block, ground, and industrially wafered into full size ($156 \times 156\,\mathrm{mm}^2$) wafers about 180 μm thick. The wafers were then damage etched. The first group consists of ungettered (U) wafers. The second group of wafers (G) was gettered by phosphorus in-diffusion at 830 °C with $\mathrm{POCl_3}$ gas for 60 min followed by an emitter etch-back. The third group of wafers was gettered and subsequently hydrogenated through a simulated contact firing process with a hydrogen rich anti-reflection coating present prior to the emitter etch-back. This last group, after phosphorus diffusion gettering and a standard high temperature contact firing process with a peak temperature of 720 °C, constituted the gettered and hydrogenated group (G + H). All wafers were then surface passivated using PECVD deposition of hydrogenated amorphous silicon. The groups consisted of neighboring wafers; thus, for each position in the ingot, the same grain boundaries were compared after different processing steps.

Processed wafers were cut into $50\,\mathrm{mm} \times 50\,\mathrm{mm}$ samples and processed further into Heterojunction with Intrinsic Thin layer solar cells (HIT).[17] The cell structure enabled Light Beam Induced Current (LBIC) measurements, and the HIT structure was chosen to avoid thermally induced changes to the bulk recombination activity thanks to the low processing temperatures (less than 200 °C). Following electrical characterization, the cell structure was removed by etching in *aqua regia* at 80 °C for 2 h. Samples were then mechanically polished to enable Electron Backscatter Diffraction (EBSD) analysis of grain boundaries. Finally, $10\,\mathrm{mm} \times 10\,\mathrm{mm}$ samples were cut from several samples for Micro-X-Ray Fluorescence (μ-XRF) to analyse the precipitate distribution in selected areas.

B. Characterization

The main purpose of this work was to quantify the recombination activity of specific grain boundaries at different processing steps. To this end, LBIC was chosen as a technique to map the internal quantum efficiency (IQE) at grain boundaries with sufficient spatial resolution. The measurements of HIT cells made on the analysed wafers were performed using a custom-built LBIC system with an 826 nm laser as an excitation source. The spatial resolution used was about 12.5 μm under about 2 μW light power.[3,18] The recombination activity at grain boundaries has been quantified using IQE contrast, according to the formula presented and used by Chen and Sekiguchi[15]

$$IQE_c = \frac{I_b - I_g}{I_b}, \tag{1}$$

where I_b is the IQE of the background and I_g the IQE at the grain boundary.

After LBIC characterization, samples were prepared for EBSD measurements and analysed with a Nordif EBSD detector mounted on a Jeol JSM 840 microscope. The grain boundary type information was extracted from the resulting data using the "EDAX OIM Analysis" software. The restrictive Palumbo criterion was used to classify CSL grain boundaries.[19,20] The resulting grain boundary maps and IQE maps were manually matched.

Spatially resolved μ-XRF measurements were used to map metal distributions at grain boundaries in selected samples. These measurements were performed at beamline 2-ID-D at the Advanced Photon Source, using a 200 nm beam spot size and 220 nm steps to scan areas of about 225 $\mu\mathrm{m}^2$ and 400 $\mu\mathrm{m}^2$.[21]

III. RESULTS AND DISCUSSION

The result presentation is divided into the bottom part of the ingot, and middle and top parts, as the grain boundaries in the bottom showed different electrical activities during processing, most probably because of a difference in the initial impurity concentration. There was also a difference between the wafers coming from the middle and top of the ingot, in that the grain boundaries in wafers from the top showed a stronger IQE contrast after gettering, but since the changes in contrast during processing and the characteristics of the fully processed, G + H group from the top were similar to what was observed in the middle, they are discussed in one section.

A. Bottom of the ingot

Grain boundaries affect the IQE strongly in this part of the ingot, as the grain size is smaller, meaning a larger grain boundary density. Figure 1 shows a representative sample area analyzed by IQE after different processing steps and a corresponding EBSD map. These results suggest that at the bottom of the ingot, the recombination active grain boundaries are mostly of the RA and SA type, with CSL grain boundaries showing recombination activity less frequently.

The ungettered state shows a much lower overall performance on samples from the bottom of the ingot. The IQE map reveals zones near grain boundaries with increased efficiency. The intragrain IQE is at levels of 60%–70%, and at the grain boundaries it is lower, down to 40%–50%, but there is a zone up to about 100–150 μm from the grain boundary where the IQE increases even up to 80%. These zones with increased IQE can be explained based on an assumption that the overall poor performance of the ungettered samples is caused by an increased impurity concentration in this part of the ingot.[22,23] The zone with increased IQE values would then be an area depleted of impurities through internal gettering and precipitation on grain boundaries, so-called "denuded zones."[24] A detailed analysis of such denuded zones was performed by Autruffe *et al.*[20] An important conclusion from their work, relevant to the results presented here, is that precipitates in HPMC Si, in the absence of dislocation clusters, form rather on sparse intra-granular dislocations than on grain boundaries. Additionally, the low dislocation densities in the material lead to a higher interstitial iron concentration after solidification,

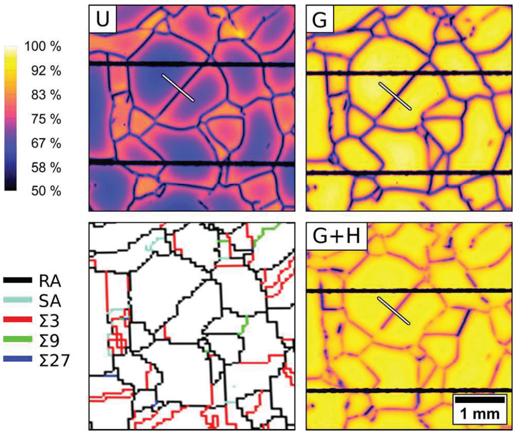

FIG. 1. Representative IQE maps from the bottom of the ingot after different processing steps, compared to EBSD of the gettered sample (lower left). The black, horizontal lines in the IQE maps are the contact fingers. The white line in the IQE maps shows the position of the linescans discussed in Fig. 2.

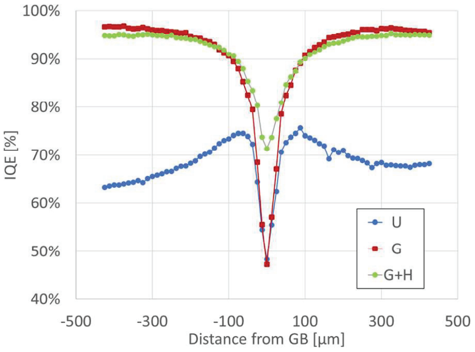

FIG. 2. IQE profiles over the random-grain boundary marked with a white line in Fig. 1 from the bottom of the ingot after different processing steps. No improvement in the IQE at the grain boundary is observed from gettering.

because there are less nucleation sites present. These conclusions are directly comparable with the material from the bottom of the ingot presented here in the ungettered state. While lower IQE levels can be found directly on grain boundaries, cells made from such a material are mostly limited by the low intragrain IQE. According to Autruffe *et al.*, this would be caused by precipitation on the intragrain dislocations and by interstitial iron present in the intragrain areas of higher concentration than in the denuded zones close to grain boundaries.

Phosphorus diffusion gettering improves the overall IQE considerably but mainly through changing the impurity concentration in the bulk. This can be seen both in Fig. 1 and when comparing the profiles in Fig. 2. Only the intragrain IQE is increased; the IQE measured at the grain boundary remains at levels of about 50%, giving a stronger grain boundary contrast. The internal gettering occurring at grain boundaries is probably stronger than on the sparse intragrain dislocations. The grain boundaries, with a similar IQE as in the ungettered state but with a higher bulk IQE, show a stronger contrast and indicate that in the absence of dislocation clusters, the impurities that are not extracted to the emitter by PDG most probably diffuse and decorate the random-angle and small-angle grain boundaries during the gettering process.

The majority of grain boundaries are passivated during the process of firing with deposited hydrogen-rich layers. As the profiles in Fig. 2 indicate, the IQE contrast on grain boundaries is reduced during firing by reducing their recombination activity, but the high intragrain IQE is not changed. The IQE maps indicate, however, that some grain boundaries are not passivated well. An analysis of the IQE contrast value for 100 randomly chosen grain boundaries showed that their distribution is indeed bimodal. The majority of the active grain boundaries shows a reduction in contrast during hydrogenation. This majority is dominated by random-angle grain boundaries. About 20% of the analysed active boundaries have a contrast similar to that in the gettered state. In this group, small-angle grain boundaries are the most frequent, but other types, including CSL, can also be found.

The analysis of dislocation clusters in the material and their recombination strength indicates that in the bottom of the ingot, their effect is much smaller than in the middle or top because of their much lower densities and a lack of larger dislocation clusters and very few areas with dislocation densities above $10^5\,\mathrm{cm}^{-2}$.[8] The effect of grain boundaries discussed above dominates in the bottom of the ingot.

B. Middle of the ingot

The middle part of the ingot, from which most commercial cells are made, is more important from an industrial point of view and as such is analysed in more detail. An overview of the sample response to the studied processes can be found in Fig. 3. When compared to the bottom part of the ingot, the material in the middle performs better and the IQE maps indicate that the concentration of impurities in the middle is lower. This can be seen especially in the ungettered state, where the middle of the ingot performs much better due to a higher intragrain IQE, indicating a lower intragrain impurity content. The grain boundary profile visible in Fig. 4 also shows that there are no depletion zones near the boundaries.

Such a material results in higher IQE values in the intragrain areas, where after gettering, values up to 98% could be measured, compared to 95%–96% in the grains in the bottom part. The grain boundaries, however, show very similar profiles after gettering in both these ingot positions, with IQE values at the boundary down to about 50%. Gettering clearly increases the grain boundary recombination rates. The most interesting difference is after hydrogenation, in the fully processed state. When comparing the IQE and EBSD maps, it can be seen that while in the ungettered and gettered samples, recombination occurs mostly at random-angle grain boundaries, but in the fully processed state, more than 90% of active GBs become well passivated and electrically inactive, with an IQE contrast below 3%. This means that random-angle grain boundaries, which are believed to be highly detrimental to performance of cells made from

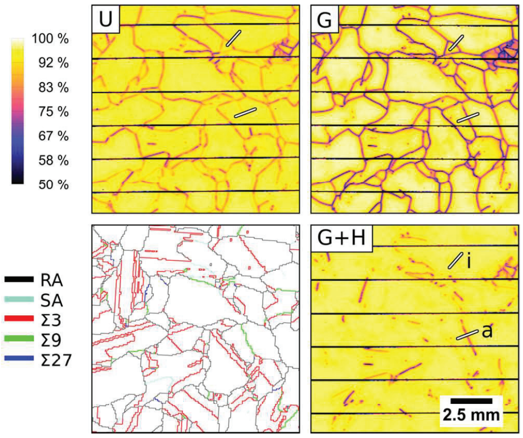

FIG. 3. IQE maps of the analysed samples from the middle of the ingot after different processing steps. The map in the lower left corner shows the different types of grain boundaries as measured by EBSD on the gettered sample. The black, horizontal lines in the IQE maps are the contact fingers. The white lines on the IQE maps mark the profiles over which the linescans of an active and inactive GB were taken.

multicrystalline silicon,[5] are very well passivated in standard processing in HPMC.

What remains active are mostly small-angle boundaries as well as a small section of random-angle grain boundaries. Parts of Σ3, Σ9, and Σ27 CSL boundaries also remain active. Figure 4 shows two profiles. One is from a random-angle grain boundary representing the well passivated grain boundaries and the other is from a Σ27 GB segment, one of the highly active in the final state.

Like most grain boundaries in the material, the "inactive" GB has its contrast, and thus recombination activity, increased during gettering. The contrast increases from 17% in the ungettered state to 32% after gettering. After hydrogenation, it is reduced to very low levels, about 2%, having a relatively small effect on IQE. The activity of the "active" grain boundary is also increased during gettering, but here, the increase is stronger, from an IQE contrast of 5% to 39%. The main difference is that hydrogen passivation reduces the contrast only slightly, down to 27%. The GB is still visible on the map and acts as a recombination site, affecting the overall IQE of the device.

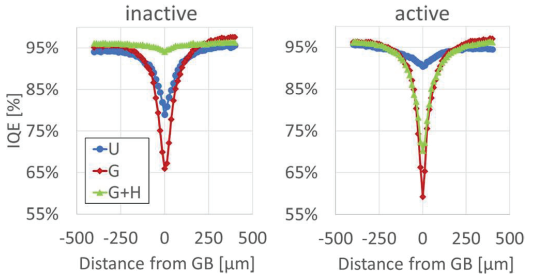

FIG. 4. IQE grain boundary profiles from samples from the middle of the ingot after different processing steps. The lines over which the linescans were taken are shown in Fig. 3. The inactive grain boundary is of random type, and the active grain boundary is of Σ27 CSL type.

An overview of the active grain boundary length and the average IQE contrast of different grain boundary types is presented in Fig. 5, and additional details can be found in Table I. The classification is based on defining the active grain boundaries as having an IQE contrast at or above 5% and those with contrast below as well passivated and inactive. The average IQE contrast for a given grain boundary type is a weighted arithmetic mean of the contrast with the active segment length of this type as weight. While many random-angle grain boundary segments are still recombination active, they are only a small fraction of all the RAGBs detected in the material and their activity, and thus, the effect on cell performance is smaller than that of small-angle grain boundaries. Most of the active grain boundary segments show a similar IQE contrast, but the active Σ27 segments show higher contrast values, about 33%, which is twice the average contrast of RAGBs, and more than half of Σ27 grain boundaries remains active after full processing. Cases of Σ27 grain boundaries emitting dislocations have been presented in the literature, and this can explain the higher recombination activity at boundaries of this type.[25] Additionally, more recombination active grain boundary segments were classified as SAGBs than were actually measured with EBSD. This is because the measurement system used in this study did not allow for precise detection of SAGB with the misorientation angle below 5°. When a recombination active boundary segment was found in the IQE maps but could not be matched with a boundary measured by EBSD, it was classified as SAGB. An example of this is the dislocation cluster visible as an area with a higher density of recombination active grain boundaries near the right, upper corner of each IQE map in Fig. 3. This dislocation cluster is "contained" within a grain bounded by RAGB and CSL boundaries visible on the EBSD map, but no SAGB are detected within. Selective etching performed on these samples revealed a complex dislocation structure, consisting of a network of unindexed grain boundaries and etch pits from dislocations in their vicinity.[8]

As mentioned, special cases of CSL grain boundaries can also be found among the recombination active grain boundaries. The fraction of boundary type that remains active in

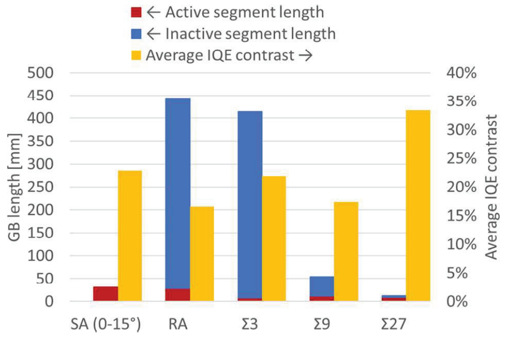

FIG. 5. Sum of active and inactive GB segment lengths for each type and average IQE contrast of the active segments. Active segments are defined as showing an IQE contrast equal to or above 5%. The arrows in the chart legend indicate the respective axis for each dataset. The analysis was performed on an area of 375 mm^2, of which part is visible in Fig. 3.

TABLE I. Fraction of remaining active boundaries of each type in the total length of all active boundary segments and fraction of active boundaries for each type in the total length of grain boundaries measured with EBSD for this type. *—active GB segments visible on the IQE maps which were not found with EBSD were classified as SAGB, and thus, more active SAGB were found on IQE maps than measured with EBSD.

Remaining active boundaries	Fraction of remaining active boundaries	Fraction of this boundary type that remain active
SAGB	36%	>100% *
RAGB	32%	6%
$\Sigma3$	9%	2%
$\Sigma9$	14%	22%
$\Sigma27$	10%	65%

Table I shows that for CSL grain boundaries, the higher the coincidence index is, the larger the fraction of grain boundaries remains active, which is in agreement with other results reported in the literature.[5,7,26] These results are similar to the case for the bimodal contrast distribution in the bottom of the ingot and can be probably explained with the difference in coherence of the grain boundaries. The recombination active segments, while some still being CSL, are macroscopically incoherent and induce stress in the lattice, in some cases probably relaxing it with dislocations. Such cases of recombination active grain boundaries with dislocations in their close vicinity were found when the samples have been selectively etched for dislocation cluster analysis.[8] This macroscopic incoherence increases the number of available nucleation sites on the grain boundary during gettering, and a larger concentration of impurities is internally gettered on them. The precipitate distribution in their vicinity could potentially change during gettering so that more but smaller precipitates are present. This would result in a larger precipitate surface, more difficult to passivate during hydrogenation.

Previous studies showed that $\Sigma3$ grain boundaries tend to be decorated with metals closer to the detection limit than other types of grain boundaries, but in this study, $\Sigma3$ grain boundaries with high levels of recombination activity were found. To investigate the relation between the contamination level on such grain boundaries and their recombination activity, two $\Sigma3$ grain boundaries were selected from about 80% ingot height. One inactive and one active $\Sigma3$ grain boundary before and after gettering were chosen to analyse their metal precipitate distribution by μ-XRF. The IQE maps of these grain boundaries along with an EBSD map and the resulting μ-XRF maps can be seen in Fig. 6. Table II contains the detection limits for the presented μ-XRF maps.

TABLE II. Detection limits for each of the μ-XRF maps presented in Fig. 6. The values are given in ng/cm^2.

μ-XRF map	Fe	Ni	Cu
Inactive ungettered	9	4	5
Inactive gettered	9	4	5
Active ungettered	8	3	4
Active gettered	33	17	21

The grain boundary labeled as "Inactive" showed no IQE contrast after each processing step. The "Active" grain boundary started showing strong IQE contrast after gettering and remained recombination active after hydrogenation. The measurement results can be seen in Fig. 6. In the as-grown, ungettered material, large areas with high Fe, Ni, and Cu contents were found near the inactive grain boundary. After gettering, no particles are present at the same grain boundary above the detection limit of the technique. An opposite situation occurred on the recombination active $\Sigma3$ grain boundary. No precipitates above the detection limit were found before gettering, but after the gettering process, clusters of smaller metal precipitates are visible. Only a very limited number of four relatively small regions of interest could be analysed by μ-XRF in this study; however, the results indicate that contaminants are in the vicinity of this recombination-active grain boundary, suggesting a correlation.

Previous results showing that a change in Ni contamination levels on dislocation clusters was related to a change in their recombination strength[8] are in line with these results on grain boundaries. Strong signals from iron, nickel, and copper are found on the grain boundary that is activated during

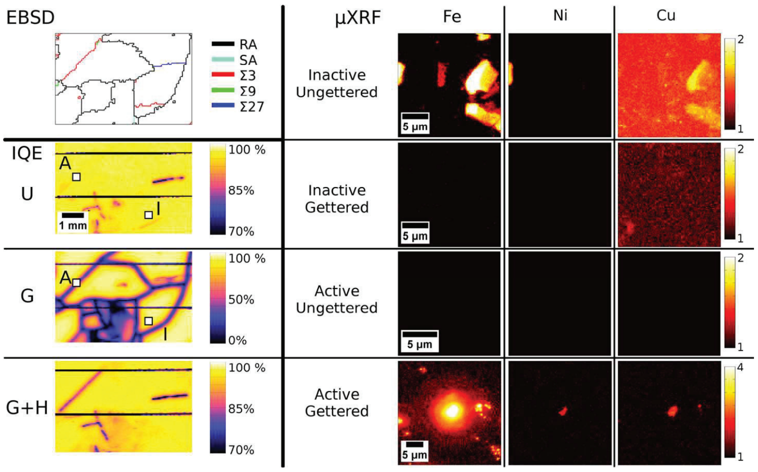

FIG. 6. EBSD and IQE of a sample area containing $\Sigma3$ grain boundaries, of which one is active and the other inactive in the gettered and hydrogenated state (G + H), along with μ-XRF maps of areas in close vicinity to these grain boundaries in two process states: ungettered (U) and after gettering (G). The IQE maps in the U and G state roughly show the positions of where the μ-XRF analysis was performed with white squares A for the active and I for the inactive $\Sigma3$ grain boundary. The μ-XRF maps are displayed in the logarithmic scale (base 10), where the color-bars represent the exponent and the unit is ng/cm^2.

gettering. This grain boundary remains active after hydrogenation. If the active Σ3 grain boundary is macroscopically incoherent and contains dislocations in its structure, it results in a different nucleation site density. On coherent Σ3 GBs, there are fewer nucleation sites, and during gettering, the dissolved impurities are extracted to the emitter. On the incoherent grain boundary, the increased nucleation site density leads to an internal gettering process, after which the recombination activity on the grain boundary increases.

C. Quasi-mono part of the ingot

The material analysed in this study comes from a hybrid ingot containing both HPMC and QM structures. The main focus is on the HPMC part, but the QM part was also analysed. The overall effect of grain boundaries on the IQE in the QM part was small due their nature and very low density. Small-angle grain boundaries were found in the QM part above the seed joint, and their misorientation was measured to be below 5°. They showed an activity very similar to SAGB in the HPMC part, presented in Sec. III B. Σ3 CSL grain boundaries could also be found in the QM part but they showed no detectable recombination activity.

IV. CONCLUSIONS

In this work, LBIC and EBSD measurements show that recombination activity of grain boundaries increases during gettering and is reduced in subsequent hydrogenation. About 90% of the random-angle grain boundaries are well passivated after standard cell processing. What remains recombination active are mostly small-angle grain boundaries, segments of random-angle grain boundaries, and special cases of CSL boundaries, on which a lack of coherence is suspected as a cause for increased nucleation site density.

The recombination activity in fully processed HPMC wafers is observed to be caused by dislocations in the form of clusters, SAGBs, and possibly as part of grain boundary structure reducing the macroscopic GB incoherence.

μ-XRF measurements of a typical inactive Σ3 grain boundary and a special case of this grain boundary type, activated during gettering, indicate that the change in recombination activity might be related to the presence of metals, as evidenced by a change in precipitate distribution on the extended defects.

ACKNOWLEDGMENTS

The work reported in this paper was performed in the project Impurity Control in High Performance Multicrystalline Silicon, 228930/E20, funded by the Norwegian Research Council's ENERGIX programme and industry partners REC Solar, REC Silicon, Steuler Solar, and The Quartz Corp. Part of this work was also supported by the SOPHIA project "HPSS," the Solar-Era. Net project "HighCast" via the Swedish Energy Agency, and the project "Advanced analysis of industrial silicon wafers for solar cells" by J. Gust. Richert stiftelse, which is gratefully acknowledged. The authors would like to thank Tonio Buonassisi for his comments on this work. M. A. Jensen and E. E. Looney acknowledge support by the National Science Foundation (NSF) Graduate Research Fellowship under Grant No. 1122374 and the NSF and the U.S. Department of Energy under NSF CA No. EEC-1041895. This research used resources of the Advanced Photon Source, a U.S. Department of Energy (DOE) Office of Science User Facility operated for the DOE Office of Science by Argonne National Laboratory under Contract No. DE-AC02-06CH11357.

[1] ITRPV and VDMA, 8 ed. (ITRPV, VDMA Photovoltaik Equipment, Frankfurt, Germany, 2017).
[2] Fraunhofer Institute for Solar Energy Systems, Photovoltaics Report No. 2017-07-12 (2017).
[3] M. Rinio, A. Yodyungyong, S. Keipert-Colberg, D. Borchert, and A. Montesdeoca-Santana, Phys. Status Solidi A **208**, 760 (2011).
[4] S. Castellanos, M. Kivambe, J. Hofstetter, M. Rinio, B. Lai, and T. Buonassisi, J. Appl. Phys. **115**, 183511 (2014).
[5] J. Chen, T. Sekiguchi, D. Yang, F. Yin, K. Kido, and S. Tsurekawa, J. Appl. Phys. **96**, 5490 (2004).
[6] M. Di Sabatino and G. Stokkan, Phys. Status Solidi A **210**, 641 (2013).
[7] T. Buonassisi, A. A. Istratov, M. D. Pickett, M. A. Marcus, T. F. Ciszek, and E. R. Weber, Appl. Phys. Lett. **89**, 042102 (2006).
[8] K. Adamczyk, R. Søndenå, C. C. You, G. Stokkan, J. Lindroos, M. Rinio, and M. Di Sabatino, Phys. Status Solidi A **215**, 1700493 (2018).
[9] C. W. Lan, A. Lan, C. F. Yang, H. P. Hsu, M. Yang, A. Yu, B. Hsu, W. C. Hsu, and A. Yang, J. Cryst. Growth **468**, 17 (2017).
[10] C. W. Lan, W. C. Lan, T. F. Lee, A. Yu, Y. M. Yang, W. C. Hsu, B. Hsu, and A. Yang, J. Cryst. Growth **360**, 68 (2012).
[11] K. E. Ekstrøm, G. Stokkan, A. Autruffe, R. Søndenå, H. Dalaker, L. Arnberg, and M. Di Sabatino, J. Cryst. Growth **441**, 95 (2016).
[12] L. Priester, *Grain Boundaries—From Theory to Engineering* (Springer, 2013), Vol. 172.
[13] N. Sakaguchi, M. Miyake, S. Watanabe, and H. Takahashi, Mater. Trans. **52**, 276 (2011).
[14] F. Komninou, T. Karakostas, G. Bleris, and N. Economou, J. Phys. Colloques **43**, 9 (1982).
[15] J. Chen and T. Sekiguchi, Jpn. J. Appl. Phys., Part 1 **46**, 6489 (2007).
[16] G. Stokkan, M. Di Sabatino, R. Søndenå, M. Juel, A. Autruffe, K. Adamczyk, H. V. Skarstad, K. E. Ekstrøm, M. S. Wiig, C. C. You, H. Haug, and M. M'Hamdi, Phys. Status Solidi A **214**, 1700319 (2017).
[17] M. Taguchi, A. Terakawa, E. Maruyama, and M. Tanaka, Prog. Photovolt.: Res. Appl. **13**, 481 (2005).
[18] M. Rinio, H. J. Möller, and M. Werner, Solid State Phenom. **63–64**, 115 (1998).
[19] G. Palumbo, K. T. Aust, E. M. Lehockey, U. Erb, and P. Lin, Scr. Mater. **38**, 1685 (1998).
[20] A. Autruffe, M. M'Hamdi, F. Schindler, F. D. Heinz, K. E. Ekstrøm, M. C. Schubert, M. Di Sabatino, and G. Stokkan, J. Appl. Phys. **122**, 135103 (2017).
[21] Z. Cai, B. Lai, W. Yun, I. McNulty, A. Khounsary, J. Maser, P. Ilinski, D. Legnini, E. Trakhtenberg, S. Xu, B. Tieman, G. Wiemerslage, and E. Gluskin, AIP Conf. Proc. **521**, 31 (2000).
[22] S. Riepe, I. E. Reis, W. Kwapil, M. A. Falkenberg, J. Schön, H. Behnken, J. Bauer, D. Kreßner-Kiel, W. Seifert, and W. Koch, Phys. Status Solidi C **8**, 733 (2011).
[23] D. Macdonald, A. Cuevas, A. Kinomura, Y. Nakano, and L. J. Geerligs, J. Appl. Phys. **97**, 033523 (2005).
[24] J. Lu, M. Wagener, G. Rozgonyi, J. Rand, and R. Jonczyk, J. Appl. Phys. **94**, 140 (2003).
[25] A. Autruffe, V. S. Hagen, L. Arnberg, and M. Di Sabatino, J. Cryst. Growth **411**, 12 (2015).
[26] P. Karzel, M. Ackermann, L. Gröner, C. Reimann, M. Zschorsch, S. Meyer, F. Kiessling, S. Riepe, and G. Hahn, J. Appl. Phys. **114**, 244902 (2013).

Article V:

Guidelines for establishing an etching procedure for dislocation density measurements on multicrystalline silicon samples

K. Adamczyk, G. Stokkan, M. Di Sabatino, 2018, MethodsX, vol. 5, p 1178–1186

Paper V

MethodsX 5 (2018) 1178–1186

Contents lists available at ScienceDirect

MethodsX

journal homepage: www.elsevier.com/locate/mex

Method Article

Guidelines for establishing an etching procedure for dislocation density measurements on multicrystalline silicon samples

Krzysztof Adamczyk[a,*], Gaute Stokkan[b], Marisa Di Sabatino[a]

[a] Department of Materials Science and Engineering, NTNU, NO-7491 Trondheim, Norway
[b] Sintef Materials and Chemistry, NO-7465 Trondheim, Norway

ABSTRACT

With multicrystalline silicon becoming the main material used for photovoltaic applications and dislocations being one of the main material limitations to better solar cell efficiency, etch pit density measurements are gaining more importance. Traditionally, etch pit density measurements are based on selective etching of silicon samples. The majority of the etchants have been developed for monocrystalline samples with known orientation, while those developed for multicrystalline samples have been less investigated and might need some optimization. In this study, we use and compare the PVScan tool, which provides a quick way to assess dislocation density on selectively etched samples, and microscope image analysis. We show how the etching methods used for dislocation density measurements can affect the results, and we suggest how to optimize the Sopori etching procedure for multicrystalline silicon samples with high dislocation densities. We also show how the Sopori etchant can be used to substitute Secco while maintaining a high precision of dislocation density measurements, but without the toxic hexavalent chromium compounds.

© 2018 The Authors. Published by Elsevier B.V. This is an open access article under the CC BY license (http://creativecommons.org/licenses/by/4.0/).

ARTICLE INFO

Method name: Sopori etching for etch pit density measurements, Combined with PVScan and microscope image analysis
Keywords: Selective etching, Sopori, Secco, Etch pit density, EPD, Dislocations, Silicon, Photovoltaic
Article history: Received 18 October 2017; Accepted 26 September 2018; Available online 28 September 2018

---

[*] Corresponding author.
E-mail address: krzysztof.adamczyk@ntnu.no (K. Adamczyk).

https://doi.org/10.1016/j.mex.2018.09.013

2215-0161/© 2018 The Authors. Published by Elsevier B.V. This is an open access article under the CC BY license (http://creativecommons.org/licenses/by/4.0/).

Specifications Table

Subject area	*Materials Science*
More specific subject area	*Analysis of methods for dislocation density measurements in silicon material for photovoltaic applications*
Method name	*Sopori etching for etch pit density measurements, combined with PVScan and microscope image analysis*
Name and reference of original method	*Sopori etching* [1] *PVScan* [2] *ImageJ* [3]
Resource availability	• *Glassware and bench suitable for handling reagents with HF* • *Grinding machine, grinding disc with grain size 500 and 1200* • *Polishing machine, diamond paste with grain size 9, 3, 1 μm* • *Sopori etchant–* HF:CH_3COOH:HNO_3 with a ratio of 36:15:2 • *Secco etchant–HF:*015 *mol $K_2Cr_2O_7$with a ratio 2:1* • *PVScan 6000 measurement system* • *Metallographic microscope* • *GIMP – GNU Image Manipulation Program* • *ImageJ – Image Processing and Analysis in Java* • *Matlab – used for PVScan data imaging* • *MS Excel – used for result analysis and plotting*

Background information

The Etch Pit Density (EPD) measured by the PVScan tool on an etched multicrystalline silicon wafer is typically in the range 10^4 and 3×10^6 cm^{-2}. No lower and higher values are measured.

For smaller dislocation density areas, the reason for no detection might be that with the low density of etching pits a change in the reflected laser signal is too small to be measured. For larger dislocation density areas, like in dislocation clusters, correct dislocation density cannot be measured because the etch pits overlap.

The main motivation behind this work was to address these issues by modifying the etching time to obtain different size of dislocation etch pits and allow a more precise measurement with the fast, large-area PVScan technique. It was hypothesized that to measure intra-grain dislocations, which are in the range below 10^4 cm^{-2}, a possible way could be to etch the sample longer and obtain bigger etch pits. For dislocation clusters, decreasing the etching time should lead to smaller etch pits and less etch pit overlap.

In this work the influence of etching time on etch pit size and etch pit density measurements was evaluated. The tests presented in this work were performed with the Sopori etchant recipe. Several studies important for the PV industry have also been performed with the Secco etchant recipe containing a carcinogenic hexavalent chromium compound, potassium dichromate, $K_2Cr_2O_7$ [4,5]. In addition to its toxicity, the Cr present in the Secco etchant can contaminate the sample and influence subsequent measurements of chemical composition analysis. Because of these factors, part of this work was also aimed at comparing the Secco and Sopori recipes for their use in etch pit density measurements to establish if the Sopori etchant could be used instead of Secco for precise measurements.

PVScan and microscope image analysis for EPD measurements

All the measurements were performed on one 5 × 5 cm slab coming from a high performance multicrystalline silicon (HPMC-Si) ingot, seeded with Si feedstock from the fluidized bed reactor (FBR) process and solidified at NTNU/SINTEF lab [6]. To prepare the sample for etching, its surface was ground on sandpaper and polished using a diamond suspension down to 1 μm.

The standard recipe used at NTNU for selective etching consists of the steps presented below and performed in one etching session (ratios, if not stated otherwise, are given in units of volume):

1 RCA1 cleaning/10 min
2 Dip in deionized water
3 5% hydrofluoric acid - HF/3 min
4 Sopori/25 s
5 HF:HNO_3(1:9)/5 s
6 Dip in deionized water
7 Flush with ethanol

The RCA1 cleaning mixture used in step 1 was developed in the Radio Corporation of America for cleaning of silicon wafers {Kern, 1990 #8} [7]. It consists of 5 parts of deionized water, 1 part of ammonia water (29% HNO_3) and 1 part of aqueous H2O2 (30% H_2O_2). It is applied by dipping the silicon wafer in the mixture at a temperature of 80 °C with agitation. The remaining etchants and mixtures are applied by dipping the silicon wafer in the etchants at room temperature and without agitation, only with a very slow mixing introduced by moving the sample holder in the bath. The dipping time is given for each step. Dips in deionized water don't require time control.

The Sopori etchant used in step 4 is a mixture of HF:CH_3COOH:HNO_3 with a ratio of 36:15:2. Silicon etching with such an etchant is a multi-reaction process in which a local concentration of reaction products could lead to increased etching locally. The etchant mixing by moving the sample holder in the bath is introduced to avoid such changes in the etching rate and allow for a more even distribution of substrates and products.

Evaluation of different etching time was performed by changing the time used for Sopori step in the standard NTNU recipe and leaving the remaining steps unchanged. In the first three etching sessions the sample was etched afterwards without repolishing, with Sopori etching steps lasting 5, 10 and 10 s – up to 25 s in total, as in the standard procedure. This was done to evaluate if it is possible to first obtain a measurement on a surface with small etch pits and subsequently etch the same sample further, to obtain measurements comparable with the standard procedure.

For the next sessions, the sample was repolished before each etching. Sessions with the Sopori step lasting 25, 75 and 150 s were performed to obtain standard and larger etch pits. Finally, the sample was repolished and etched for 5 s with the Sopori mixture diluted down to HF:CH_3COOH:HNO_3 ratio of 36:20:1 to obtain etch pits smaller than in the first three sessions.

The Secco etching procedure used in this work was as follows:

1 Dip in acetone
2 Dip in ethanol
3 Dip in deionized water
4 Secco/60 s

The Secco etchant is a mixture of one part of 0.15 M solution of $K_2Cr_2O_7$ in H_2O and two parts of 49% HF.

Etch pit density measurements with PVScan and microscope analysis was performed after each etching session.

PVScan 6000 is a surface scanning tool which allows for relatively fast evaluation of etch pit density by integrating the diffused light reflected by the etched surface. The basic principle of operation of this instrument is presented in Fig. 1. A laser beam is used to illuminate the surface. Surface free of any defects like dislocation clusters or grain boundaries will reflect the light directly and the signal coming from the diffused light detector is weak. When the laser illuminates defects, the signal is varied depending on the density of the defects. As mentioned earlier, this technique fails when the etch pits are not dense enough, or when their density is too high and leads to overlapping. Microscope image analysis allows to measure etch pit density more precisely, but requires more time and usually allows analysis of much smaller areas.

Calculating the etch pit density by microscope image analysis can be explained with Fig. 2 showing the subsequent steps in the process. All the presented steps were performed in ImageJ software. The image was first converted from the color image format into a black and white image. This allowed for thresholding, which is a division of the pixels on image into two groups depending on their intensity

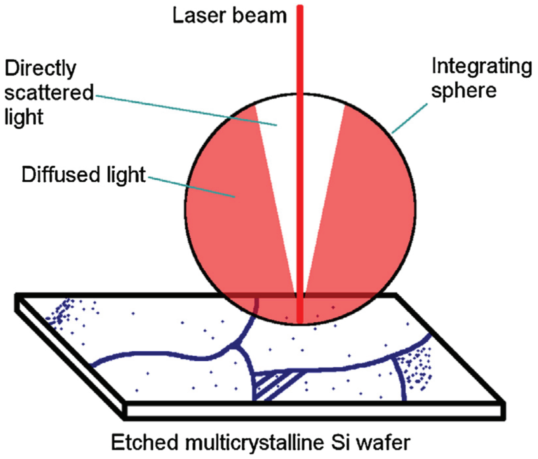

Fig. 1. Schematic presenting the basic principle of PVScan operation [2].

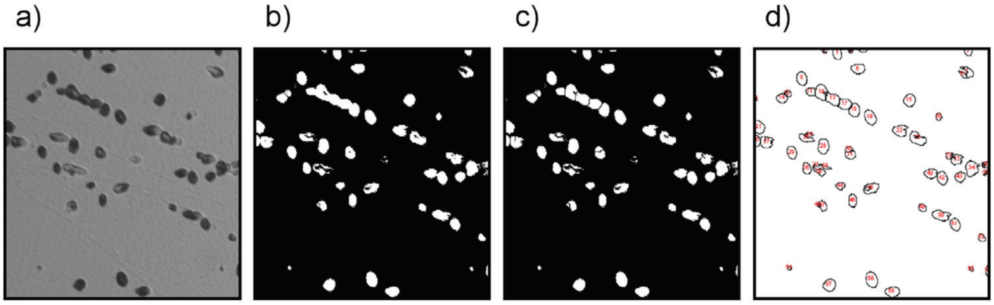

Fig. 2. Etch pit density measurement by microscope image analysis with ImageJ software. The image shown here was slightly trimmed down from 100 × 100 μm for presentation. Its analysis resulted in a count of 58 etch pits, leading to a density of 5.8×10^5 dislocations/cm^2. Each frame shows an effect of a processing step.
a) Microscope image is converted to 8-bit black and white image.
b) Image is thresholded into 2 values – white for etch pit, black for background c) Watershed operation performed in order to divide overlapping etch pits d) Etch pits fulfilling the analysis conditions are counted by Particle Analysis tool.

values, higher and lower than the threshold, and assigning them to only two values, black and white. To compensate for etch pit overlap, the ‘watershed’ operation was performed on the image. This operation searches for cases of overlapping particles on the image, basing on their shape, and divides them accordingly. While it may lead to dividing single etch pits into several areas on the image if their shape is far from circular, the majority of the overlapping etch pits are separated. The etch pits fulfilling the analysis conditions are then counted by the software.

To compare both methods different areas were selected on the samples, one with large dislocation densities for analysis of shorter Sopori etching times, one with smaller dislocation densities for longer etching times. The selection was made on PVScan dislocation density maps which, while less precise, are easier and faster to obtain.

The dislocation density maps from PVScan are discrete, that is each value was obtained by stepping over the scanned area with a discrete step size. In the case of reported measurements this step size equaled 100 μm. Because of this the microscope images, covering a limited area, were first manually stitched in GIMP software into larger images covering areas which could be more easily compared with PVScan maps, and then divided into areas corresponding to PVScan pixels. This can be more easily understood when looking at Fig. 3. The resulting ‘pixel’ microscope images were automatically

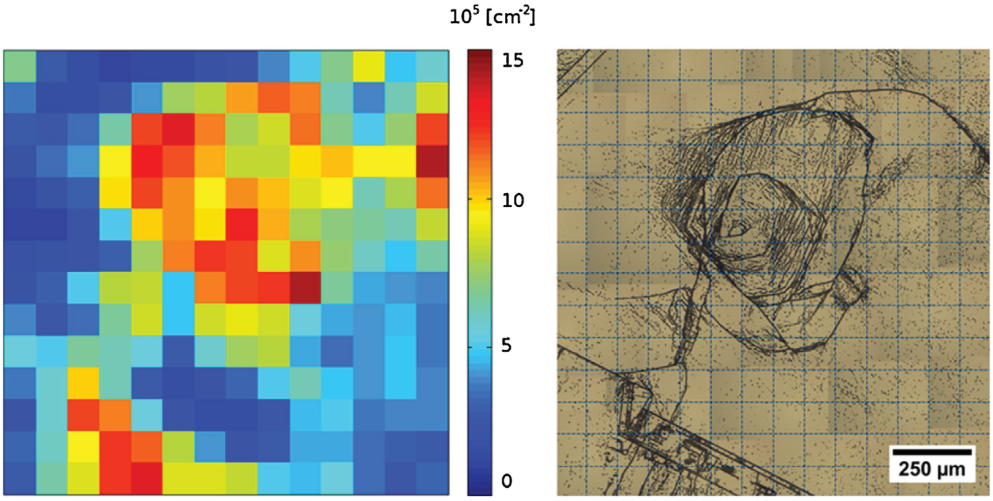

Fig. 3. Images of same area of the silicon sample, obtained with different techniques: on the left is a PVScan etch pit density map and on the right is a microscope image, stitched and divided into areas corresponding to PVScan pixels. The orientation axis system on the PVScan map refers to pixel positions. Each such pixel corresponds to 100 × 100 µm square on the microscope image.

processed with ImageJ software, as described above. The etch pit density results were compared between each PVScan pixel and a corresponding 'pixel' from ImageJ microscope image analysis.

For the low dislocation density areas, the lowest density measured – that is if 1 etch pit was visible on 100 × 100 µm square – was equal to 10^4 dislocations/cm^2. Since lower values were expected in low dislocation density areas, they were divided into a grid of 200 x 200 µm instead of 100 × 100 µm. Such larger 'pixels' were compared with PVScan maps, which were recalculated to the same pixel size – one new pixel with a density value calculated as an average of four original PVScan pixels. Such binning allowed comparison with microscope image analysis of areas with etch pit densities down to 2.5×10^3 dislocations/cm^2. It needs to be noted that the PVScan laser beam has a diameter of about 800 µm, but reanalysing the microscope data so that each pixel result was a weighted average of itself and its surrounding pixels with weights accounting for the PVScan beam intensity did not lead to different conclusions than the ones without such recalculation, meaning that the intensity of the laser beam is not uniform and majority of PVScan signal comes from scattering mostly its high-intensity center part. For simplicity the microscope analysis results presented below are based on single pixels, without the weighted average recalculation.

Etch pit size was measured with ImageJ software on the microscope images obtained after etching.

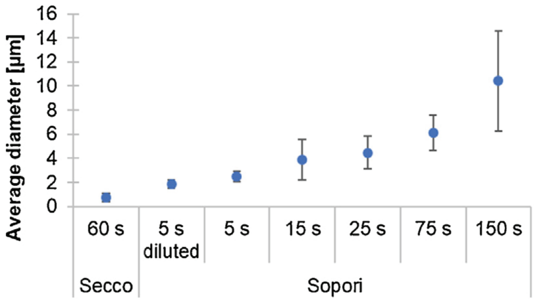

Fig. 4. Etch pit size for each of the etching procedures tested in the experiment. 150 random etch pit diameters averaged for each etching time.

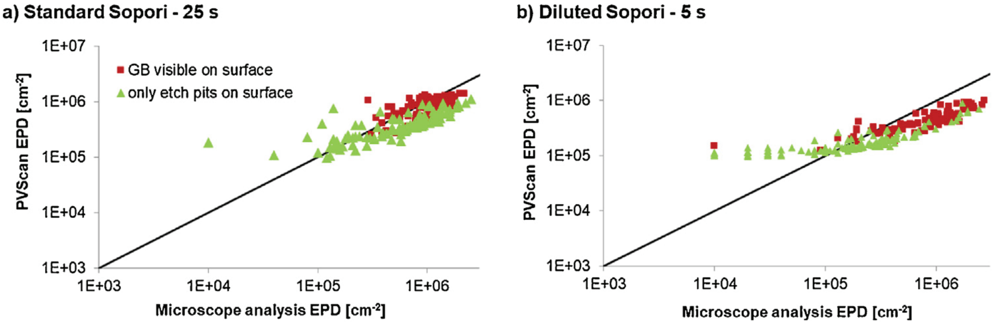

Fig. 5. Charts presenting the comparison between dislocation density values measured by PVScan and by microscope image analysis. The different etching times were tested on the same area, repolished after each etching session.
a) Standard NTNU Sopori etchant, used for 25 s as in standard procedure.
b) Diluted Sopori etchant used only for 5 s, to obtain lower size of etch pits for analysis of high dislocation density areas.

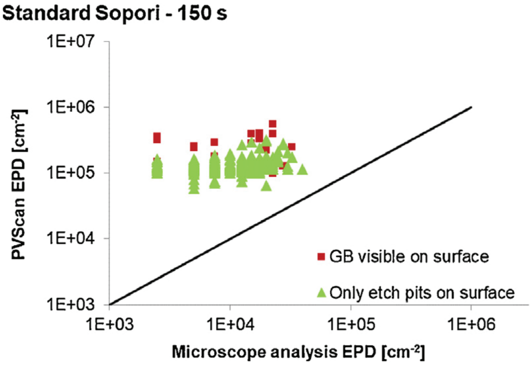

Fig. 6. Comparison between dislocation density values measured by PVScan and by microscope image analysis on a sample etched with the standard Sopori etchant used for 150 s to obtain larger size of etch pits for analysis of low dislocation density areas.

Etch pit size comparison is presented in Fig. 4. As expected for Sopori, the average etch pit diameter was largest for the longest etching time, and smallest for shortest time of etching in a dilute etchant. The etch pit size obtained according to the Secco etching procedure was smaller than the size obtained from a short etch in diluted Sopori.

The results showing a comparison between PVScan measurements and microscope image analysis with ImageJ are presented in Figs. 5 and 6. The data for analysis of high dislocation density presented in Fig. 5 for both charts comes from the same area as presented in Fig. 4, while data for low dislocation density areas was obtained from a different sample area, free of larger dislocation clusters.

The black line dividing the chart area is a linear representation of the case where the results from PVScan are equal to the results from microscope image analysis. If the point is above this line, PVScan measured a value higher than obtained by microscope analysis on the same area. If the point is below the line, the PVScan value was lower. A distinction is made within the data between pixels covering an area with grain boundaries visible in addition to etch pits and pixels covering areas with etch pits, but without grain boundaries.

A general conclusion from the above comparison is that if a grain boundary is present in the scanned area, PVScan returns a higher dislocation density value than can be obtained with microscope analysis. The etched grain boundary also scatters the laser beam and more signal is measured by PVScan.

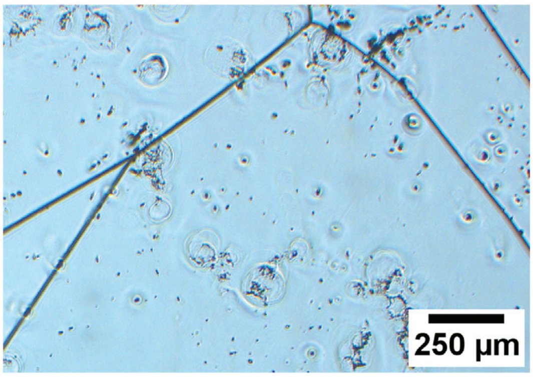

Fig. 7. Image of sample surface after 150 s etching in standard Sopori etchant.

Another feature similar for all the datasets is that the PVScan showed a very low signal to noise ratio for dislocation densities below 10^5 dislocations/cm^2. This is a cutoff value for the data points on charts a) and b). Even for pixels where etch pits were visible with microscope in densities closer to 10^4 cm^{-2}, PVScan assigned values above 10^5 cm^{-2}. It was expected to have low signal to noise ratio coming from areas with low density of small etch pits, which is visible on the chart b) in Fig. 5, but increasing the etch pit size by longer etching did not result in better sensitivity of the PVScan system. The chart in Fig. 6 shows that there seems to be no correlation between dislocation density measured by PVScan and with microscope image analysis in the low density range. This might be related to the etching conditions, where the long etching time not only led to an increase in etch pit size, but also resulted in introducing significant artifacts on the sample surface. Some of these artifacts are visible in Fig. 7. As was seen in Fig. 4, the etch pits after 150 s of Sopori etching are not uniform, their size differs across a wide range of values. The reason for such artifacts can be that for such long etching times the mixing introduced by moving the sample in the bath is not efficient enough. Different techniques should be used to increase the mixing. The artifacts can affect the results from both techniques, with PVScan being probably more prone to error because of it. Each of these artifacts scatters light of the PVScan laser beam, resulting in increased signal for this technique. Majority of the artifacts is not counted as etch pits by the microscope image analysis algorithms due to their capability to distinguish defects by their size. Etching the sample with three subsequent steps without repolishing, with 5, 10 and 10 s steps, also led to having similar artifacts on the surface.

In the range of high dislocation densities, the data coming from a sample etched in a diluted etchant gave a smaller spread of values coming from PVScan. The PVScan settings are a linear calibration of the measured signal: $\rho = C^*S$, where the dislocation density ρ is calculated from the signal S based on a calibration constant C [8]. The calibration constant can be adjusted for the diluted etchant showing a possibility of closer fit between PVScan and microscope image analysis in the range above 10^5 cm^{-2}. Modifying the calibration equation to contain a constant factor accounting for the noise in low dislocation density areas can be also considered. This would increase the precision of this fast measurement technique and make it more comparable with the more tedious, but also more precise microscope analysis.

The comparison between measurements of high dislocation density areas showed an additional issue with precise measurement. As can be seen in Fig. 5, in the range below 10^5 cm^{-2} there is a difference in what was found by microscope image analysis after 25 s in the standard etchant and after 5 s in a diluted etchant. As analysis of the etched surfaces reveals, the standard etch results in a variety of etch pits, ranging from circular to elliptic, and the elliptic etch pits seem more shallow. The difference in etch pit shape can be explained by differing angles between the surface and the dislocation core. The etch pits on the sample after the shorter, diluted etch are much more uniform, as if only the dislocations at a certain preferential angle to the surface were etched. The small etch pit size with fewer overlapping etch pits allowed for a more precise quantification of high dislocation density areas, but the fact that part of the dislocations aligned in less preferential orientations didn't etch

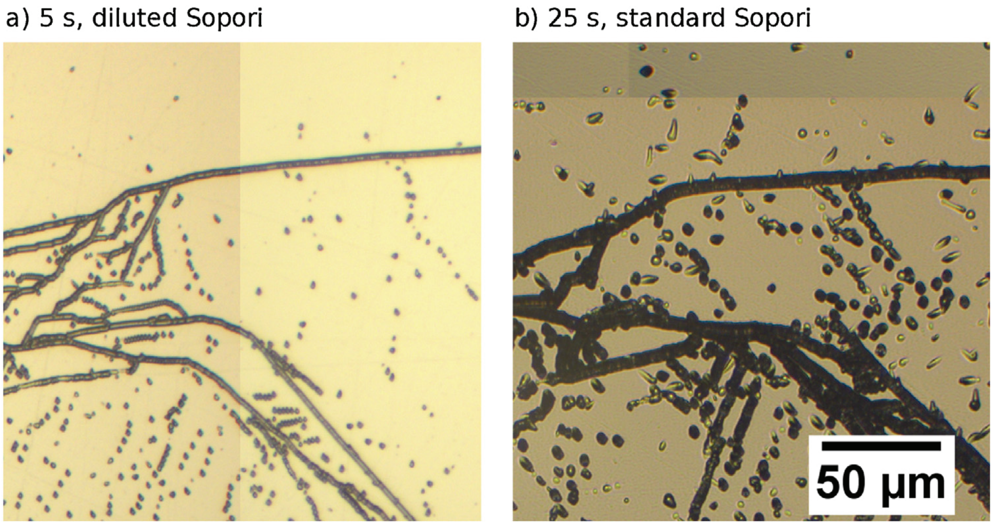

Fig. 8. Microscope images of the same sample area, a) etched for 5 s in a diluted Sopori etchant and b) for 25 s in standard Sopori etchant. The sample was repolished between each etching session.

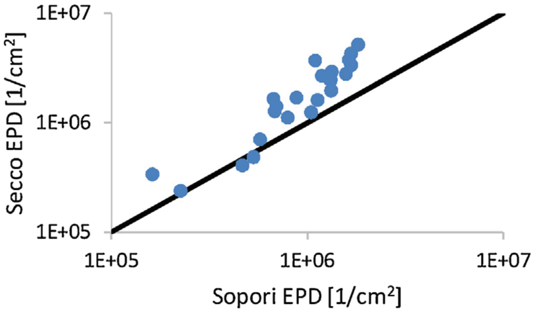

Fig. 9. Effect of etching procedure on EPD measurements by microscope image analysis. 60 s Secco and 5 s standard Sopori are compared.

needs to be considered when applying this technique. A comparison of the surface after the two discussed etching steps is shown in Fig. 8.

As the above results show, dividing the etching procedure into short etching for high dislocation density analysis and subsequent long etching for low dislocation density analysis does not yield good results, especially in the low density range after long etching. Combining long etching with short etching without repolishing samples between such sessions may introduce etching artifacts and make further measurements unprecise. Shorter etching times can be applicable if only high dislocation density areas need to be characterized with more precision. Proper optimization of the etching time can allow precise analysis on the PVScan instrument.

Comparison between Sopori and Secco etching

For a comparison between the Secco etchant and Sopori etchant, the etch pit density was measured in the same areas after etching for 5 s in standard Sopori and then after repolishing and etching in Secco for 60 s. In the original paper on Secco it was suggested to etch monocrystalline silicon samples for 5 min with ultrasonic agitation. 60 s without agitation is enough to selectively etch multicrystalline silicon samples, thus 60 s was used for this comparison. The results of the microscope image analysis of the surface obtained after each of these procedures are shown in 9. Microscope image analysis was chosen as the technique for this comparison, because due to the etch pit size the PVScan signal was very weak, resulting in lower dislocation densities. Fig. 9 indicates that even 5 s is too much for the Sopori etchant to obtain precise dislocation density measurements in the high density range. The 60 s Secco etch gives an etch pit size of about 0.5–1 μm, while the 5 s Sopori etch results in 2 μm etch pits. The main cause for the difference in measurement between the two etching procedures is the overlap of etch pits in the range above $10^5\,\mathrm{cm}^{-2}$ for Sopori.

The conclusion from this comparison is that the Secco etchant can be replaced with Sopori etching, but the Sopori etching procedure needs to be further optimized for measurements of high dislocation density areas. Etching times with the diluted Sopori etchant below 5 s are suggested in such case. Replacing the Secco etchant with Sopori gives significant benefits since one can avoid toxic and carcinogenic Cr compounds.

Acknowledgements

The authors would like to thank Torild Krogstad for her help with the etching performed in this study. The work reported in this paper was performed in the project Impurity Control in High Performance Multicrystalline Silicon, 228930/E20, funded by the Norwegian Research Council's ENERGIX programme and industry partners REC Solar, REC Silicon, Steuler Solar, and The Quartz Corp.

References

[1] B. Sopori, A new defect etch for polycrystalline silicon, J. Electrochem. Soc. 131 (1984) 667–672.
[2] B. Sopori, W. Chen, Y. Zhang, T. Hemschoot, J. Madjdpour, Extending PVSCAN to meet the market needs for high-speed, large-area scanning, 9th Workshop on Crystalline Silicon Solar Cell Materials and Processes (1999).
[3] C.A. Schneider, W.S. Rasband, K.W. Eliceiri, NIH Image to ImageJ: 25 years of image analysis, Nat. Methods 9 (7) (2012) 671–675.
[4] M. Rinio, A. Yodyungyong, S. Keipert-Colberg, D. Borchert, A. Montesdeoca-Santana, Recombination in ingot cast silicon solar cells, Phys. Status Solidi A 208 (4) (2011) 760–768.
[5] S. Castellanos, M. Kivambe, J. Hofstetter, M. Rinio, B. Lai, T. Buonassisi, Variation of dislocation etch-pit geometry: an indicator of bulk microstructure and recombination activity in multicrystalline silicon, J. Appl. Phys. 115 (18) (2014).
[6] G. Stokkan, M. Di Sabatino, R. Søndenå, M. Juel, A. Autruffe, K. Adamczyk, H.V. Skarstad, K.E. Ekstrøm, M.S. Wiig, C.C. You, H. Haug, M. M'Hamdi, Impurity control in high performance multicrystalline silicon, Phys. Status Solidi A 214 (7) (2017) 1700319.
[7] W. Kern, The evolution of silicon wafer cleaning technology, J. Electrochem. Soc. 137 (6) (1990) 1887–1892.
[8] G. Stokkan, Characterisation of dislocation density of multicrystalline silicon wafers using the PVScan 6000, 22nd European Photovoltaic Solar Energy Conference (2007).